NATIONAL INSTITUTE FOR FUSION SCIENCE

Resent Developments of Pulsed Power Technology and Plasma Application Research

Edited by Jun Hasegawa and Tetsuo Ozaki

(Received - Dec. 22, 2017)

NIFS-PROC-110

Jan. 12, 2018

Resent Developments of Pulsed Power Technology and Plasma Application Research

Edited by Jun Hasegawa and Tetsuo Ozaki

January 5-6, 2017
National Institute for Fusion Science
Toki, Gifu, Japan

ABSTRACT

The papers presented at the symposium on “Resent Decelopments of Pulsed Power Technology and Plasma Application Research” held on January 5-6, 2017 at National Institute of Fusion Science are collected. The papers in this proceeding reflect the current status and progress in the experimental and theoretical researches on high power particle beams, high energy density plasmas produced by pulsed power technology.

Keywords

high power particle beams, high energy density plasma, pulsed power technology, z-pinch, soft x-ray, EUV, neutron source, pulsed discharge, high power micro wave, material processing, biological application

Preface

The symposium entitled “Recent Developments of Pulsed Power Technology and Plasma Application Research” was organized as a part of the General Collaborative Research of National Institute for Fusion Science (NIFS) and held on January 5-6, 2017 at NIFS, Toki.

In the symposium, 23 papers were presented in two days, of which 20 papers are reported in this proceeding. The total number of participants was 45 including students and researchers from universities and companies.

The main objective of the symposium is to provide a place of discussion about the pulsed power technology, generation of plasmas by using pulsed power technology and its application. Therefore, the papers in this proceeding reflect the current status and progress in the experimental and theoretical researches on high power particle beams and high energy density plasmas produced by pulsed power technology in Japan. It is our great pleasure with the unexpectedness if the symposium was beneficial to the development of pulsed power and fusion technologies.

We would like to express our sincere thanks to all of the participants, the authors and the staff of NIFS.

Jun Hasegawa
Tokyo Institute of Technology

Tetsuo Ozaki
National Institute for Fusion Science

Contents

List of Participants

Akira Tokuchi	(Pulsed Power Japan laboratory)
Tohru Kawamura	(Tokyo Institute of Technology)
Sunao Katshuki	(Kumamoto University)
Soowon Lim	(Kumamoto University)
Weihua Jiang	(Nagaoka University of Technology)
Taichi Sugai	(Nagaoka University of Technology)
Tomoya Ito	(Nagaoka University of Technology)
Tatsuro Ohka	(Nagaoka University of Technology)
Yasunori Eguchi	(Nagaoka University of Technology)
Hirofumi Sasaki	(Nagaoka University of Technology)
Luu Trung Dung	(Nagaoka University of Technology)
Daijiro Fujisawa	(Nagaoka University of Technology)
Keiichi Takasugi	(Nihon University)
Noboru Yugami	(Utsunomiya University)
Kazuhiko Horioka	(Tokyo Institute of Technology)
Tomonobu Itagaki	(Tokyo Institute of Technology)
Shotaro Kittaka	(Tokyo Institute of Technology)
Seiichiro Yoshioka	(Tokyo Institute of Technology)
Hiroaki Ito	(Toyama Univsersity)
Hayato Ohashi	(Toyama Univsersity)
Tukasa Nakamura	(Toyama Univsersity)
Tarou Honoki	(Toyama Univsersity)
Yoshio Imai	(Toyama Univsersity)
Motohiro Teramae	(Toyama Univsersity)
Fumiya Niwa	(Toyama Univsersity)
Takashi Kikuchi	(Nagaoka University of Technology)
Tohru Sasaki	(Nagaoka University of Technology)
Ryota Hayashi	(Nagaoka University of Technology)
Taichi Takezaki	(Nagaoka University of Technology)
Jun Hasegawa	(Tokyo Institute of Technology)
Kohei Okutomo	(Tokyo Institute of Technology)
Keiichi Kamada	(Kanazawa University)
Yukihiro Soga	(Kanazawa University)
Youngsoo Park	(Kanazawa University)
Dai Takaki	(Kanazawa University)
Shogo Nakata	(Kanazawa University)
Thang Nhat Tan	(Kanazawa University)
Takumi Yoshino	(Kanazawa University)
Tatsuya Ohtake	(Kanazawa University)

Kazuto Tanimura (Kanazawa University)
Teruhiko Tajima (National Institute for Fusion Science)
Tetsuo Ozaki (National Institute for Fusion Science)
Eiki Hotta (Tokyo Institute of Technology)
Katsufumi Nakanishi (Shindengen)

Development and evaluation of chopper type Marx Modulator for International Linear Collider

Hirofumi Sasaki[#, A)], Weihua Jiang[A)], Taichi Sugai[A)], Akira Tokuchi[B)], You Sawamura[B)], Mitsuo Akemoto[C)], Hiromitsu Nakajima[C)], Masato Kawamura[C)]

[A)] *Nagaoka University of Technology*
[B)] *Pulsed Power Japan Laboratory Ltd.*
[C)] *High Energy Accelerator Research Organization (KEK)*

ABSTRACT

On the International Linear Collider (ILC), 10 MW multi-beam klystron will be used as the driver for microwave source. For multi-beam klystron power supplies, long pulse power supplies with specifications of -120 kV (± 0.5%), 140 A, 1.65 ms, 5 pps are required. Therefore, the chopper-type MARX modulator that combines a MARX circuit with a step-down chopper circuit has been proposed. In this paper, we report the evaluation results of the chopper type MARX modulator.

Keywords

ILC, MARX modulator, Pulse Power

1 Introduction

In the International Linear Collider, a multi-beam klystron of 10 MW will be used as a microwave source. As shown in Table 1 for the power supply of the multi-beam klystron, a long pulse power supply is required with high precision as compared with a general high voltage pulse power supply. In addition, high reliability of power supply, high efficiency, small size, low cost are required. When trying to realize this specification with a normal MARX power supply or a pulse transformer, it is inevitable to increase the size of the power supply. Therefore, a chopper type MARX Modulator that combines a MARX circuit with a step-down chopper circuit has been proposed. -2 kV charging, -1.6 kV output cells superimposed in 4 stages is taken as 1 unit.

Its output is -6.4 kV. Furthermore, by using 20 units, we achieve an output of -120 kV. We report the evaluation results of the prototype chopper type Marx Modulator.

Table 1: Specification of Pulsed Power Supply[1]

Output Voltage	-120 kV
Output Pulse Flat-top	< ±0.5 %
Output Current	140 A
Pulse Width (flat-top)	1.65 ms
Pulse Repetition Frequency	5 Hz
Rise time and Fall time	< 0.1 ms
Energy deposited into klystron during a gun spark	< 20 J

2 Chopper type MARX Modulator

2.1 Main circuit

Figure 1 shows the circuit of one unit of the chopper type MARX power supply. The capacitor CM of each MARX cell is charged in parallel by turning on SWC. At the time of discharging, discharging is performed by PWM controlling SWD. For this reason, it is possible to compensate the CM voltage decreasing during discharging by the change in the duty ratio. Moreover, by superimposing the voltage by shifting the phase of each stage of MARX, the ripple generated in the step-down chopper can be reduced.

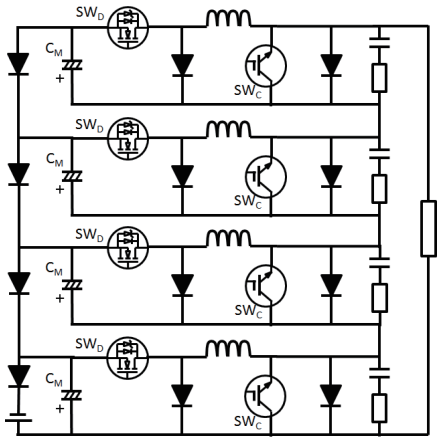

Figure 1: Simplified circuit schematic of chopper-type Marx modulator.

Figure 2 shows a picture of the actual chopper type MARX power supply. It is a system with a total of 20 units.

Figure 2: Photograph of the Chopper-type Marx modulator.

2.2 Charging system

The charging of the chopper type MARX power supply is performed by one high frequency transformer for each unit. At present, as shown in Figure 3, high-frequency transformers for 4 units are driven by one inverter to charge. However, since one high-frequency transformer is designed to be driven by one inverter, it is planned to finally add an inverter.

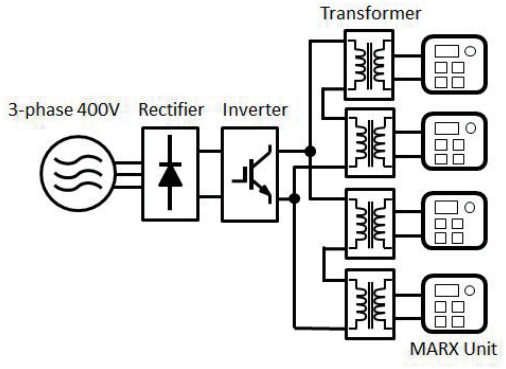

Figure 3: Charging system diagram.

3 Power supply evaluation test

3.1 Phase control between each unit

Regarding the phase control, by shifting the phase of each stage by 1/80 of the PWM period, the ripple rate of the output voltage becomes the minimum under the ideal condition. Therefore, for phase control of each stage of MARX, control is set which shifts by 5 μs which is ¼ of the PWM period (20 μs) in 4 cells in the unit. Also, the phase between each unit is shifted by 0.25 μs, which is 1/80 of the PWM cycle, and setting is made so that all 80 cells are out of phase by 1/80. This is shown in Figure 4 (a), where the arrow shows that the phase is shifted by 0.25 μs. However, in the current charging system, the influence of the coupling due to the capacitance between the windings of the high-frequency transformer is large. Therefore, phase control between each unit was adjusted. Four units that use the same inverter with strong coupling of stray capacitance are regarded as one group. Within this group, PWM control is performed with the same phase. Although the four cells in the unit are shifted by 5 μs similarly to the ideal condition, the phase between each group is controlled to shift by 1/20 (1 μs) of the PWM cycle. This is shown in Figure 4 (b). The arrows indicate that the phase is shifted by 1 μs.

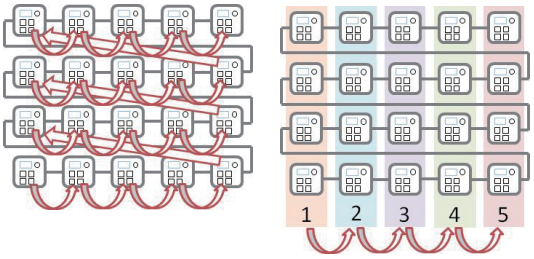

(a) 1/80 shift. (b) 1/20 shift.

Figure 4: Diagram of phase shift.

Figure 5 and Figure 6 show the results of the output voltage under two conditions with different phase control. The conditions were a charging voltage of 72 V, a duty ratio of 80 % to 97 %, and a load of a dummy resistance of 800 Ω. The output voltage when shifting the phase by 1/80 is shown in Figure 5, and the ripple ratio is ± 2.9 %. On the other hand, the output voltage when the four units charging using the same inverter are moved with the same phase is shown in Figure 6. The ripple ratio is ± 0.7 %, and it can be confirmed that the ripple ratio improves more than the phase control that minimizes the ripple under ideal conditions.

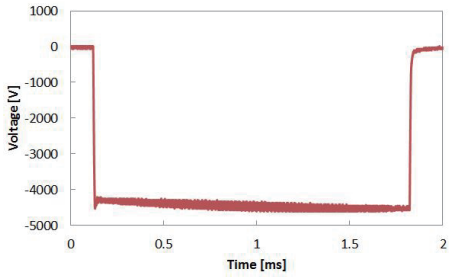

Figure 5: Output voltage at 1/80 shift.

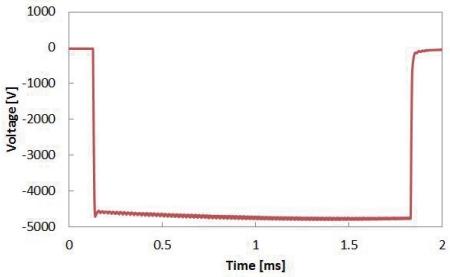

Figure 6: Output voltage at 1/20 shift.

3.2 Klystron test

As described in Section 3.1, with adjustment of the phase control between the units, RC snubbers of 40 Ω and 375 nF were connected to the output of the unit, and the klystron load test was conducted. Thales' 5 MW TH 2104 was used for the klystron. Figure 7 shows the output waveform when the charging voltage is -1.2 kV and the duty ratio is 86 % to 97 %. Output voltage - 82.0 kV, ripple ratio ± 0.2 %, output current - 46.5 A was confirmed. However, under the present situation, an undershoot occurs at the falling edge of the waveform, and an overvoltage is applied to the klystron. Therefore, the introduction of soft start is necessary.

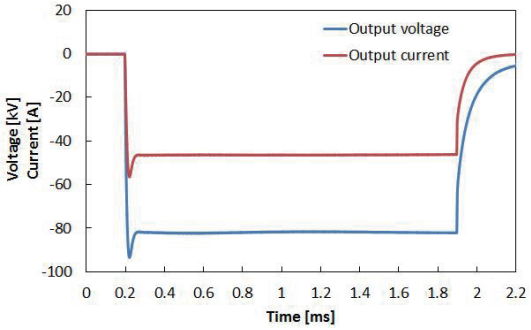

Figure 7: Measured modulator output waveform.

4 Conclusion

A chopper type MARX Modulator was tested as a power source for 10 MW multi-beam klystron which will be used in ILC. Adjustment of the phase shift between each unit was performed, and the output characteristics when klystron was used as a load in 20 units were confirmed. By introducing soft start in the future, we plan to aim for operation with output voltage of -120 kV, output current of 140 A, and repetition frequency of 5 Hz.

Reference

[1] ILC Technical Design Report Volume 3–Accelerator,2013, http://www.linearcollider.org/ILC/Publications/Technical-Design-Report.

Development of warm dense matter generation and specific heat measurement system in implosion time scale for fuel pellet design of inertial confinement fusion

Ryota Hayashi*, Tomoaki Ito*, Tomoki Ishitani*, Kazumasa Takahashi*, Toru Sasaki*, Takashi Kikuchi*, Nob. Harada*, Weihua Jiang*, Kenji Kashine**, Akira Tokuchi*,***

*Nagaoka University of Technology
**National Institute of Technology, Kagoshima College
***Pulsed Power Japan Laboratory Ltd.

ABSTRACT

A warm dense matter generator by pulsed power discharge with isochoric heating during an implosion time scale of inertial confinement fusion is developed. An intense pulsed power generator is used to input the energy into the sample during the implosion time period. An optical measurement system is arranged with the simultaneous operation by triggering the pulsed power discharge. As a result, several 1000 K of the sample is observed, and warm dense matter is generated with well–defined condition. The specific heat measurement system is developed by the results of the temperature and the input energy histories in the WDM state.

Keywords

Inertial Confinement Fusion, Pulsed Power, Warm Dense Matter, Specific Heat

1 Introduction

Properties of warm dense matter (WDM) are important, because the physical properties affect an implosion process of an inertial confinement fusion (ICF) system [1]. A pulsed power discharge with isochoric heating was proposed to investigate the WDM characteristics [2, 3]. In the setup, the density of a sample (i.e., WDM) is well-defined because the volume of the sample is given by a rigid capillary wall, and the temperature of the sample is controlled by the input energy due to the discharge current. As a result, the various WDM conditions in the density and the temperature are achieved by using a foamed metal as the sample with the system. The WDM research at the time scale of the implosion process in ICF was proposed with an intense pulsed power device by using the pulsed power discharge with the isochoric heating [4–6]. To explore the physical properties such as electrical and thermal conductivities, thermodynamic properties, equation–of–state, a well–defined WDM is expected for the measurements.

To generate the WDM in a laboratory scale, the pulsed power discharge with isochoric heating was proposed and carried out during several μsec of the time scale. In this study, the pulsed power discharge with isochoric heating by using the intense pulsed power generator "ETIGO-II" [7] (Extreme Energy–Density Research Institute, Nagaoka University of Technology) is investigated to create the WDM during the ICF implosion process (several–tens nsec). The electron beam diode as the impedance controller [4, 6, 8] is installed for the input energy control into the sample.

2 Experimental Method

The intense pulsed power generator "ETIGO-II" [7], which is used as the pulsed power supply in this study. The nominal parameters of ETIGO-II are suitable for this research because of the peak output voltage of 1 MV, the output current of 590 kA, and the pulse duration of 100 nsec, respectively. The outline of the experimental setup consists of the sample, an electron beam diode placed on the output terminal of ETIGO-II, voltage and current measurement devices, and an optical measurement system. The sample, the electron beam diode, and the voltage and current measurement devices are installed into the vacuum chamber. The pressure in the vacuum chamber is set as less than 0.02 Pa in the discharge experiment.

The sample is surrounded with a glass capillary as a rigid wall [6]. The sample material is a copper wire (ø20 μm) and/or a foamed metal, and the density is set as 0.1 ρ_s (ρ_s is the solid density of Cu, 8.96×10^3 kg/m^3).

As the optical measurement system, the streak camera (Hamamatsu Photonics: C7700-1) mounted with the spectroscope (Hamamatsu Photonics: C1119-01) is trigged by the voltage signal from ETIGO-II. The light emission from the sample placed in the vacuum chamber is transported from the sample to the streak camera in the atmosphere. Only the optical path consists of the mirrors placed in the atmosphere, and the length is determined by the time delay of the trigger signal and the streak camera.

3 Experimental Result

The current I of the sample and the voltages for V_1 and V_2 at both edge of the sample were directly measured by the Rogowski coil and the resistive dividers [6].

$$V(t) = V_1(t) - V_2(t) - L\frac{dI(t)}{dt}, \qquad (1)$$

The applied voltage V at the sample was adjusted by Eq. (1) with the stray inductance of $L = 75$ nH. The stray inductance was measured pre-experimentally with the short circuit. The input power into the sample was obtained by the product of the current and the voltage, and the input energy into the sample was given by the integration of the input power.

The spectrum history from the sample obtained by the streak camera. From the spectrum, the self-absorption was observed at the Hα line. For this reason, it is considered that the ablated sample becomes the dense enough. As a result, we estimate the temperature of the sample by fitting the spectrum to the Planck function.

According to the fitting results, we determined the temperature of the sample. It was expected that the sample temperature was increased up to several 1000 K with the pulsed power discharge with isochoric heating during the implosion time scale. For this reason, the WDM could be generated during the implosion time scale with the established system proposed in this study.

4 Conclusion

In this study, the warm dense matter generator by the pulsed power discharge with isochoric heating during the implosion time scale was developed. The intense pulsed power generator was used to input the energy into the sample. Also the optical measurement system was arranged with the simultaneous operation by triggering the discharge pulse. The several 1000 K of the sample was observed by the spectrum from the heated sample, and the temperature and the input energy histories will be able to give the specific head in the WDM state.

Acknowledgment

This work was supported by JSPS KAKENHI Grant-in-Aid for Scientific Research(C) Grant Number 16K06934.

References

[1] Y. KOMATSU, T. SASAKI, T. KIKUCHI, Nob. HARADA, and H. NAGATOMO, *EPJ Web Conf.*, **59**, 04010 (2013).

[2] Y. AMANO, Y. MIKI, T. TAKAHASHI, T. SASAKI, T. KIKUCHI, and Nob. HARADA, *Rev. Sci. Instrum.*, **83**, 085107 (2012).

[3] Y. AMANO, Y. MIKI, T. TAKAHASHI, T. SASAKI, T. KIKUCHI, and Nob. HARADA, *EPJ Web Conf.*, **59**, 16005 (2013).

[4] R. HAYASHI, T. ITO, F. TAMURA, T. KUDO, N. TAKAKURA, K. KASHINE, K. TAKAHASHI, T. SASAKI, T. KIKUCHI, Nob. HARADA, W. JIANG, and A. TOKUCHI, *Laser Particle Beams*, **33**, pp.163-167 (2015).

[5] R. HAYASHI, K. KASHINE, A. TOKUCHI, F. TAMURA, A. WATABE, T. KUDO, K. TAKAHASHI, T. SASAKI, T. KIKUCHI, T. ASO, Nob. HARADA, and W. JIANG, *J. Phys.: Conf. Series*, **688**, 012028 (2016).

[6] R. HAYASHI, T. ITO, T. ISHITANI, F. TAMURA, T. KUDO, N. TAKAKURA, K. KASHINE, K. TAKAHASHI, T. SASAKI, T. KIKUCHI, Nob. HARADA, W. JIANG, and A. TOKUCHI, *J. Phys.: Conf. Series*, **717**, 012063 (2016).

[7] W. JIANG, T. SAKAGAMI, K. MASUGATA and K. YATSUI, *Jpn. J. Appl. Phys.*, **32**, pp.L752-L754 (1993).

[8] T. ITO, R. HAYASHI, T. ISHITANI, Md. SHAHED-UZ-ZAMAN, K. KASHINE, K. TAKAHASHI, T. SASAKI, T. KIKUCHI, Nob. HARADA, W. JIANG, and A. TOKUCHI, *Plasma Fusion Res.*, **12**, 1204024 (2017).

Radiative properties of cold Kα radiation generated by an intense ion beam

Tohru Kawamura, and Fumihiro Koike*

Department of Physics, School of Science, Tokyo Institute of Technology

**Department of Materials and Life Sciences, Sophia University*

ABSTRACT

Examined are spectral properties of cold Kα radiation from low charge chlorine from C_2H_3Cl-plasma heated by an intense ion beam for cold dense plasma diagnostics. Relativistic atomic structure calculations indicate that the Kα lines are slightly shifted to a higher-energy side according to the degree of M-shell ionization. Spectral shift from Cl^+-Kα lines to those with a fully stripped M-shell is about 10 eV, and calculations with a collisional radiative equilibrium (CRE) condition show clear spectral deformation in the electron temperatures of less than 30 eV, where low charge chlorine having M-shell electrons is dominant. Opacity of the Kα lines is small, and the potential to apply for cold dense plasma diagnostics is shown, expecting to give us distinct understandings for energy deposition by an ion beam.

Keywords

heavy ion fusion, energy deposition, opacity, Kα lines, collisional-radiative model, spectral shift, plasma diagnostics

1. Introduction

In heavy ion inertial fusion (HIF) research, energy deposition and plasma heating by ion-beam irradiation is one of critical issues, and many experimental and/or theoretical studies have been intensively done [1, 2]. In the related experiments, Time-Of-Flight (TOF) is one of the most powerful diagnostics in the framework of particle diagnostics [3, 4]. In the category of X-ray diagnostics, which is also one of promising tools for the above purpose, Rzadkiewicz *et al.* [5] experimentally showed direct observation of Si-Kα lines from atomic states with L-shell vacancies and chemical bounding with neighbor oxygen. Their study may lead us fruitful understandings for energy deposition by an ion-beam, and have a potential to open a new field of cold and/or warm dense matter physics. In the study of Ref. [6], Cl-Kα spectra from polyvinyl-chloride (C_2H_3Cl) plasma, which is often used in laser-produced-plasma (LPP) experiments and chlorine is doped as a tracer, heated by a He^{2+}-beam were examined for cold dense plasma diagnostic, and a threshold temperature (~85 eV) was found. The created plasma-temperature must be lower than the threshold to trace energy deposition by an incident ion beam since the K-shell ionization by an ion beam governs the kinetics of the Kα radiation below the threshold. In such a case, Kα radiation with a lower charge state is preferred. Recently, the demonstration of Kα lines from low charge states chlorine having M-shell electrons, which are Cl+~Cl^{7+} and called

'cold-Kα lines' hereafter, is examined for cold plasma diagnostics [7]. M-shell Ionization between lower charge states results in small spectral shift of line radiation. Kα radiation is due to an atomic transition between L and K-shells, and the resultant spectral shift by M-shell ionization is much smaller than that by L-shell ionization. It should be note that Kα lines with partially ionize L-shell are well-separated with respect to the charge states, and essentially applicable to moderately hot plasma diagnostics. In this paper, our study on Kα lines from low charge chlorine, which has M-shell electrons, embedded in C_2H_3Cl-plasma is briefly presented.

2. Descriptions on Population Kinetics and Spectral Synthesis

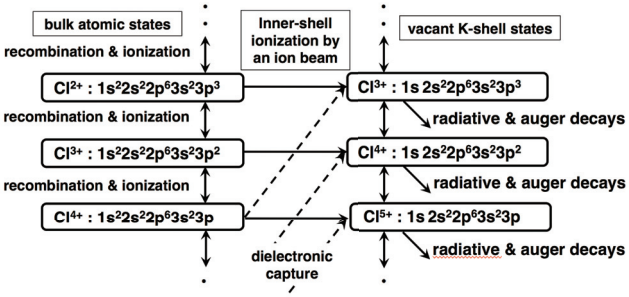

Fig.1 Model of population kinetics.

The model of population kinetics considered here is presented in Fig.1. Vacant K-shell states are mainly created through inner-shell ionization by ion impacts rather than dielectronic-capture in cold plasma. In the figure, although only the creation of a K-shell vacancy is given, L-shell vacancy can be also created in the same manner. The vacant L-shell states play an important role to absorb the Kα emission. Non-radiative processes KLL-, KLM-, KMM- and LMM-Auger transitions are considered for the estimation of net Kα emission. These Auger transitions compete with Kα transitions. The LMM-Auger is for vacant L-shell states and the others are for vacant K-shell states. In solid density plasma heated by an ion beam, since the population of vacant K-shell states is very small, the total average charge state of chlorine $Z_{total} \sim Z_{bulk} \sim Z_{vacant\ K\text{-}shell} - 1$ [8], where Z_{bulk} and $Z_{vacant\ K\text{-}shell}$ stand for the average charge states of bulk and vacant K-shell states, respectively. Here, it should be noted that Fig.6 in Ref. [6] gives an intensity ratio between cold-Kα radiation and high charged one, and the ratio can be an effective index to deduce an electron temperature T_e in the range of 50 – 100 eV, in which the ratios give almost 0.1 - 10. For mostly $T_e < 50$ eV, it is suggested that only cold-Kα lines, which come from atomic states having M-shell electrons and the charge states are less than 8, are applicable.

Calculations are carried out with a collisional radiative equilibrium (CRE) condition. The model of population kinetics considered here is based on those presented in Kawamura *et al.* [7,8]. The cross-sections of collisional excitation and ionization by electron impacts are found in the references in Ozawa *et al.* [9]. Radiative recombination can be estimated by the detailed balance principle with use of the cross-sections of photo-ionization, which can be also found in the article. Collisional de-excitation and three-body recombination are calculated by the detailed balance principle with the corresponding inverse processes. The cross-sections of K- and L-shell ionizations by ion impacts are respectively calculated by Rice *et al.* [10] and Hansteen *et al.* [11].

The ionization degrees of other elements, namely carbon and hydrogen, are estimated with a scaling formula based on the Thomas-Fermi model developed by More [12]. Pressure ionization [13] corrected in terms of Kawamura *et al.* [14], and continuum lowering [15] models are adopted. Concerning the spectral line-shape modeling, a dynamical effect on the Stark broadening is adopted [16]. Resultant spectral profiles are convolved by electron impact broadening using a semiclassical expression [17], natural and Doppler broadenings assuming that ion temperature is equal to electron temperature. Finally, to estimate the opacity of Cl-Kα with low charge states, a radiative transfer equation under one-dimensional stationary and spatially uniform plasma is solved.

3. Calculation of Kα Lines with use of a Relativistic Atomic Structure Program

Emission energies and oscillator strengths of cold-Kα lines are calculated with the use of GRASP92 and RATIP codes. These codes are based on a multi-configuration Dirac-Fock (MCDF) method [18, 19, 20]. Calculated Cl-Kα lines are associated with the charge states of Cl^{+} - Cl^{8+}, and they come from ground states with a vacant K-shell, namely, Cl^{+}: $1s2s^22p^63s^23p^5$ -> $1s^2s^22p^53s^23p^5$ + hν, Cl^{2+}: $1s2s^22p^63s^23p^4$ -> $1s^22s^22p^53s^23p^4$ + hν , … , Cl^{8+}: $1s2s^22p^6$ -> $1s^22s^22p^5$ + hν. The resultant $K\alpha_1$ and $K\alpha_2$ are found to be calculated within the accuracy of ~0.5 eV compared with one of available data [7].

4. Spectral Properties of Cold-Kα Lines

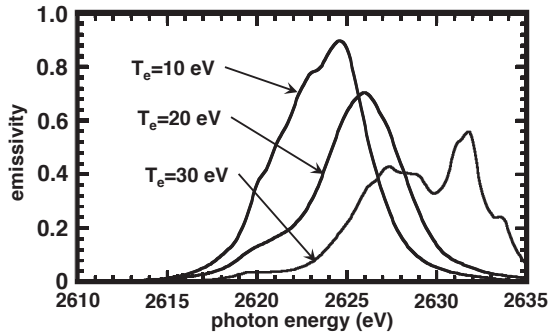

Fig.2 Deformation of a spectral line-shape and blue-shift of cold Cl-Kα radiation emitted from a polyvinyl-chloride (C_2H_3Cl) plasma. The vertical scale is an arbitrary. However, that at T_e = 10 eV is scaled down more to make direct comparison with others. The actual scale at T_e = 10 eV is two times larger.

The typical deformation of a spectral line-shape on the electron temperature is given in Fig.2. The figure shows dynamical Stark profiles, which are without radiative transfer calculation, and the spectra are given with the unit of emissivity. In the calculation, it is assumed that plasma ion density is solid density (~8.1 x 10^{22} cm^{-3}), and incident ion-beam is a C^{6+}-beam, of which current density and mean energy respectively are 3 kA/cm^2 and 30 MeV. Energy spread of the beam is 10% of the mean energy, which is described by Maxwellian. It should be noted that the emissivity at T_e = 10 eV must be scaled down to make direct comparison with others, and the actual scale of it must be multiplied by two.

As seen in Fig.2, at electron temperature T_e = 10 eV, the spectrum mainly consists of three Kα components of Cl^{+} - Cl^{3+}. With increase in T_e, the charge states of the main components are Cl^{2+} - Cl^{5+} at T_e = 20 eV, and the Kα lines from Cl^{4+} - Cl^{8+} have a large contribution at T_e = 30 eV. Finally, total blue-shift at 30 eV from the Kα lines of Cl^{+} is ~10 eV, and clear spectral deformation can be observed.

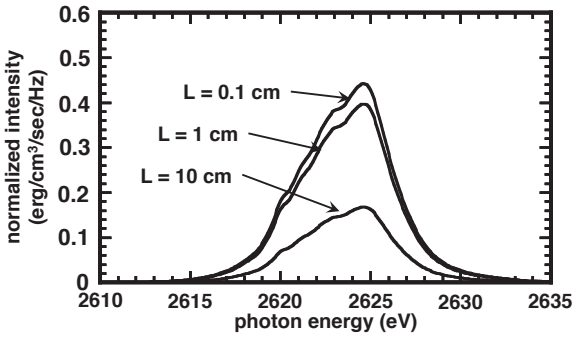

Fig.3 Calculated Cl-Kα spectra at T_e = 10 eV with L = 0.1 cm, 1 cm, 10 cm. All spectra are normalized by L to make direct comparison.

To examine the saturation phenomenon of low charge state Cl-Kα lines, one-dimensional radiative transfer calculations with stationary and spatially uniform plasma are carried out. In Fig.3, Cl-Kα spectra at T_e = 10 eV with some plasma lengths L are given. All the spectra are normalized by L to make direct comparison. With L < 0.1 cm, there is almost no difference among the profiles. In this case, L = 1 cm is almost an upper limit for opacity-free diagnostics.

5. Conclusions

In this study, our recent progress on plasma diagnostics with use of cold-Kα radiation is given. To utilize the radiation, clear blue-shift of cold-Kα lines must be examined with accurate numerical

simulation. In the calculation, the line-shift gives about 10 eV in accordance with M-shell ionization for chlorine, and the clear deformation of spectral shape can be seen, and cold-Kα radiation is shown to be one of promising tools for cold dense and large volume plasma diagnostics.

References

[1] D. H. H. Hoffmann, K. Weyrich, H. Wahl, D. Gardés, R. Bimbot, and C. Fleurier, *Phys. Rev. A* **42**, pp.2313-2321 (1990).

[2] T. Peter, and J. Meyer-ter-Vehn, *Phys. Rev. A* **43**, pp.1998-2014 (1991), *ibid*. **43**, pp.2015-2030 (1991).

[3] M. Ogawa, U. Neuner, H. Kobayashi, Y. Nakajima, K. Nishigori, K. Takayama, O. Iwase, M. Yoshida, M. Kojima, J. Hasegawa, Y. Oguri, K. Horioka, M. Nakajima, S. Miyamoto, V. Dubenkov, and T. Murakami, *Laser Part. Beams* **18**, pp.647-653 (2000).

[4] J. Hasegawa, N. Yokota, Y. Kobayashi, M. Yoshida, M. Kojima, T. Sasaki, H. Fukuda, M. Ogawa, Y. Oguri, and T. Murakami, *Laser Part. Beams* **21**, pp.7-11 (2003).

[5] J. Rzadkiewicz, A. Gojska, O. Rosmej, M. Polasik, and K. Slabkowska, *Phys. Rev. A* **82**, pp.012703 (2010).

[6] T. Kawamura, K. Horioka, and F. Koike, *Laser Part. Beams* **24**, pp.261-267 (2006).

[7] T. Kawamura, K. Horioka, and F. Koike, *Laser Part. Beams* **29**, pp.135-140 (2011).

[8] T. Kawamura, H. Nishimura, F. Koike, Y. Ochi, R. Matsui, W. Y. Miao, S. Okihara, S. Sakabe, I. Uschmann, E. Förster, and K. Mima, *Phys. Rev. E* **66**, pp.016402 (2002).

[9] T. Ozawa, S. Yamamura, N. Tatsumura, K. Horioka, and T. Kawamura, *Phys. Plasmas* **19**, pp.063302 (2012).

[10] R. Rice, G. BasBas, and F. D. Mcdaniel, *Atomic Data Nucl. Data Tables* **20**, pp.503 (1977).

[11] J. M. Hansteen, O. M. Johnsen, and L. Kocbach, *Atomic Data Nucl. Data Tables* **15**, pp.503 (1975).

[12] R. M. More, in *Advanced in Atomic and Molecular Physics*, edited by D. Bates and B. Bederson (Academic Press, Inc. 1985), Vol.**21**, pp.305.

[13] G. B. Zimmerman and R. M. More, *J. Quant. Spectrosc. Radiat. Transf.* **23**, pp.517 (1980).

[14] T. Kawamura, K. Mima, and F. Koike, P*hys. Plasmas* **6**, pp.3658 (1999).

[15] J. C. Steward and K. D. Pyatt, *Astrophys. J.* **144**, pp.1203 (1966).

[16] A. Calisti, C. Mossé, S. Ferri, B. Talin, F. Rosmej, L. A. Bureyeva, and V. S. Lisitsa, *Phys. Rev. E* **81**, pp.016406 (2010).

[17] H. Griem, M. Blaha, and P. C. Kepple, *Phys. Rev. A* **41**, pp.5600 (1990).

[18] F. A. Parpia, C. Froese Fischer, and I. P. Grant, *Comput. Phys. Commun.* **94**, pp.249 (1996).

[19] S. Fritzsche, *J. Electr. Spec. Rel. Phenom*. **114-116**, pp.1155 (2001).

[20] S. Fritzsche, *Phys. Scr.* **T100**, pp.37 (2002).

A Study on the Dynamics of Laser Ablation Plasma in Vacuum

Shotaro Kittaka[a], Tatsuya Sodekoda[a,d],
Jun Hasegawa[a,b], Tohru Kawamura[a,c], Kazuhiko Horioka[a,b]

[a)] *Department of Energy Sciences, Tokyo Institute of Technology, Midori-Ku, Yokohama 226-8502, Japan*
[b)] *School of Engineering, Tokyo Institute of Technology, Midori-Ku, Yokohama 226-8502, Japan*
[c)] *School of Science, Tokyo Institute of Technology, Midori-Ku, Yokohama 226-8502, Japan*
[d)] *Research Laboratory, IHI Corporation, Isogo-Ku, Yokohama 235-8501, Japan*

Abstract

Dynamics of laser ablation plasma in vacuum was discussed for incident intensities less than ~ 10^9 W/cm^2. Results showed that the ablation plasma is accompanied by charge flows from the laser ablation plasma to a grounded target. The current signals, directly measured by a current monitor, developed from negative to positive depending on the dynamically evolving plasma. Results also showed that, initially the current is induced by an electron flow from the plasma plume to the surrounding wall and, after a transient phase, the current is replaced by ion flow to the wall. This result reflects a breaking of quasi-neutral state of the ablation plasma during the evolution and corroborates a generation of ambipolar electric field (double layer) during the ablation process.

Keywords: laser ablation, double layer, sheath, two-electron temperature, ion acceleration

1. Introduction

Laser ablation plasmas made by moderate irradiation level are used in a wide variety of scientific and industrial fields. Behaviors of the plasma plume in vacuum are usually estimated with the well-known solution of gas-dynamic equations [1,2]. Although the velocity distribution of ions in the plasma play an important role for high flux beam sources of charged particles [3,4], and plasma applications such as deposition of thin films and/or surface treatments, their transient behaviors are not clarified yet. In particular, the extraordinarily fast drift speed of ions has been one of the unclarified issues of the ablation plasma expanding into vacuum [5]. Although the plasma shields the laser irradiation, the plasma can interact with the target. In addition to the hydrodynamic acceleration scheme, a theoretical model of metallic target ablation considering electron emission from the hot target as well as an electric sheath produced at the target-plasma interface was proposed [6].

In connection with a study on the acceleration mechanism, transient processes induced by the evolution of ablation plasma in vacuum are of primary concern of this report. One of the purpose of this report is to show an evidence of the charge flows induced by the dynamically evolving plasma. The charge flows to a grounded target were measured directly using a current monitor and/or a charge collector probe.

2. Experimental Arrangement and Plasma Flux Measurements

A schematic diagram of the experimental arrangement for the plasma flux measurements is shown in Fig. 1. A frequency-doubled Nd:YAG laser irradiated

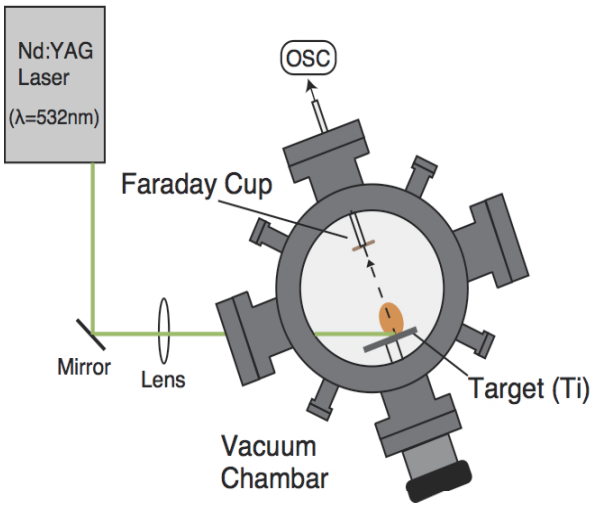

Fig. 1. Schematic of experimental setup for plasma flux measurements.

e-mail: khorioka@es.titech.ac.jp

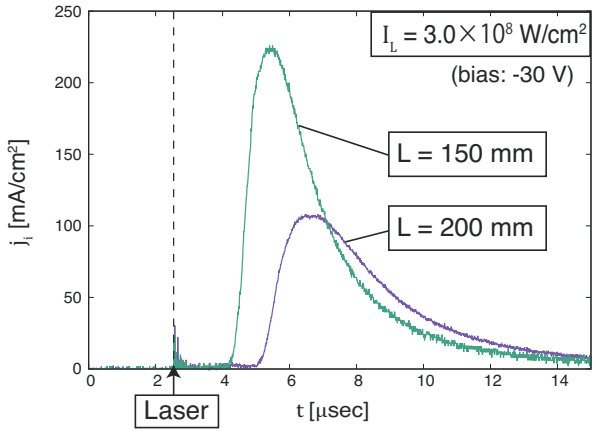

Fig. 2. Waveforms of plasma flux made by laser irradiation with I_L = 3.0 × 10^8 W/cm^2 and S = 1.73 mm^2, at L = 150 mm and 200 mm.

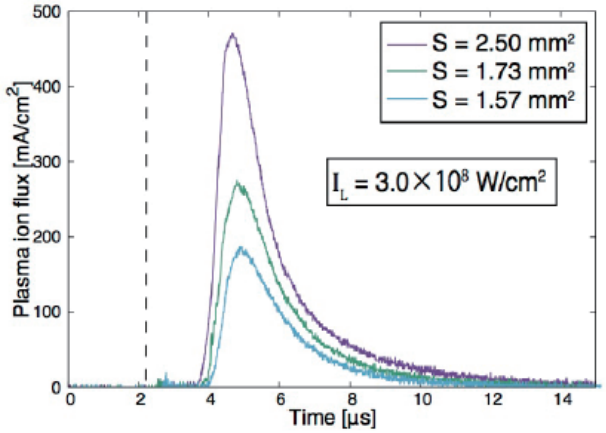

Fig. 3. Dependence of plasma flux on laser spot size with constant irradiation intensity (at L = 150 mm).

a solid titanium (Ti) plate through a lens (f = 300 mm) with a pulse energy of 115 mJ, a pulse width of 15 ns, and an irradiation power density of I_L = 1.3-3.0 × 10^8 W/cm^2. The plasma flux was measured by a Faraday cup located L = 50 mm to 300 mm downstream from the target. The background pressure of the chamber made of stainless steel was kept less than 10^{-3} Pa throughout the experiments.

Typical waveforms of the plasma flux at L = 150 mm and 200 mm are shown in Fig. 2 where the reproducibility was with the line width of the waveform. As is well known, the flux has a drifted-Maxwellian form and the plasma particles dispersed with the propagation. Then the distribution function of ions are composed of fast (drift) and thermal (random) components.

Figure 3 shows waveforms of the plasma flux at L = 150 mm where laser spot size at the target: S was changed as a parameter. As can be seen, when we increase the spot size, the rise time and the flight times for the peak values of the flux-waveforms decreased. The spot size dependence indicates that hydro-dynamical process plays a role for the dynamics of ablation plasma. The plume evolution includes two stages: in the initial stage, where the laser spot size is large enough compared with the plasma thickness, the expansion is one-dimensional, and after some time, when the plasma plume is far from the target, the expansion plume becomes three-dimensional. The transition from the 1D to the 3D behaviors depends on the distance normalized by the spot size.

In the frame of fluid dynamical theory, the ions can be accelerated, by transforming their enthalpy to kinetic energy, up-to the thermal speed at stagnation state [7,8]. This means the maximum speed: u_{max} of the particles is:

$$u_{max} \approx \sqrt{\frac{2\gamma}{\gamma-1}\frac{RT_0}{m}} = \sqrt{\frac{\gamma}{\gamma-1}}\,a \qquad (1)$$

where γ is the specific heat ratio, R is the gas constant, T_0 is the stagnation temperature, m is the mass of particle, and a is the sound speed. This means, in the frame of fluid dynamical theory, the ions can be accelerated up to an order of the sound speed at stagnation temperature [7].

We can estimate the attainable temperature using a simplified model, in which the power balance between the laser intensity: I_L of 10^9 W/cm^2 and the radiation power loss from the plasma is solved, without considering the latent heats for vaporization, excitations, ionization processes, and fluid-dynamical effect, the electron temperature is estimated to be 10 eV at most.

At the intensity level of this experiments, the initial temperature of the ablation plasma: T_0 is estimated to be a 10 eV at most. However, as shown in Fig. 2 and Fig. 3, the flux peak arrived the collector at L = 150 mm with time-of-flight of 3.3 μs. Then the ion energy corresponding to the flux peak is estimated to be $(1/2)m_i v_i^2$ ~ 520 eV, which is an order of magnitude larger than that predicted by the hydro-dynamical acceleration mechanism at this laser irradiation level.

3. Direct Measurements of Charge Flows from the Plasma to the Target

Figure 4 shows the arrangement for the charge flow measurements [9]. In order to measure the charge flow, the Ti target was electrically isolated from the vacuum chamber except a connection to the ground by a cable, around which a Rogowski type current monitor (R.G.) was placed. Also, to change the boundary condition for the plasma plume, a charge collector probe composed of a brass disk with 10mm in diameter was placed at L = 150-200 mm from the Ti plate.

Figure 5 shows typical signals from the current probe. As shown, the currents were negative (electron flow from

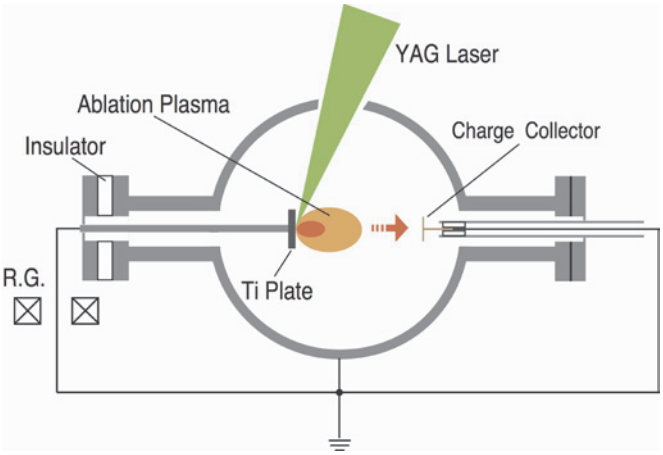

Fig. 4. Experimental arrangement for measurements of charge flow to the laser target.

the target) at the initial phase, and after that they were replaced with positive signals (ion flow to the boundary wall). The negative peak increased with increase of the laser intensity. Also the positive part slightly depended on the laser intensity. The results clearly show that the ablation plume is breaking quasi-neutrality and the plasma potential fluctuates depending on the plume evolution.

For quasi-neutral plasma, the potential ϕ satisfies the Poisson equation:

$$\varepsilon_0 \frac{\partial^2 \phi}{\partial x^2} = e(n_e - Zn_i) \qquad (2)$$

where Z is the charge of ions. Then the dense plasma is separated by a sheath from the target across which the potential drop is formed.

In order to characterize spatial distribution of the charge flows, effects of conductive boundary on the current signals were investigated. For the characterization, we changed the position of charge collector probe shown in Fig. 4, and measured the dependence of the current waveforms on L. As shown in Fig.4, in these measurements, the collector probe was also directly grounded and detected the charge flux to ground potential within a narrow solid angle to the target normal.

The waveforms depended on the laser intensity and the distance between the target to the probe. Examples of the waveforms are shown in Fig.6. As shown in the figure, when we decreased the distance L, the current peak increased. These results indicate that the charge flows are induced by the dynamic behavior of the plasma plume. The sharp increase of the first peak of the current signal for smaller L is due to increase of the solid angle of the charge collector toward the plasma. The dependence of charge flow waveforms on L reflects dynamically evolving un-isotropic current distribution.

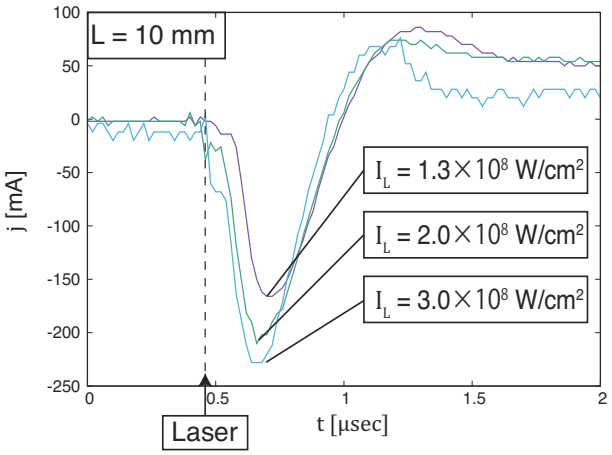

Fig. 5. Current signals through ablation target to the ground potential.

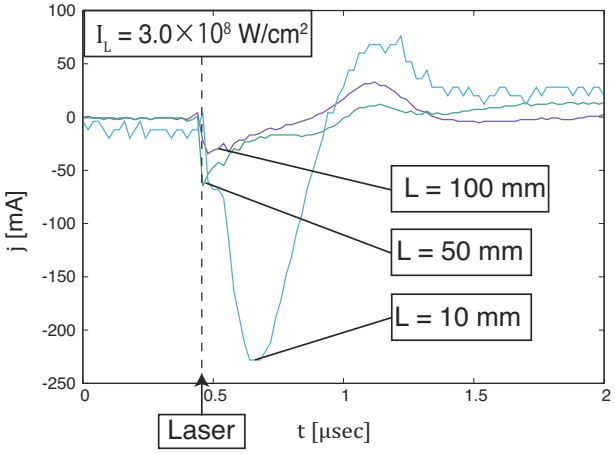

Fig. 6. Dependence of the target-to-ground current on the collector distance L.

Negative signals are probably due to energetic electrons escaping from the plume boundary and the positive signals are from ion flows induced by the potential hump induced in the plume [10]. Although a hot electron population is considered to be critical for producing double layer structure [11], electrostatic probe measurements indicated existence of the hot electron component in the laser ablation plasma under similar experimental condition [4]. Absorption of laser radiation and rapid expansion in vacuum right after the absorption, are probably essential to form the energetic electrons, two-electron temperature components, and the breaking of quasi-neutral state in laser ablation plasma.

4. Concluding Remarks

The charge separation effects in the collision-less plasma expansion into a vacuum have been studied extensively concerning high-energy ion jets from short-pulse interaction with target [12]. The effects seem to play some roles also in the plasma expansion made by moderate intensity level as has been shown in this study.

In this work, charge flows to the ground potential from the ablation plasma were measured directly using a current monitor. The current signals through the grounded target do not disturb the plasma potential. Then the results reflected the transient structure of the ablation plume in vacuum. Also the results could corroborate a breaking quasi-neutrality in the ablation plume, effect of energetic electrons, and ambipolar electric field arising during the expansion of ablation plume. Results also indicated that not only hydro-dynamical mechanism but the ambipolar electric field induced in the ablation plasma contribute the acceleration of ions in the plasma.

The final goal of this study is to clarify the acceleration mechanism of the fast ions and to derive the velocity distribution function of ions under the moderate irradiation levels (10^8-10^9 W/cm^2) which is useful for high-flux ablation type ion sources, and reliable laser triggering of pulsed discharges.

References

[1] S.I. Anismov, D. Bauerle, B.S. Luk'yanchuk, *Phys. Rev.* B., **Vol.48**, 12076-12081 (1993).

[2] R. Kelly, *Phys. Rev.* A, 46, 860-874 (1992).

[3] S.Ikeda, K.Horioka, M.Okamura, *IEEE Trans. Plasma Sci.*, **Vol.43**, 3456 (2015).

[4] Y. Sakai, T. Itagaki, K. Horioka., *Phys. Plasmas*, **Vol.23**, 123112 (2016).

[5] N.M. Bulgakova, A.V. Bulgakov, O.F. Bobrenok, *Phys. Rev. E*, **Vol.62**, No.4, pp.5624-5634 (2000).

[6] I.I. Beilis, *IOP Publishing for Sissa Medialab*, 1-11 (2016).

[7] H.W. Liepmann and A. Roshko, *Elements of Gasdynamics*, Wiley, New York, (1957).

[8] Q. Zhu, J. Yamada, N. Kishi, et.al.; *Jpn. J. Appl. Phys.*, **Vol.49**, 056201 (2010).

[9] S. Kittaka, T. Sodekoda, J. Hasegawa, K.Horioka, *Plasma and Fusion Research*, 12: 1201014 (2017).

[10] F. Isono, M. Nakajima, J. Hasegawa and K. Horioka, *Phys. Plasmas*, **Vol.22**, 084501 (2014).

[11] G. Hairapetian and R.L.Stenzel, *Phys. Fluids B*, **Vol.3**, No.4, 899 (1991).

[12] P. Mora, *Phys. Rev. Letters*, **Vol.90**, 185002-1-4 (2003).

Study on interaction of pulsed-power-driven plasma flow and perpendicular magnetic field

Taichi Takezaki, Yutaro Hatakeyama, Kazumasa Takahashi,
Toru Sasaki, Takashi Kikuchi, and Nob. Harada

Nagaoka University of Technology
Kamitomioka 1603-1, Nagaoka Niigata 940-2188, Japan

ABSTRACT

To understand particle acceleration mechanisms in non-relativistic collisionless shocks, we have investigated an interaction between a pulsed-power-driven plasma flow and a perpendicular magnetic field. The ion current from the plasma flow in the perpendicular magnetic field was measured by an ion collector. The valuation of the ion current waveform without and with the perpendicular magnetic field was observed. With the magnetic field, the ion current preceding the main current was observed. Results of numerical simulation based on an electromagnetic hybrid particle-in-cell method qualitatively agreed with experimental results.

Keywords

Plasma focus, laboratory astrophysics, hybrid particle-in-cell

1. Introduction

Elucidation of generation process of cosmic rays is important issue in astrophysics and space physics. The characteristic of cosmic rays is non-thermal energy distribution with a power-law spectrum, and the highest energy of cosmic rays reaches to 10^{20} eV [1]. Collisionless shocks such as heliospheric shocks or supernova shocks have been discussed to play an energy source for generation of cosmic rays [2-4]. In the relativistic region, first-order Fermi acceleration, which is a theoretical model of particle acceleration in collisionless shocks, has been explained the power-law energy distribution of cosmic rays and the process how to gain the energy from electromagnetic fields [5-6]. However, to drive first-order Fermi acceleration, charged particles must be accelerated from the non-relativistic region to the relativistic region. The process for driving first-order Fermi acceleration have been not clarified because of the non-linear interaction of electromagnetic fields and the charged particles [7-8]. In order to clarify particle acceleration mechanisms in non-relativistic collisionless shocks, the understanding of behaviors and interactions of plasma flow and electromagnetic fields in non-relativistic region is required.

A plasma flow with a similarity for astrophysical phenomena in a laboratory scale experiment provides "in-situ" observation of the astrophysical phenomena [9-11]. The similarities of the laboratory scale experiment to the astrophysical phenomena, such as a mean free path of particles, the velocity of the plasma flow, or plasma beta are considered. To obtain a fast plasma flow in a laboratory, experiments using laser ablation or pulsed-power discharge has been carried out [12-18]. We have proposed a tapered cone plasma focus device to obtain a quasi-one-dimensional fast plasma flow for laboratory astrophysics [19-20].

In this study, to understand an interaction between fast plasma flow and perpendicular magnetic field, we have investigated behavior of a one-dimensional plasma flow generated by the tapered cone plasma focus device in a perpendicular B-field by measuring a plasma ion current. A numerical simulation based on an electromagnetic hybrid particle-in-cell method has been carried out for the comparison with the experimental results.

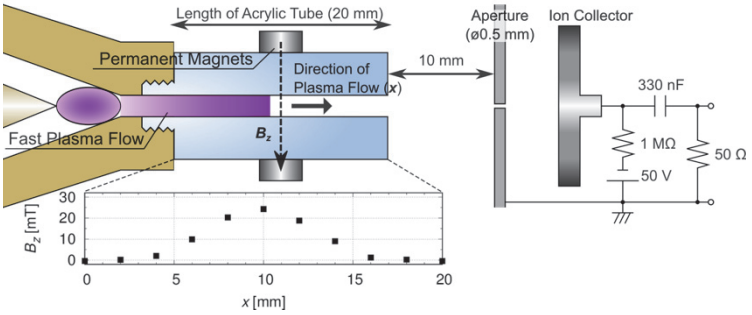

Fig. 1 Schematic image of the experimental setup to apply the perpendicular *B*-field using permanent magnets and to measure the plasma ion current using the ion collector (IC).

2. Experimental Setup

The tapered cone plasma focus device with a guiding acrylic tube (length of 20 mm) produces a quasi-one-dimensional fast plasma flow with the velocity of 30 km/s in a helium gas discharge at 0.3 Pa [20]. Figure 1 shows the experimental setup to apply an external perpendicular *B*-field, and to investigate ion behavior. In order to apply a magnetic field B_z perpendicular to the plasma flow direction x, permanent magnets were set on the acrylic tube. The peak of the *B*-field is 25 mT at the center of the acrylic tube. To measure a plasma ion current from the plasma flow, an ion collector (IC) biased at –50 V with an aperture of ø0.5 mm was set coaxially to the electrodes and the acrylic tube. The distance from the end of the acrylic tube to the aperture is 10 mm. The ion current was measured through a high-pass filter with the cutoff frequency of 10 kHz.

3. Results and Discussions

3.1 Measurement of the plasma ion current without and with the perpendicular magnetic field

Figure 2 shows the plasma ion current measured by the IC without and with the perpendicular *B*-field. Without the *B*-field, the initial distortion has been detected at 3.9 μs, and the current has reached to the peak of 70 mA at 4.8 μs. The time from the initial distortion to the peak is 0.9 μs. On the other hand, with the *B*-field, the main ion current has been delayed, and it has been detected at 5.6 μs. The ion current of a few mA preceding the main current was observed.

3.2 Numerical simulation for plasma flow

To simulate the plasma behavior generated by the tapered cone plasma focus device, a numerical simulation based on an electromagnetic hybrid particle-in-cell (PIC) method has been carried out [20]. The ion current at 30 mm is compared with the experimental results as shown in Fig. 2.

Initial conditions for the numerical simulation were decided by the comparison of experimental results. The average velocity of super particles is 30 km/s. We assumed singly ionized helium ions and thermodynamic equilibrium, and thus the electron temperature and electron number density becomes $T_e = T_i$ and $n_e = n_i$.

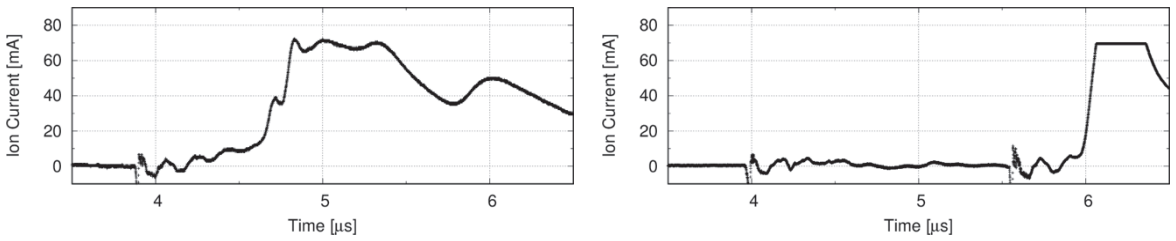

(a) w/o *B* (b) w/ *B*

Fig. 2 Ion current waveform measured by the IC. (a) without the *B*-field and (b) with the *B*-field. Without the *B*-field, the initial distortion was detected at 3.9 μs, and the current reached to the peak of 70 mA at 4.8 μs. The time from the initial distortion to the peak is 0.9 μs. With the *B*-field, the main ion current was delayed, and was detected at 5.6 μs. The ion current of a few mA preceding the main current was observed.

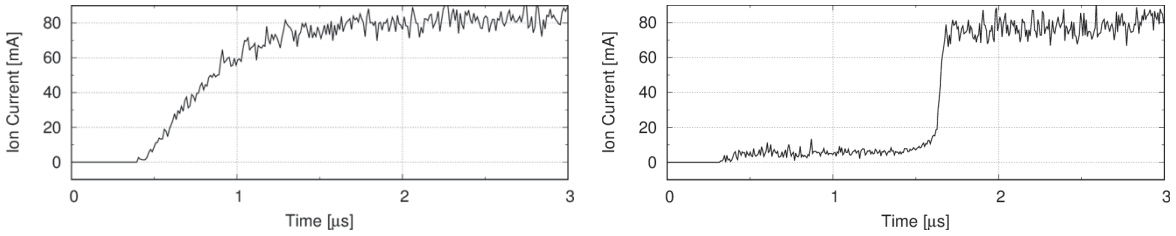

(a) w/o *B* (b) w/ *B*

Fig. 3 Ion current waveform at 30 mm numerically simulated by the electromagnetic hybrid PIC method. (a) without the *B*-field and (b) with the *B*-field. The peak of ion current both without and with the *B*-field were 80 mA. Without the *B*-field, the current was detected from 0.5 μs, and reached to the peak at 1.5 μs. The rising time of the current is 1 μs. With the *B*-field, the current was sharply increased at 1.5 μs, and the current with a few mA preceding the main current was confirmed.

The electron temperature of the plasma flow has been experimentally estimated to be $T_e \sim 2.6$ eV from the optical emission spectroscopy [20]. The ion number density is estimated to be $n_i \sim 10^{20}$ m^{-3} with assuming fully-ionized-plasma of the initial helium gas in the chamber as below; the initial number density of neutral helium in the chamber is calculated by using ideal gas law, $n_{\mathrm{He}} = P_0 / k_{\mathrm{B}}T_0$, where P_0 is the initial gas pressure in the chamber, k_{B} is the Boltzmann constant, and T_0 is the initial temperature. The initial number density of neutral helium is estimated to be $n_{\mathrm{He}} \sim 10^{20}$ m^{-3} with the initial pressure $P_0 = 0.3$ Pa, and the room temperature $T_0 = 300$ K.

Figure 3 shows the ion current waveform at 30 mm numerically simulated by the electromagnetic hybrid PIC method. The ion current I_i was calculated as below:

$$I_i = J_{ix} S_{\mathrm{ap}} \quad (1)$$

where J_{ix} is the ion current density on x direction at 30 mm represented by the super particles, S_{app} is the cross section of the aperture with the diameter of ø0.5 mm. The peaks of the ion current both without and with the perpendicular *B*-field are 80 mA. Without *B*-field, the current has been detected from 0.5 μs, and the peak current has been reached at 1.5 μs. The rising time of the current is about 1 μs. On the other hand, with *B*-field, the current has been sharply increased at 1.5 μs, and the current with a few mA preceding the main current has been confirmed. These results qualitatively agree with the experimental results shown in Fig. 2.

4. Conclusions

We have observed the plasma ion current from the plasma flow generated by the tapered cone plasma focus device both in without and in with the perpendicular *B*-field. Without *B*-field, the peak of the ion current was 70 mA, and the rising time of the current was 0.9 μs. On the other hand, with the *B*-field, the detected time of the main ion current was delayed, and the rising time was shorter than without the *B*-field. In addition, the current of a few mA preceding the main current was observed. The numerical results simulated by the electromagnetic hybrid particle-in-cell method qualitatively agreed with the experimental results.

To investigate the ion behavior in the perpendicular *B*-field, we will evaluate the dependence of the behavior of the ion current on the peak of the *B*-field, and the dependence of the detected time of the ion current on the distance to the detector.

References

[1] S. P. Swordy, “The energy spectra and anisotropies of comic rays”, Space Sci. Rev. **99**, 85, 2001.

[2] W. I. Axford, E. Leer, and J. F. McKenzie, “The

structure of cosmic ray shocks", Astron. Astrophys. **111**, 317, 1982.

[3] L. A. Fisk, "On the acceleration of energetic particles in the interplanetary medium", J. Geophys. Res. **81**, 4641, 1976.

[4] M. A. Lee, "The association of energetic particles and shocks in heliosphere", Rev. Geophys. Space Phys. **21**, 324, 1983.

[5] A. R. Bell, "The acceleration of cosmic rays in shock fronts - I", Mon. Not. R. Astron. Soc. **182**, 147, 1978.

[6] R. D. Blandford, and J. P. Ostriker, "Particle acceleration by astrophysical shocks", Astrophys. J. **221**, L29, 1978.

[7] G. P. Zank, W. K. M. Rice, J. A. Le Roux, and W. H. Matthaeus, "The injection problem for anomalous cosmic rays", Astrophys. J. **556**, 494, 2001.

[8] Y. Ohira, "Cosmic ray acceleration mechanism", JPS Conf. Proc. **15**, 011002, 2017.

[9] R. P. Drake, "The design of laboratory experiments to produce collisionless shocks of cosmic relevance", Phys. Plasmas **7**, 4690, 2000.

[10] D. D. Ryutov, B. A. Remington, H. F. Robey, and R. P. Drake, "Magnetohydrodynamic scaling: From Astrophysics to the laboratory", Phys. Plasmas **8**, 1804, 2001.

[11] A. Stockem, F. Fiuza, A. Bret, R. Fonseca, and L. Silva, "Exploring the nature of collisionless shocks under laboratory conditions", Sci. Rep. 4, 3934, 2014.

[12] A. Bell, P. Choi, A. Dangor, O. Willi, D. Bassett, and C. Hooker, "Collisionless shock in a laser-produced ablating plasma", Phys. Rev. A **38**, 1363, 1988.

[13] C. Courtois, R. Grundy, A. Ash, D. Chambers, N. Woolsey, *et al*., "Experiment on collisionless plasma interaction with applications to supernova remnant physics", Phys. Plasmas **11**, 3386, 2004.

[14] K. Kondo, M. Nakajima, T. Kawamura, and K. Horioka, "Compact pulse power device for generation of one-dimensional strong shock waves", Rev. Sci. Instrum. **77**, 036104, 2006.

[15] Y. Kuramitsu, Y. Sakawa, T. Morita, C. Gregory, J. Waugh, *et al*., "Time evolution of collisionless shock in counterstreaming laser-produced plasmas", Phys. Rev. Lett. 106, 175002, 2011.

[16] K. Adachi, M. Nakajima, T. Kawamura, J. Hasegawa, and K. Horioka, "A table-top pulsed power device for counter-streaming plasma experiments", IEEJ Trans. Fundm. Mater. **135**, 366, 2015.

[17] T. Morita, Y. Sakawa, Y. Kuramitsu, S. Dono, H. Aoki, *et al*., "Characterization of electrostatic shock in laser-produced optically-thin plasma flows using optical diagnostics" Phys. Plasmas **24**, 072701, 2017.

[18] J. S. Ross, D. P. Higginson, D. Ryutov, F. Fiuza, R. Hatarik, *et al*., "Transition from collisional to collisionless regimes in interpenetrating plasma flows on the national ignition facility", Phys. Rev. Lett. **118**, 185003, 2017.

[19] T. Sasaki, H. Kinase, T. Takezaki, K. Takahashi, T. Kikuchi, *et al*., "Laboratory scale experiments for collisionless shock generated by taper-cone-shaped plasma focus device" JPS Conf. Proc. **1**, 015096, 2014.

[20] T. Takezaki, K. Takahashi, T. Sasaki, T. Kikuchi, and N. Harada, "Accelerated ions from pulsed-power-driven fast plasma flow in perpendicular magnetic field", Phys. Plasmas **23**, 062904, 2016.

Effects of Metal on the Formation and the Evolution of Laser-supported Detonation Wave

Seiichiro Yoshioka[a], Jun Hasegawa[a,b], Kazuhiko Horioka[a,b]

Department of Energy Sciences, Tokyo Institute of Technology[a],
School of Engineering, Tokyo Institute of Technology[b],
Nagatsuta 4259, Midori-ku Yokohama, 226-8502

ABSTRACT

Detonation waves were induced by focusing a TEA CO_2 laser in the atmosphere. When a metal was placed close to the focusing spot, the shock front was strengthened and a two-step shock wave was driven. The formation of discontinuous (two-step) shock wave indicated that there is an additional transference mechanism of the energy deposition region to that induced by the shock wave. The images made by a time-resolved interferometry and fast framing photographs indicated an electron emission from the metal. Current measurements confirmed a current spike induced by electrons emission from the metal surface. All of the results strongly indicated that the electron emission plays an important role for the evolution of laser supported detonation wave formed at the region close to metal.

Keywords: **Detonation wave, Shock wave, Laser-induced plasma, Electric potential, Uni-polar arc**

1. Introduction

When a detonation is triggered in a combustible gas, the heated fluid drives a self-evolving fast shockwave: the shock heated region enhances the combustion, the combustion strengthen the shock wave, and vice versa. The phenomena in which a laser-induced plasma and resulting shock wave propagate together is called laser-supported detonation wave (LSD) [1]. The laser absorbing rate enhances at the shock heated region that strengthen the shock wave. Therefore the LSD usually has a similar driving mechanism to that of the detonation wave. However it has a bit complicated structure than the combustion driven one, in which laser induced highly non-equilibrium plasma and the radiation transport induces a highly transient hydro-dynamical motion [2].

The phenomena; LSD itself was already found in 1960's [2] and the fluid dynamic phenomenon induced by the LSD and its basic structure is already known when it is formed in simple conditions such as in gas atmosphere. However, for a phenomena with more complex situation such as LSD driven in existence of a metal boundary, detailed models are still in discussion [4].

The "Light Craft" is famous for the demonstration of propulsion by LSD which succeeded in launching a projectile with about 50 g weight to 120 meters by using a 10kW CO_2 laser [3]. The LSD driver is formed in atmosphere with metal boundary. In the previous experiment, it was observed that when we placed a metal cone, the breakdown threshold decreased and a two-step (discontinuous) shock wave was formed. Also, a streamer-like structure was observed by a fast frame camera in the initial phase [4]. The results indicated that electron emission from the top of the cone plays a role for the evolution of the detonation wave.

To clarify effects of the metal on the evolution of LSD, we tried to make clear the metal induced phenomena using a time-resolved interferometry and a measurements of current through the metal.

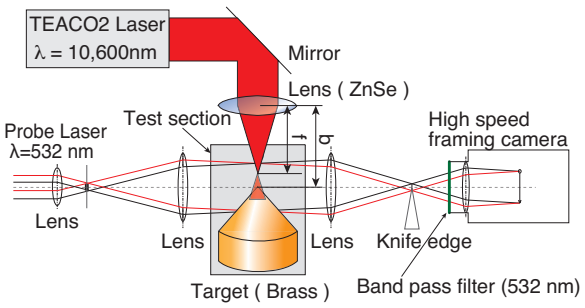

Fig.1. Experimental arrangement for study on CO_2-laser supported detonation.

2. Experimental Setup and Results

2.1 Basic configuration

A schematic of the basic experimental set-up for the LSD experiments is shown in Fig.1. A TEA CO_2 laser (Ushio-Unimark 400; λ = 10,600 nm), was used for inducing the breakdown and driving the LSDs. The laser beam has a cross-section of 20 × 30 mm^2. In the figure, f = 63.5 mm is the focal length of a ZnSe lens and b is the distance between the lens and a conical brass target. We conducted experiments usually under atmospheric air conditions and the laser was focused 4 mm above the top of a conical target (b = 67.5 mm) made of brass. So the F-value of laser optics was 2.3, and the beam waist was estimated to be about 0.031 mm.

Temporal out-put profile of the TEA CO_2 laser was measured by a pyroelectric detector (QS3-H) and the total energy with a joule detector (PHD50). A typical profile of the laser power is shown in Fig. 2.

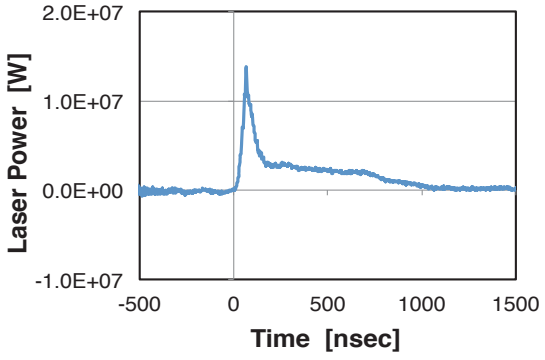

Fig.2. Typical power profile of TEA-CO_2 Laser.

We took the shockwave images with a Schlieren system and a fast framing camera (NAC-Ultra Neo). A semiconductor laser (λ = 532 nm) was used for the probe light of the Schlieren image. A narrow-band path filter (532nm) in front of the fast framing camera lens suppressed the stray light from the laser breakdown plasma.

2.2 Interferometry and Fast-framing Photographs

When we take a fast photograph, we removed the Schlieren optical system, and observed directly the evolution of laser-induced plasma image using the fast framing camera.

In order to measure the electron density inside the detonation wave and also to increase the temporal resolution, we constructed a highly-sensitive, time-resolved Mach-Zehnder interferometer using a Nd: YAG laser (Handy YAG H-700, Quanta System). The second harmonics (λ=532 nm, Δt = 8 nsec) of the laser was used as the light source.

The setup of the interferometer is shown in Fig3. Interference fringes were captured by a CCD camera (D5100, Nikon) and a telephoto lens (AF Micro Nikkor 105 mm f / 2.8 D, Nikon). The focal length of the telephoto lens was set to 0.314 m, F.28, and the sensitivity of the camera was set to the lowest value (ISO 100). The time of the image was estimated by comparing the signal of the pyroelectric detector and the signal of a PIN photodiode. We used two interference filters (VPF - 25C - 03 - 45 - 5 3200, Sigma Koki) in series to improve the SN ratio of the fringe.

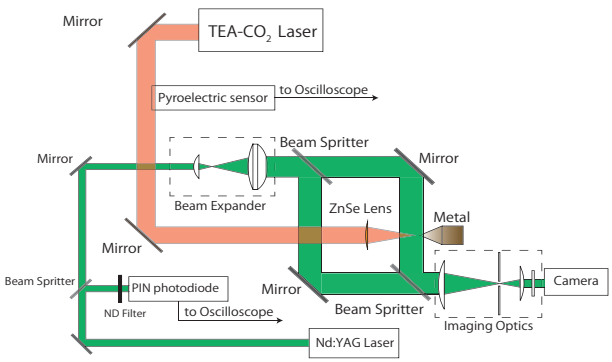

Fig.3. Set-up of time-resolved interferometry.

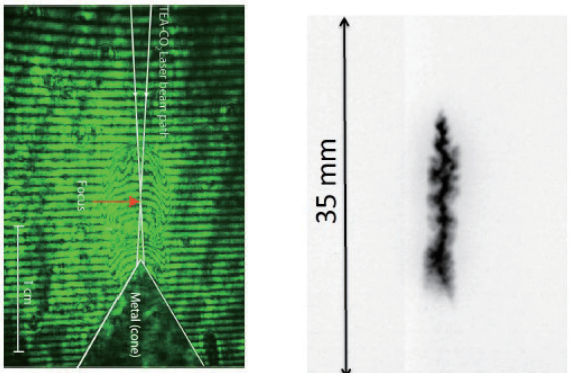

(a) (b)

Fig.4. Schlieren image (a) and fast frame photograph (b) of the laser induced breakdown at an initial stage of LSD.

Examples of the current signals are shown in Fig.7 (a): without aperture, and (b): with aperture. By the interferometry, we could make clear the existence of electrons in the initial stage of laser driven detonation wave.

2.3 Current measurement from the metal

In addition to the imaging experiments, an attempt was made to correlate the images and current emission from the metal. We curried out direct measurements of electron current from the metal.

The arrangement for the current measurements is shown in Fig.5. As shown, the metal cone was supported with electrically insulated metal holder between which a 50 Ω terminating resistor and a BNC cable were connected. That enabled us to estimate the current from the cone to the ground. To investigate the current path, we placed a metal aperture around the top of the cone as shown in Fig.6.

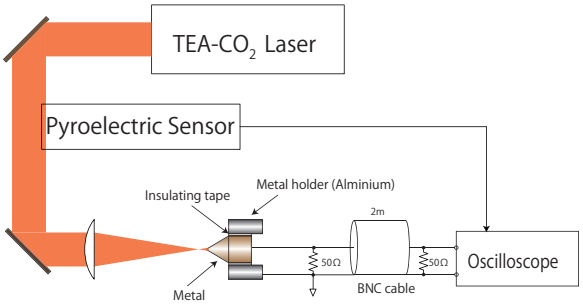

Fig.5. Schematic of the current measurements.

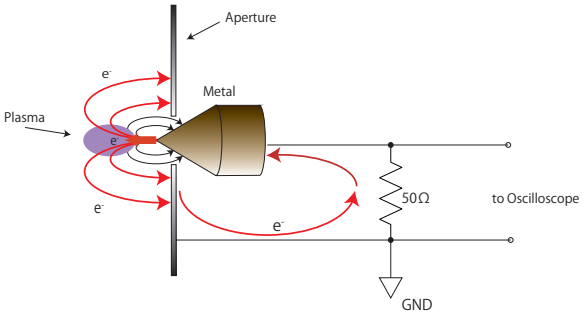

Fig.6. Details of the current measurements.

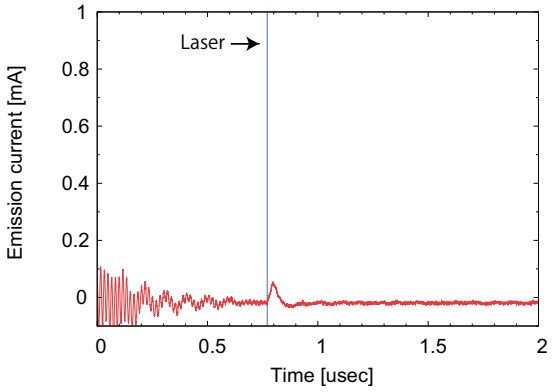

(a)

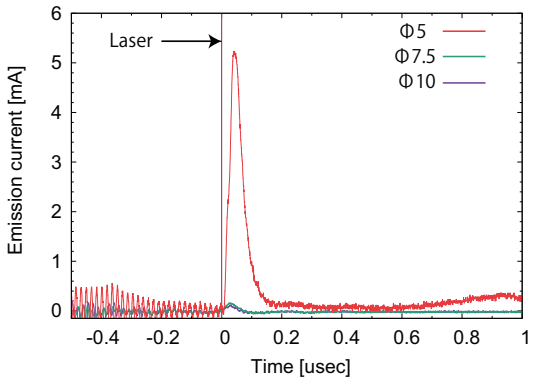

(b)

Fig.7. Current signals through the metal.

As shown in the figures, we observed a current spike at the beginning of the LSD. When we consider the correlation of the current signal, the fringe pattern and the fast frame images in Fig.4, the positive signal indicates electrons emission from the cone.

In order to investigate the current distribution, we placed an aperture at the top of the cone target, as shown in Fig.6. The current signals are shown in Fig.7 (b). As shown, the current signal strongly

depended on the aperture diameter which corroborates the electron emission pattern from the metal cone as illustrated in Fig.6.

3. Concluding Remarks

A memorable idea of laser propulsion was proposed by A. Kantrowits, in which he discussed the capability of a laser launching system of spacecraft from the earth using a rocket model based on laser ablation pressure [5]. In the system, a fast plasma jet and/or a LSD made by laser ablation in a thrust nozzle behind the projectile are used to obtain high specific impulse. The LSD made in the nozzle is the effective driving force for the launching system from the earth [6]. Namely the LSD is considered to be formed in the atmosphere and evolved in a region close to a metal wall. However the role of the metal on the formation and evolution of the LSD was not clarified yet.

We constructed a system for time-resolved interferometry and made clear existence of electrons in the very early phase of the LSD. In this study, an attempt was made to correlate the signal of current emission from metal and the density distribution of electrons. Also we directly measured the current between the breakdown plasma and the metal using an electrical set-up for evaluating the current profile and its distribution.

The results confirmed electron emission with full width at half maximum of 100nsec at a very early phase of LSD. To investigate the current distribution, we placed an aperture at the top of the meatal cone. The current spike increased clearly with decrease of aperture size. The result also support the electron emission from the top of the cone and an electron flow circulating between the plasma and the metal.

All of the results are indicating an important role of electrons from the metal boundary both for the formation and the evolution of LSDs.

The apparently monopolar current flow can be caused by an electrical potential distribution induced by the pressure gradient of a transient breakdown plasma formed close to metal boundary [7]. Investigating further the metal-plasma interaction and making clear the relation between the current flow and the LSD are the future issues.

Acknowledgement

Authors wish to thank Mrs. K.Yonezawa, and K.Kawaguchi, for pioneering experiments concerning this study.

References

[1] T.Endo, J.Kasahara, A.Matsuo et. al., “Pressure History at the Thrust Wall of a Simplified Pulse Detonation Engine”, AIAA J., **Vol.42**, pp.1921-1930 (2004).

[2] S. A. Ramsden and P. Savic: “A Radiative Detonation Model for the Development of a Laser-Induced Spark in Air”, NATURE, **Vol.203**, No.4951, pp.1217-1219 (1964).

[3] L. N. Myrabo, “Brief History of the Light Craft Technology Demonstrator (LTD) Project”, AIP Conference Proceedings, **Vol.664**, No.1, pp.49-60 (2003).

[4] K.Kawaguchi, K.Yonezawa, M.Nakajima, K.Horioka, “Two-Step Spheroidal Shock Wave Driven by TEA-CO2 Laser”, J. Plasma Fusion Res., **10**, 008 (2015).

[5] A. Kantrowitz, ”Propulsion to Orbit by Ground-Based Lasers”, Aeronaut. Astronaut., **Vol.10**, pp.74-76 (1972).

[6] C. Phipps, M. Birkan, W. Bohn, et. al., “Review: Laser-Ablation Propulsion”, JOURNAL OF PROPULSION AND POWER, **Vol.26**, No.4 pp.609-637 (2010).

[7] H.J.G. Gielen, D.C.Schram,”Unipolar arc model” IEEE Plasma Sci., **Vol.18**, pp.127-133 (1990).

Development of an inertial electrostatic confinement neutron source and its application to neutron imaging

Kohei Okutomo[*1], Florian Aymanns[1], Eiki Hotta[1], Kei Takakura[1], Jun Hasegawa[1], Toshiyuki Kohno[2]

[1]*Department of Mechanical Engineering, School of Engineering, Tokyo Institute of Technology*
[2]*Department of Physics, School of Science, Tokyo Institute of Technology*

ABSTRACT

We tested a linear type Inertial Electrostatic Confinement (IEC) neutron source that adopted permanent magnets to enhance ion production rate in the glow-discharge plasma. By introducing magnetic fields locally near the discharge anodes, the neutron production rate (NPR) normalized by background gas pressure increased by a factor of 1.8 and the light emission pattern of the discharge plasma drastically changed. A neutron imaging test was also carried out by using a coaxial cylinder type IEC neutron source. Neutron transmission images were successfully obtained even with a neutron flux of 45 n/s/cm^2, which coincided well with numerical predictions based on Monte-Carlo simulations.

Keywords

compact neutron source, glow discharge plasma, neutron imaging

1. Introduction

A demand for neutron sources has recently been growing in various fields such as air luggage security, landmine detector, boron neutron capture therapy, and so on. Conventional neutron sources based on fission reactor or accelerator technologies, however, are huge and expensive, so these neutron sources have not gained widespread use yet.

The inertial electrostatic confinement (IEC) fusion device is one of potential candidates for a commercially used compact neutron source. It uses high-voltage glow discharge in low-pressure (~Pa) background deuterium gas to produce deuterium ions and accelerate them. Fast neutrons (2.45 MeV) generated by fusion reactions between deuterium nuclei are emitted isotropically from the center of the IEC device and a part of them are used for neutron applications. The neutron sources based on the IEC concept can be very compact and less expensive compared with the conventional neutron sources, various types of IEC devices have been studied for many years since the first pioneering work by Miley *et al*[1].

The most important issue of the IEC neutron source is to improve neutron production rate (NPR). The champion record of NPR achieved by the IEC devices ranges from 10^7 to 10^8 neutrons/s. On the other hand, the demand for NPR in practical applications is typically more than 10^9 n/s. Until the kinetic energy (E) of deuterium nuclei become 150 keV, the DD fusion cross-section (σ) increases as $\sigma \propto E^n$ ($n > 1$). So, it is necessary to efficiently use the applied voltage to accelerate deuterium ions. Since the maximum kinetic energies of the ions is determined by the positions where those ions are initially produced. Controlling the ion production location in the IEC plasma is also an important issue. In the previous work, various types of ion sources were proposed and tested to actively supply deuterium ions to IEC devices [2-5].

This paper reports experimental results on both the operation characteristics of a linear-type IEC source and the demonstration of neutron imaging using a cylindrical type IEC source.

2. Preliminary test of a linear-type IEC device

A schematic of the linear-type IEC device is shown in Fig. 1. A hollow cathode (60 mm in inner diameter, 100 mm in outer diameter, and 100 mm in length) made of stainless steel was mounted in the center of a vacuum chamber and biased to negative high voltage through a high-voltage feedthrough. A couple of disk anodes (140 mm in diameter) made of stainless steel were located coaxially with respect to the hollow cathode with a gap length of 110 mm. The discharge region between the electrodes were surrounded by eight stainless steel rods (ø6 mm), which were arranged in parallel with the center axis of the cathode and anodes with the same interval in the azimuthal direction. The anodes and the rods were connected to the grounded vacuum chamber.

To enhance ion production rate near the anode, a magnetic field was locally introduced by putting a permanent magnet (samarium-cobalt) on the back of the anode disk as shown in Fig. 2. Since electrons travelling toward the anode are trapped by the magnetic field and their flight distances increase due to $E \times B$ drift motion, we can expect that the rate of ion production by electron impact ionization enhances. This effect can localize the ion production near the anode where the potential is relatively high, thus contributing to the increase of NPR accompanying with the increase in the average kinetic energy of ions at the cathode.

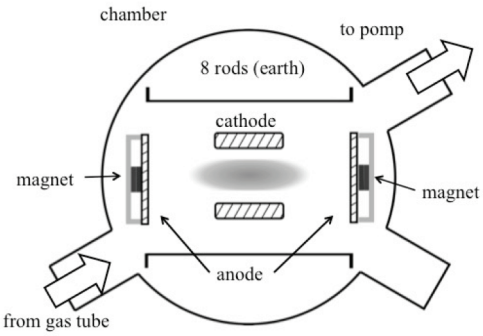

Fig. 1. Experimental setup.

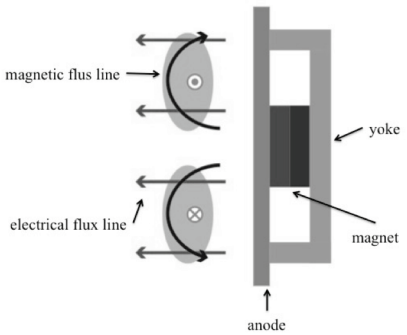

Fig. 2. A schematic of magnetron discharge for ion production near anodes.

The cathode was connected to a high voltage power supply and biased up to –40 kV. The power supply was operated in a constant current mode with a discharge current of 5 mA or 13 mA. The discharge voltage was changed by changing the deuterium/hydrogen gas pressure from 0.92 Pa to 1.83 Pa, which was controlled by a solenoid valve in the gas feed line.

Figure 3 plots the operating voltage as a function of the gas pressure. The voltage values with the anode magnets (solid lines) and those without the magnets (dotted lines) are plotted for two different discharge current conditions, 5 mA and 13 mA. In both conditions, the operating voltage decreased by introducing the magnets to the anodes, indicating that that the glow discharge is more easily sustained by induced magnetic fields around the anodes. This result is probably attributed to the increase in electron mean flight distance in the gap, which results from their gyrokinetic motions in the magnetic field.

Figure 4 shows the observed neutron production rate (NPR) normalized by background gas pressure. It is known that the DD fusion reaction rate between ions and background neutral atoms is much larger than that between ions in the IEC devices [6]. Thus, by using the normalized NPR, we can clearly see the dependency of NPR on the discharge voltage and current. The normalized NPR increased from 2.5×10^4 n/s/Pa to 3.8×10^4 n/s/Pa by introducing the magnets under a discharge condition of 40 kV, 13 mA.

When introducing the magnets, strong light emission patterns sometimes appeared near the anodes under certain discharge conditions as shown in Fig. 5a. Since this emission pattern was accompanied by lager discharge current, we call this "low-Z (low-impedance) mode". In the low-Z mode the operating voltage largely decreased, so nuclear fusion reactions

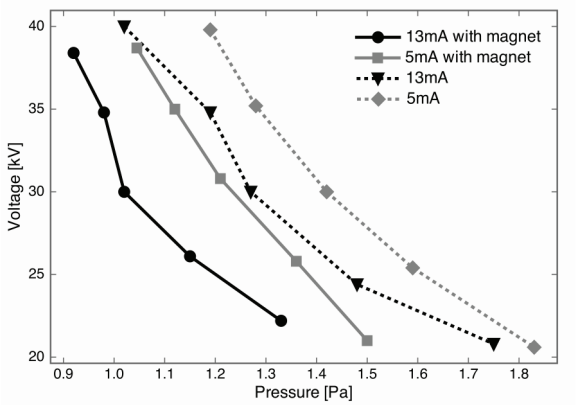

Fig. 3 Dependency of discharge voltage on back ground gas pressure. Solid and dotted lines are results with and without anode magnets, respectively.

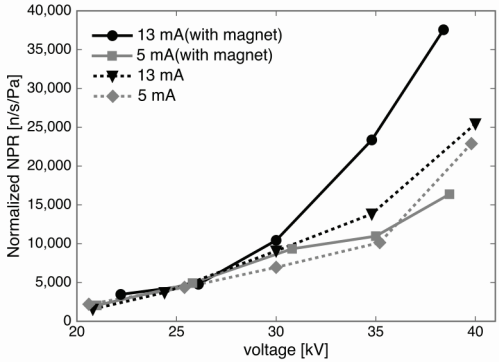

Fig. 4. Dependency of normalized neutron production rate (NPR) on discharge parameters.

were strongly suppressed. Therefore, the low-Z mode must be avoided in operating the IEC device as a neutron source. On the other hand, a discharge mode with relatively high voltage could be achieved by carefully controlling the gas pressure and the discharge current (Fig. 5b). This "high-Z" mode is considered to be suitable for neutron production. The NPR increase observed in Fig. 4 was available only in the high-Z mode.

As shown in Fig. 5a, the shape of light emission pattern is similar the shape of the magnetic field lines. In this region the so-called magnetron discharge process happens; secondary electrons generated by the electron avalanche process near the anode are trapped by the magnetic field, leading to strong ionization of the background gas. As a result, a relatively highly ionized (low-impedance) plasma is generated near the anode.

The original role of the anode magnet is to enhance

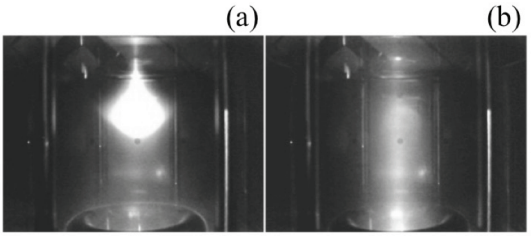

Fig. 5. Typical light emission patterns of the plasma column: (a) low-Z mode (2.6 kV, 1.8 Pa, 20 mA) and (b) high-Z mode (22.6 kV, 1.0 Pa, 20 mA).

the ionization of the background deuterium gas by the magnetron discharge, which is expected to enhance the NPR. However, it was difficult to control the discharge so that two conflicting conditions, high ionization degree and high impedance of plasma, could be satisfied at the same time. One possible way to improve the controllability is to introduce additional electrodes near the anodes that are used for the control of the magnetron discharge condition. The design work based on this idea is underway.

3. Neutron imaging test

Figure 6a shows the IEC neutron source used for the neutron imaging in this study. Figure 6b shows the setup of the imaging experiment. The anode (height 320 mm, ø200 mm) and the cathode (height 380 mm, ø40 mm) are coaxially mounted in a vacuum chamber (height 340 mm, ø393 mm). Both electrodes consist of cylindrically arranged stainless-steel rods. The cathode was biased to negative high voltage (~60 kV) via a feedthrough, and the anode and the chamber were grounded. In this device ions are accelerated and converged in the radial direction, so neutron production occurs in the region along the center axis of the cylindrical cathode. The device was operated typically for 3 hours in the imaging experiment with a NPR of 10^6-10^7 n/s. To thermalize neutrons, polyethylene blocks (200 cm × 100 cm × 50 cm) were located between the device and a converter.

The indirect method was used for neutron imaging. This method consists of the following steps; thermal neutrons passing through the object activate a dysprosium (Dy) foil (~3 h), an imaging plate (IP) is activated by the foil (image transfer), and the image

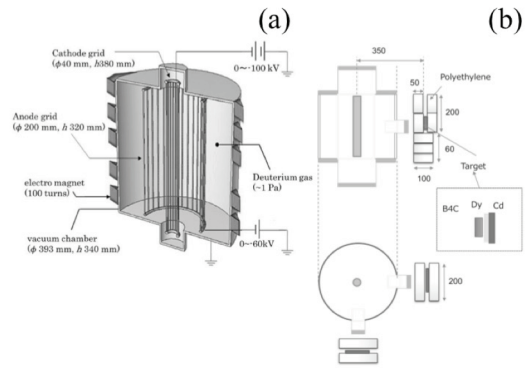

Fig. 6. (a) A schematic of a cylindrical IEC device, (b) imaging setup.

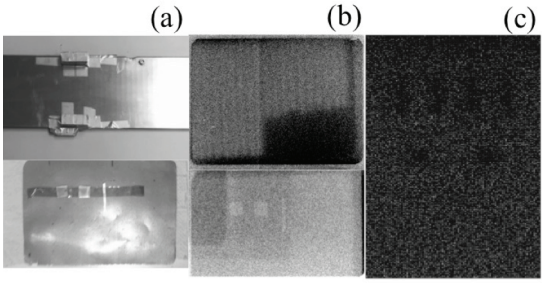

Fig. 7. (a) Imaging objects, (b) neutron images of B_4C powder and Cd pins, (c) numerically obtained neutron images of Cd pins.

was read out from the IP by a scanner. This method is free from background radiation. In the present study, a stainless-steel sample containing B_4C powder and Cd pins were prepared as objects. Geant4[7], a Monte-Carlo code, was used to simulate neutron dose on the imaging plane.

Figure 7 shows the objects, the observed images, and a numerically predicted image. As shown in Fig. 7b, B_4C powder and Cd pins were successfully imaged. In addition, the numerical analysis well reproduced the contrast of the images obtained by the experiment.

4. Conclusion

Introducing magnetic field near the anodes of the linear-type IEC device was found to effective for the enhancement of the NPR. Typically, a normalized NPR was enhanced by ~50 % under a discharge condition of 40 kV and 13 mA. Without the magnet, a normalized NPR was 2.5×10^4 n/s/Pa, and so a normalized NPR was increased.

The neutron imaging using a coaxial-cylinder-type IEC device was carried out, and the imaging of B4C powder contained in a stainless-steel holder and Cd pins was successfully demonstrated.

References

[1] George H. Miley, and John Sved, "The IEC–A Plasma-target-based Neutron Source," *Appl. Radiat. Isot.* Vol. 48, No. 10-12, pp. 1557–1561, 1997

[2] T. Takamatsu, K.Masuda, T. Kyunai, et al., "Inertial electrostatic confinement fusion device with an ion source using a magnetron discharge," *Nucl. Fusion*, Vol. 46, pp. 142-148, 2006

[3] K. Masuda, T, Nakagawa, J. Kipritidits, et al., "Cathode grid current dependence of D(d, n)^{3}He reaction rates in an inertial electrostatic confinement device driven by a ring-shaped magnetron ion source," *Plasma Phys. Control. Fusion*, Vol. 52, pp. 1-15, 2010

[4] J. Khachan, and S. Coils, "Measurements of ion energy distributions by Doppler shift spectroscopy in an inertial-electrostatic confinement device," *Phys. Plasmas,* Vol.8 No. 4, pp. 1299-1304, 2001

[5] J. Khachan, D. Moore, and S. Bosi, "Spatial distribution of ion energies in an inertial electrostatic confinement device," *Phys. Plasmas,* Vol. 10, No. 3, pp. 596-599, 2003

[6] Luis Chacon, Blair P. Bromley, and George H. Miley, "Prospects of the Cylindrical IEC Fusion Device as a Neutron Source," in *proc. 17th IEEE/NPSS Symposium Fusion Engineering*, 1997, pp. 858–861

[7] S. Agostinell, J. Allison, K. Amako, et al. "Nuclear Instruments and Methods in Physics Research Section A: Accelerators, Spectrometers, Detectors and Associated Equipment," *Nuclear Instruments and Methods in Physics Research* A, Vol. 506, pp. 250–303, 2003

Biological Impact of Non-thermal Intense Narrowband Pulsed Electric Fields

Sunao Katsuki, Nobuaki Ohnishi*, Daiki Miyakawa*

Institute of pulsed power science, Kumamoto University, Kumamoto, 860-8555 Japan
**Graduate school of science and technology, Kumamoto University, Kumamoto, 860-8555 Japan*

ABSTRACT

This paper describes the biological effect of intense pulse electric field from the frequency point of view. A pulse-modulated sinusoidal wave as a narrowband pulsed electric field (nbPEF) allows us to deliver a non-thermal, intense and well-defined electric field in terms of frequency, field strength and deposition energy to biological systems. 10 μs long sinusoidal electric fields with a frequency range between 0.1 and 100 MHz and field strengths of up to 10 kV/cm were applied to HeLa or HeLaS3 cells, which were subsequently analyzed in terms of the morphology and the Ca^{2+} response. The field with the frequency below a few MHz immediately causes blebs in the external field direction, whereas the morphology does not change apparently in the case of the frequency more than 10 MHz. The intracellular Ca^{2+} concentration rapidly increased after the exposure to the low frequency field and subsequently decayed exponentially within hundreds of seconds. Inversely, for the high frequency fields, the Ca^{2+} concentration did not change for seconds after the pulse, but increased gradually in tens to hundreds of seconds. When the Ca^{2+} channel on the plasma membrane was inhibited, the delayed Ca^{2+} uptake was suppressed. Our experiment shows that the possibility to activate or impair function of membrane proteins physically by using nbPEF without significant defects of the plasma membrane.

Keywords

Key Words: narrowband pulsed electric field, biological effect, cell morphology, blebbing, Ca^{2+} uptake, pore formation, TRP channel.

1. Introduction

Biological effects of intense pulsed electric fields (PEFs) have been reported over the past three decades. Neumann firstly reported in 1972 permeability changes induced by PEFs in membrane [1]. PEFs with a pulse length of longer than 10 μs are generally used for electroporation because the cell membrane acts as a capacitor and has to be charged to a sufficient voltage to cause membrane defects [2]. Schoenbach et al have started using nanosecond pulsed electric fields (nsPEFs) and reported their effects on various kinds of mammalian cells over the past decade [3]. Application of nsPEFs to biological cells results in intracellular effects with the intense electric field inside the cell seemingly adding a new stress to the internal biological system which will potentially be used for biotechnology and medical treatment.

Fig. 1 shows a schematic illustration of a mammalian cells exposed to an electric field and its simplified equivalent circuit. Plasma membrane, which can be regarded as an insulating dielectric film, separates intracellular components from outer environment. The membrane significantly influences the electrical energy flow under an external electric field. The membrane prevents low frequency energy (<0.3 MHz) from entering the cell, whereas high frequency energy flows into the cell because the electrical impedance of the membrane is inversely proportional to the frequency. Other possible effect is to the membrane proteins such as ion channels, ion

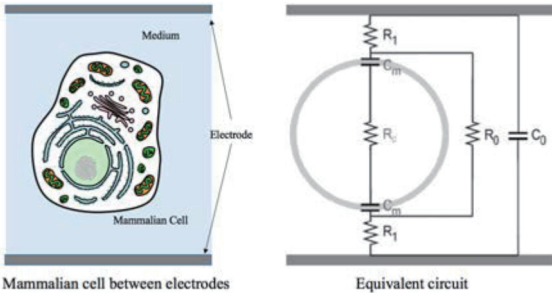

Fig. 1 Schematic illustration of mammalian cells exposed to non-thermal intense electrical pulses.

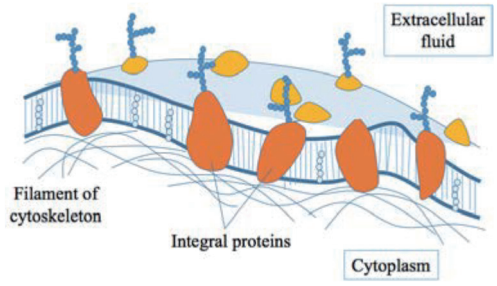

Fig. 2 Schematic illustration of plasma membrane with various kinds of proteins.

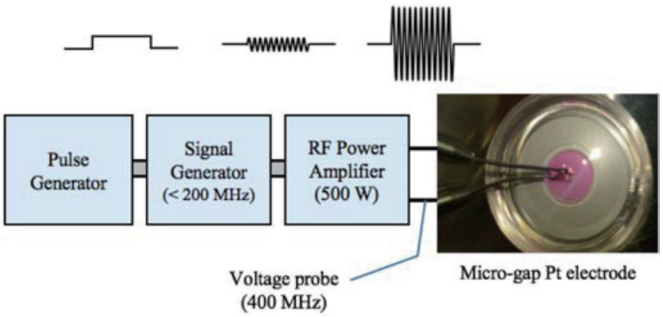

Fig. 3 Block diagram of the nbPEF application system.

pumps, signal receptors. As shown in Fig. 2, they are linked to the plasma membrane in various forms and most of them expose their part to the outer environment. An intense external field affects this external part as a mechanical stress, which might lead to activation of the protein function.

Based on the fact that cells are a complex of dielectric materials, the intracellular effects are expected to depend on frequency, field strength as well as input energy of the applied electric fields. In most of the previous studies, monopolar square pulses or their combinations have been used since the structure of the pulse generators are simple and flexible. Frequency components of a sub-hundred ns long rectangular pulse are widely distributed from zero to hundreds of MHz, which might cause various frequency dependent effects simultaneously. Electric fields with narrowband frequency spectra enable us to discuss more clearly the frequency dependence of the biological effects. We previously proposed the use of intense narrowband pulsed electric field (nbPEF) [4], which allows us to give a well-defined field in terms of frequency, amplitude and exposure time to biological targets.

Previously we demonstrated that intracellular DNA is induced to break by the exposure to nbPEF with frequencies exceeding approximately 3 MHz [5]. Also, we reported that nbPEF with tens MHz range accelerates the proliferation of mammalian cells [6]. Vernier reported firstly that nanoseconds PEF induces the rapid increase of intracellular Ca^{2+} concentration [7]. Ca^{2+}, of which the intracellular concentration is kept extremely low (<0.2 μmol/ml), are well known as the ubiquitous second messenger to initiate various kinds of signal transductions related to apoptosis, necrosis, cell cycling, production of reactive oxygen species, etc. Here, we describe the morphological change and the Ca response of mammalian cells after exposing to nbPEF, which are dependent upon the frequency. This result enables us to discuss more clearly the physical impact of non-thermal, intense pulsed electric fields on mammalian cells from the frequency point of view.

2. Materials and Methods

(1) NbPEF Application System

Our nbPEF application system consists of a signal generator (Agilent, E4400B) to generate a sinusoidal wave of frequency between 0.3 and 100 MHz, a pulse generator (Berkeley Nucleonics, Type555) to determine the pulse duration and a radio frequency amplifier (Empower RF Systems, 2088, 500 W), as shown in Fig. 3. A 10 μs-long sinusoidal voltage pulse with amplitude up to 500 V was delivered to a platinum micro-gap electrode placed on a glass bottom dish through a 50 Ω coaxial cable (RG213/U). A non-inductive resistor was inserted between the coaxial cable end and the electrodes for matching. The voltage between the electrodes was monitored by using a high voltage probe (Iwatsu, SS-0170R) in every shot.

(2) Cell and Culture Condition

All experiments were conducted using HeLa or HeLa S3 cells cultured in an incubator (5% CO_2, 95% air, 37℃) with α minimum essential medium (α MEM) including 10% fetal bovine serum (FBS). The cells were moderately passage through every 2 days, before getting 80% confluent. The cells used in the experiment were therefore assumed to be in logarithmic growth phase. The cultured cells were washed by PBS (phosphate buffered saline pH 7.4), detached by PBS base 2 mM EDTA (etylendiamine tetetraacetic acid), suspend by 10% FBS- α MEM, centrifuged at 1,000 rpm for 5 min at room temperature. Then they were re-suspended to 2×10 cells/ml with α MEM. Finally, they were stored in the CO2 incubator until they were used.

(3) Cell Morphology and PS Externalization

We observed the cells exposed to the pulse using a phase contrast and fluorescent microscope (Leica, DMI6000B). used fluorescent reagent, annexin V-FITC (ABD Bioquest) to investigate the membrane integrity. Phosphatidylserine (PS) is a phospholipids nutrient usually hidden in inner surface of plasma membrane. Usually, in an early phase of apoptosis, the PS moves to outer surface of the membrane. Labeling the PS by annexin V that fluoresces in green enables to visualize cells in the early-to-mid phase of apoptosis. This process is advanced slowly. An intensive physical membrane stress like pulsed electric field causes the mobilization of phospholipids, resulting in the PS connecting with annexin V.

(4) Ca Response

We used Fluo8-AM (ABD Bioquest) as fluorescent reagent for detection of intracellular Ca^{2+}. Fluo8-AM is permeable to cell and has a large affinity to Ca^{2+}. After removing the culture medium from the incubated cell dish, the cells were gently washed with phosphate buffered saline (PBS). 1 mL HBSS including 1 μL Fluo8-AM were added to the dish, which was subsequently incubated for 30 min for Fluo8-AM permeating the cells sufficiently. Afterwards, again the cells were gently washed with PBS and a culture medium was added prior to the exposure to nbPEF. Therefore, the situation is that Fluo8 exists only inside the cells. The exposure to nbPEF was completed within 5 min after the preparation. Also, we conducted two experiments to discuss the source of Ca^{2+}. Firstly, we used Ca-free medium to see Ca^{2+} release from intracellular stores. Secondly, we used the inhibition reagent of Ca^{2+} channels (TRP channels), Ruthenium Red (RR) to explore the route of Ca^{2+} influx through the plasma membrane.

3. Results and Discussion

(1) Morphological Change

Fig. 4 shows the phase contrast and the fluorescent images of HeLa S3 cells 2 min after the exposure to 10 nbPEFs for 0.3 and 30 MHz. All cells exposed to 0.3 MHz nbPEFs have a number of blebs. The fluorescent image shows the fluorescence is localized on the membrane at both polar sites, which is unique feature of the alternating current electric fields. The blebbing

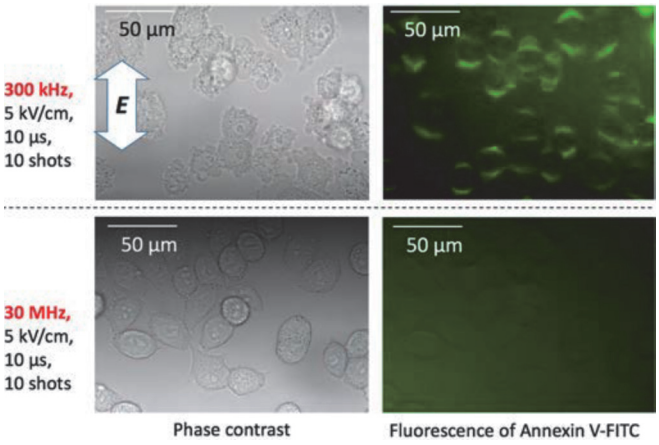

Fig. 4 Phase contrast and fluorescent (Annexin V-FITC) images of HeLa S3 cells 2 min after the exposure to 10, 5 kV/cm, 10 µs-long nbPEFs with different frequencies of 0.3, 30 MHz.

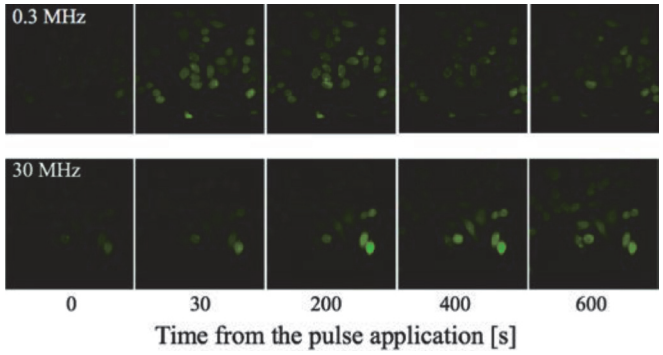

Fig. 5 Temporal variation of the presence of Ca^{2+} after the exposure to 50, 5 kV/cm nbPEF for two different frequencies of 0.3 and 30 MHz. Fluorescent dye Fluo8- AM was used as the Ca^{2+} indicator.

is supposed to occur due to the damage of the plasma membrane because of the enhanced electric field. When a mono-polar pulse was applied, the blebs tend to be formed only at the anode side because of the natural membrane potential (data not shown). In the case of 30 MHz, neither bleb nor fluorescence are observed despite the same external field strength. According to calculation of the electric field distribution under ac field [5], the enhancement of the electric field at the plasma membrane is mitigated at the frequency exceeding 1 MHz since the electrical impedance of the membrane is decreased with increasing the frequency of the applied field. apparent change occurs in 10 MHz. This implies that the cells might receive different stress for different frequency even for higher frequency range above 1 MHz, where the membrane seems to remain intact.

(2) Calcium Response

Fig. 5 shows the typical Ca responses of HeLa cells to two different frequencies of 0.3 and 30 MHz nbPEFs indicated by the fluorescent reagent detecting Ca^{2+}, Fluo8. The intracellular Ca^{2+} concentration rapidly increased after the exposure to 0.3 MHz nbPEFs and afterwards the concentration gradually decayed in hundreds of seconds. Inversely, the Ca^{2+} concentration did not change for seconds after the 30 MHz pulse, but increased gradually in tens to hundreds of seconds. Figure 6 shows the temporal variation of intracellular Ca^{2+} concentration as a function of

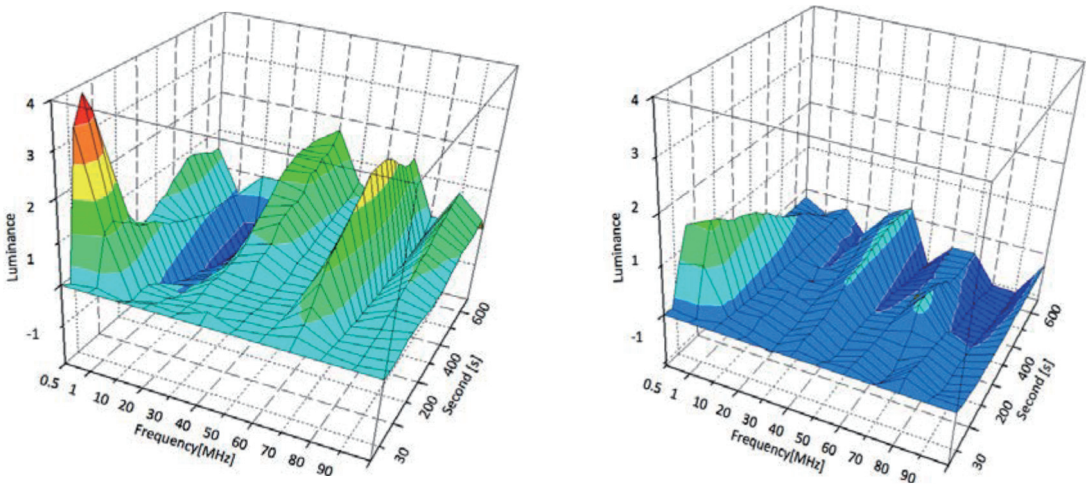

(a) Without Ruthenium Red (b) With Ruthenium Red to inhibit TRP channels

Fig. 6 Temporal variation of intracellular Ca^{2+} concentration aftet the exposure to 50, 5 kV/cm nbPEF, as a function of frequency of the electric field. (a) without (b) with Ruthenium Red for inhibition of TRP channels.

frequency of the applied electric field. When the cells were suspended in Ca-free medium, each cell independently showed a tiny fluctuation of the Ca^{2+} concentration, which lasted for tens of seconds (data not shown). This Ca^{2+} was released from intracellular stores such as an endoplasmic reticulum. Figures 6(a) and 6(b) show results of the experiments without and with RR, respectively. When the TRP channels were inhibited, the rapid Ca^{2+} increase was suppressed at the low frequency, whereas for tens of MHz nbPEF, the delayed Ca^{2+} uptake did not occur. At the situation that the membrane is significantly damaged at the low frequency nbPEF, Ca^{2+} flows mainly through the membrane pores, but also TRP channels contribute to some extent. At the higher frequencies more than a few MHz, the Ca^{2+} influx through the pores does not seem dominant, TRP channels play a certain role for the Ca^{2+} uptake. Interestingly, behavior of the delayed Ca^{2+} uptake seems dependent on the frequency. Membrane proteins might receive different stresses for different frequency. Our experiment shows that the possibility to activate or to impair function of membrane proteins physically by using nbPEF without significant defects of the plasma membrane.

References

[1] E. Neumann and K. Rosenheck, “Permeability Changes Induced by Electrical Impulses in Vesicular Membranes”, J. Membrane Biol. vol. 10, pp. 279-290, 1972

[2] U. Zimmermann, G. Pilwat and F. Riemann “Dielectric Breakdown of Cell Membranes”, Biophys. J., vol. 14, pp. 881-899, 1974.

[3] K.H. Schoenbach, S.J. Beebe and E.S. Buescher, “Intracellular effect of ultrashort electrical pulses”, Bioelectromagnetics, vol. 22, pp. 440-448, 2001.

[4] S. Katsuki, N. Nomura, H. Koga, H. Akiyama, I. Uchida and S. Abe, “Biological Effects of Narrow Band Pulsed Electric Fields,” IEEE Trans. Dielectr. Electr. Insulat., vol. 14, pp. 678-684, June 2007.

[5] N. Nomura, M. Yano, S. Katsuki, H. Akiyama, K. Abe and S. Abe, “Intracellular DNA Damage Induced by Non-thermal, Intense Narrowband Electric Fields,” IEEE Trans. Dielectr. Electr. Insulat., vol. 17, pp. 1288-1294, October 2009.

[6] M. Yano, K. Abe, H. Akiyama and S. Katsuki, “Enhancement of Proliferation Activity of Mammalian Cells by Intense Burst Sinusoidal Electric Fields,” IEEE Trans. Dielectr. Electr. Insulat., vol. 19, pp. 331-337, February 2012.

[7] P.T. Vernier, Y. Sun, L. Marcu, S. Salemi, C.M. Craft and M.A. Gundersen, “Calcium burst induced by nanosecond electric pulses”, Biochemical and Biophysical Research Communications, vol. 310, pp. 286-295, 2003.

Design of HPM exposure system for biological experiments

Soowon Lim, Koki Nobutsuka*, Kentarou Kishimoto* and Sunao Katsuki

Institute of pulsed power science, Kumamoto University, Kumamoto, 860-8555 Japan

**Graduate school of science and technology, Kumamoto University, Kumamoto, 860-8555 Japan*

ABSTRACT

High-power microwave (HPM) is widely used in communications, defense, underground exploration and a host of other applications. Especially, applications to biological and medical area are receiving great interest. High peak, low average power radiation may cause biological reactions that are qualitatively different from known microwave effects and cannot be explained by ordinary heating. Therefore, understanding of the biological effects of HPM irradiation is very important for extending use of HPM. Current knowledge of the biological effects is very limited because of specialty of the HPM sources. In this research, design of HPM exposure system for the biological experiments is proposed. The system consists of an inductive energy discharge generator, a reflex-triode virtual cathode oscillator and a bent waveguide.

Keywords

Key Words: high-power microwave, reflex triode vircator

1. Introduction

Recent advances in pulsed power technologies have resulted in increased availability and wider use of microwave transmitters that can emit nano- and micro- second pulses at peak powers of hundreds of megawatts or even gigawatts. High-power microwave (HPM) is widely used in communications, defense, underground exploration and a host of other applications. Especially, applications to biological and medical area are receiving great interest. One can reasonably expect that high peak, low average power radiation may cause biological reactions that are qualitatively different from known microwave effects and cannot be explained by ordinary heating. These biophysically different reactions will have a possibility of novel application area. Therefore, understanding of the biological effects of HPM irradiation is very important for extending use of HPM. Accumulation of experimental data including HPM conditions and theoretical analyzation of the data are also required [1], [2].

Current knowledge of HPM biological effects is very limited because of specialty of the HPM sources. The few studies that have explored peak SAR (Specific absorption rate) levels of 0.1-60 MW/kg in animals and in vitro, have produced isolated, sometimes contradictory, and generally inconclusive data. The data on HPM bio-effects at higher peak SAR (100 MW/kg and higher) are even more scarce. These studies claimed profound HPM non thermal effects, including changes in the growth rate and metabolism of alga cultures, stimulation of the immune system, suppression of tumor growth in vivo and in vitro, and inhibition of a fungus Fusarium growth, induction of developmental aberrations, imago death, and infertility in Drosophila flies. Pakhomov et al., however, pointed out in his paper that studies mentioned above could have suffered various flaws, both in biological experiment protocols and dosimetry, thus requiring confirmation for the findings [3]–[8].

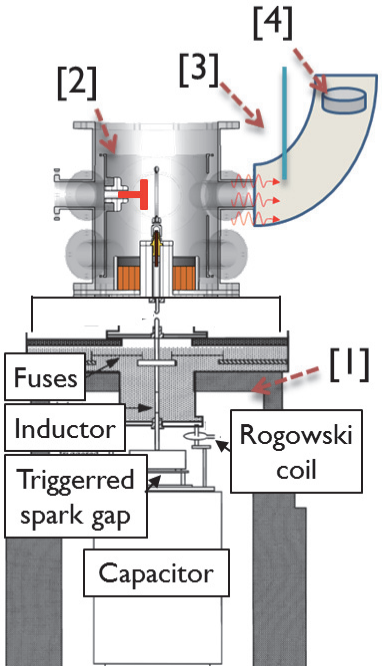

Fig. 1 The high-power microwave exposure system. (1) Inductive energy discharge generator. (2) Reflex-triode virtual cathode oscillator. (3) Bent waveguide and X-ray protector. (4) Target.

2. Experimental Setup

The system consists of an inductive energy discharge generator, a reflex-triode virtual cathode oscillator and a bent waveguide. Figure 1 and figure 2 show the HPM exposure system and an equivalent circuit, respectively. An inductive energy discharge generator was used to generate high-voltage pulse. 22 kV is charged to a capacitor of 14.9 μF. Once we trigger a triggered spark gap switch, the energy stored in the capacitor is transferred to a 1.8 μH inductor. 6 copper wires of 0.15 mm in diameter are used as an opening switch to transfer the accumulated inductive energy to a reflex-triode vircator. The HPM pulse is generated by the vircator. The generated HPM pulsed is guided by a waveguide and irradiated to the target cells. A 90-degree bent waveguide and lead plates are used to block X-rays since the vircator generate the HPM pulse but also the X-rays.

3. Results and Discussion

Figure 3 shows a typical output waveform of the inductive generator. Once the spark gap switch is closed current about 20 kA peak flows in the circuit. However, the current is gradually decreased after 4 μs due to the resistance rising of the fuses. The fuses were disconnected about 4.6 μs and the voltage potential between the both ends of fuses increased rapidly. Then the steepening gap in fig. 2 is closed and the energy is transferred to the vircator. A typical voltage is about 250 kV peak and 200 ns of full with of half maximum.

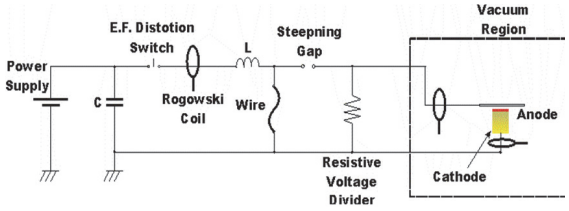

Fig. 2 Equivalent circuit of HPM generator

We measured the microwave waveform at the target position in figure 1 using a free-field magnetic field sensor(B-90B(R), PRODYN Technologies, 8 GHz bandwidth), a balun(BIB-100G, PRODYN Technologies, 10 GHz), an attenuator(40 dB, Weinschel, 8.5 GHz) and an oscilloscope(DP07604C, Tektronix, 16 GHz). Figure 4 shows a typical waveform of the vircator. The main frequency was between 2.7 GHz and 4.6 GHz.

The input voltage and output microwave is adjustable by changing the fuses(number and diameter of the fuses) and vircator(anode mesh and gap distance) parameters. We are going to do

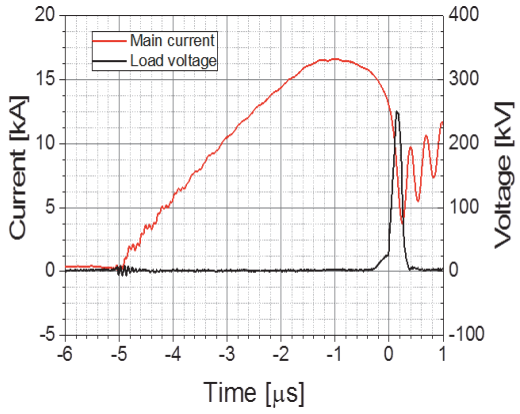

Fig. 3 Typical waveform of the inductive generator

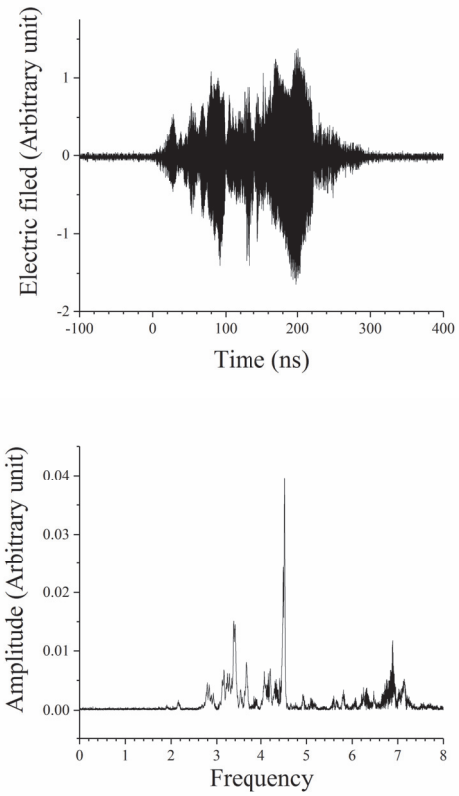

Fig. 4 Typical waveform of the vircator(upper) and frequency distribution(lower)

biological experiments under various conditions of the microwave.

4. Conclusions

In this paper, we proposed a design of HPM exposure system for biological experiments. The system consists of the inductive energy discharge generator, the reflex-triode vircator, the bent waveguide and the X-ray protector. Further improvements of the generator will be performed to do biological experiments under various conditions.

Acknowledgements

This work was supported by Overseas researcher under Postdoctoral Fellowship of Japan Society for the Promotion of Science grant numbers 16F16370.

References

[1] S. H. Gold and G. S. Nusinovich, “Review of high-power microwave source research,” Rev. Sci. Instrum., vol. 68, no. 11, pp. 3945–3974, 1997.

[2] R. L. Seaman, “Review of literature on high power microwave pulse biological effects,” GENERAL DYNAMICS ADVANCED INFORMATION SYSTEMS BROOKS CITY-BASE TX, 2009.

[3] B. L. Ibey et al., “Cellular effects of acute exposure to high peak power microwave systems: Morphology and toxicology,” Bioelectromagnetics, vol. 37, no. 3, pp. 141–151, 2016.

[4] N. Deviatkov, S. Pletnev, Z. Chernov, V. Faĭkin, G. Bernashevskiĭ, and K. Shchitkov, “Effect of a low-energy pulse of EHF and SHF-radiation of nanosecond duration with a high peak intensity on biological structures (malignant neoplasms),” presented at the Doklady Akademii nauk, 1994, vol. 336, pp. 826–828.

[5] N. Deviatkov et al., “Effect of low-energy pulsed EHF and microwave radiation with nanosecond pulse duration and high peak power on biological structures (malignant neoplasms),” Biomed. Radioelectron., vol. 1, pp. 56–62, 1998.

[6] M. Bolshakov et al., “Effect of repetitive HPM pulses on some biological objects,” Radiat. Phys. Chem. Condens. Matter High Curr. Electron. Modif. Mater. Part. Beams Plasma Flows, vol. 2, pp. 514–518, 2000.

[7] A. G. Pakhomov, J. Doyle, B. E. Stuck, and M. R. Murphy, “Effects of high power microwave pulses on synaptic transmission and long term potentiation in hippocampus,” Bioelectromagnetics, vol. 24, no. 3, pp. 174–181, 2003.

[8] O. Betsky, “Millimeter waves in medicine and biology,” Raditechnika Radioelectron. Radiotech. Radioelectron., vol. 38, no. 12, pp. 1760–1782, 1993.

Measurement of Ozone and OH Radical in Air Plasma Including Water Droplets

Taichi Sugai, Akira Tokuchi*, Weihua Jiang

Nagaoka University of Technology

**Pulsed Power Japan Laboratory Ltd.*

ABSTRACT

We have studied water treatment by spraying water droplets into pulsed discharge plasma space. To investigate the effect of ozone and plasma to OH radical production in this method, concentration of OH radical and ozone were measured in two cases of spraying water droplets into ozone space and into plasma space. OH radical concentration increased with ozone concentration, however, OH radical concentration in case of spraying into ozone space was similar to that in case of spraying into plasma space if ozone concentration is similar. That means that few or no OH radicals are generated from dissociation of water by electron collision, and almost all OH radicals are produced from the path including the reactions of hydroxide ion in water with ozone produced by plasma, in case of spraying water droplets into the plasma space.

Keywords

Water Treatment, Plasma, Pulsed Power, OH radical, Ozone

1. Introduction

Recently, water treatment which can decompose refractory organic compounds efficiently, is required because of stricter regulations being imposed on wastewater discharge into the environment. As one of methods for the decomposition of refractory organic compounds, water treatment by plasma in atmospheric pressure has been studied. Interaction between electron in plasma, gas, and water generate various active species that decompose organic compounds in water. Although various plasma reactors have been studied[1], we have adopted a method of spraying waste water into plasma space because large plasma volume and wide reaction area between active species and water can be realized. In this method, OH radical generation is very important because it can decompose refractory compound owing to its high oxidation potential.

The goal of this study is to elucidate processes of OH radical generation to realize effective OH radical generation. Generally, OH radical is produced by dissociation of water by electron collision. However, it is expected from recent research that OH radical generation process via reactions with ozone is dominant. The purpose of this study is confirmation of the effect of ozone and plasma to OH radical generation. To confirm it, OH radical concentration in cases of spraying into plasma space and into ozone space was measured and compared, and the relations between ozone concentration and OH radical concentration were investigated.

2. Experimental Setup

The water treatment system used in this experiment is shown in Fig. 1. The system is composed of a reactor module and a water tank module. In the reactor module, wire-to-cylinder coaxial electrodes are installed in the reactor cylinder, with an inner diameter of 40 mm. The wire electrode is made of stainless steel wire (diameter = 0.28 mm), and the cylindrical electrode is made of stainless steel

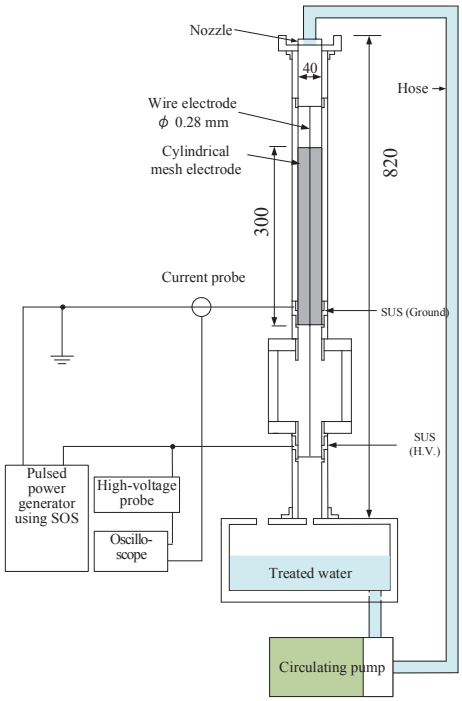

Fig. 1 Outline of setup for plasma water treatment

wire mesh (diameter = 38 mm, length = 300 mm, and mesh size = 1.2 mm × 1.2 mm). The water tank is provided with a pump for circulation of treated water. The treated water is transformed to droplets by a nozzle and sprayed into the reactor from the top of the lid. Flow rate of the circulated water was 4 L/Minute.

Positive pulsed voltage is applied to the wire electrode in the reactor and the cylindrical electrode is grounded to generate the pulsed streamer discharge. The pulsed voltage is applied by a pulsed power generator which is inductive energy storage circuit with a semiconductor opening switch.

3. Measurement Method

3.1 Ozone measurement

As a method of measurement of ozone concentration, indigo method is adopted. This is a method for measuring ozone from absorbance of indigo trisulfonate solution, which is decreased by ozone. The used indigo reagent consists of 15.4 or 30.8 mg/L of potassium indigo trisulfonate, 1.33 g/L of phosphoric acid, and 1 g/L of sodium dihydrogen phosphate. Concentration of ozone was calculated from the difference between absorbance of the treated solution and of the untreated one, by using the following equation [2],

$$\text{Ozone concentration} = \Delta A/20000 \text{ (mol/L)} \quad (1)$$

where ΔA=Difference in absorbance between treated and untreated indigo solutions.

3.2 OH radical measurement

In order to measure the OH radicals, a fluorescence method was adopted. The probe selected for the fluorescence experiment is the disodium salt of terephthalic acid (NaTA). If NaTA reacts with OH radicals, and 35% of the reacted NaTA is converted to 2-hydroxyterephthalic acid (HTA), which gives a bright stable fluorescence. When the solution containing NaTA and HTA molecules is irradiated by UV light (λ=310nm), HTA molecules emit light at λ=425nm, while NaTA molecules do not. In this measurement, NaTA solution of 2 mM was used. For fluorescence emission from HTA, a LED (LLS 310, λ=310nm, Sabdhouse Design) was used. The fluorescence spectrum was recorded through an optical fiber by a spectrometer (FLAME-S, Ocean Optics). In order to quantify the HTA concentration in water, a calibration curve for known HTA concentration was used. Because of 35% conversion to HTA, OH radical concentration is obtained by dividing HTA concentration by 0.35.

4. Experimental Method

Two types of experiment were carried out. One is spraying solutions into ozone space, the other is spraying into discharge space. Ozone space was generated in the coaxial electrode shown in Fig.1, by air discharge for several minutes. After the discharge was stopped, 1.5 L indigo reagent solution or 1.5 L NaTA solution was circulated through the generated ozone space to measure ozone concentration and OH radical concentration, respectively. The circulation was continued until the reaction of the reagent with ozone and OH radical is stopped. After that, ozone or OH radical was measured from the reacted solution. As parameter, discharge time was varied to vary ozone concentration.

At the other experiment, the solutions were

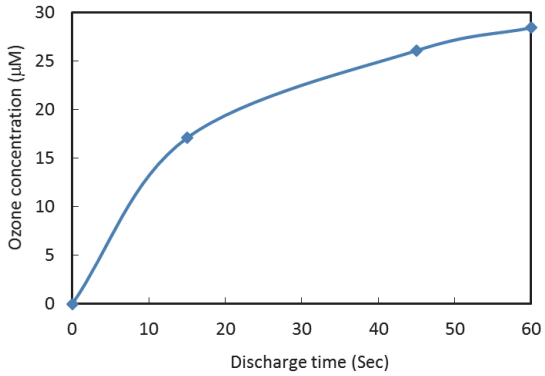

(a) Ozone concentration

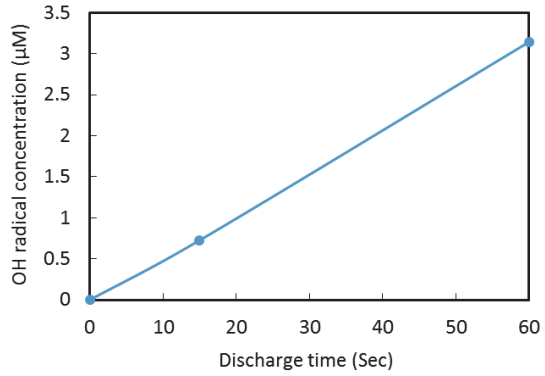

(b) OH radical concentration

Fig. 2 Variation of ozone and OH radical with discharge time in case of spraying water droplets into ozone space.

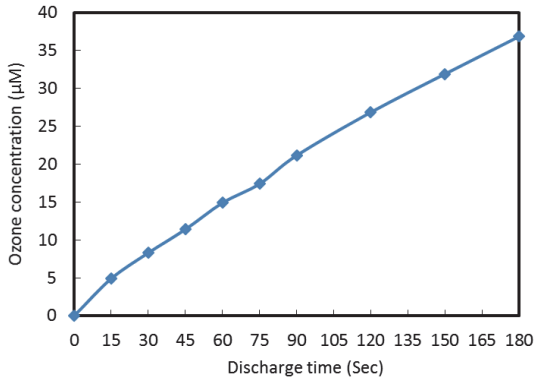

(a) Ozone concentration

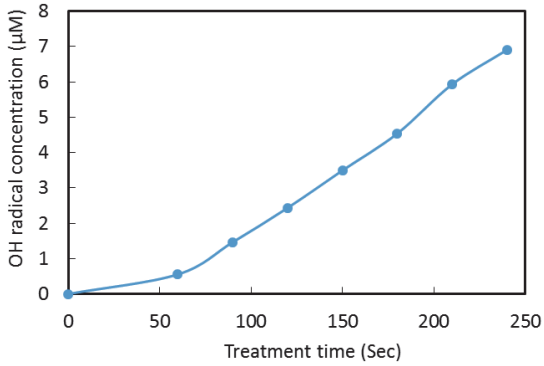

(b) OH radical concentration

Fig. 3 Variation of ozone and OH radical with discharge time in case of spraying water droplets into discharge plasma space.

circulated through the discharge space. A small quantity of solution was taken every stated discharge time, and ozone or OH radical of each discharge time was measured.

5. Experimental Result

Fig. 2 and Fig.3 show variation of concentration of ozone and OH radical with discharge time, in cases of spraying into ozone space and into plasma space, respectively. In Fig. 2, discharge time means time of discharge for ozone generation caused before water is sprayed. On the other hand, the discharge time in Fig. 3 means time of discharge in air including water droplets. Ozone and OH radical increased with the discharge time.

From Fig. 2 and Fig.3, the relation between ozone and OH radical is obtained as shown in Fig. 4, where the concentration of ozone and OH radical measured in same condition is drawn as one plot, and the result

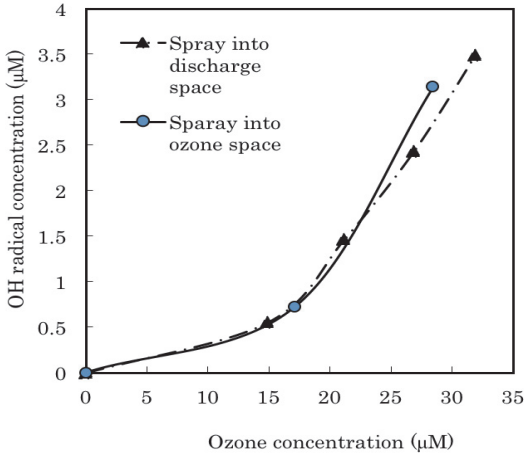

Fig. 4 Relation between ozone and OH radical concentration in cases of spraying water droplets into discharge space and into ozone space.

of the spray into ozone space and the result of the spray into discharge space are distinguished by plot shape. From Fig.4, OH radical concentration increased with ozone concentration, and the OH

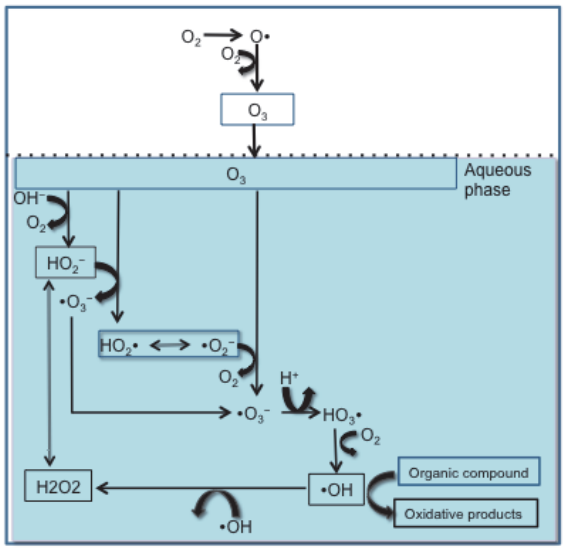

Fig. 5 Expected path for OH radical production, including the reaction of hydroxide ion with ozone.

radical concentration in case of spraying into ozone space was similar to that in case of spraying into plasma space when ozone concentration in the two cases was similar. This means that OH radical concentration depends on ozone concentration regardless presence of plasma radiated to water droplets.

6. Discussion

When water droplets were sprayed into ozone space without plasma, OH radical was produced. In this case, OH radical production path via the reaction of ozone with hydroxide ion, shown in figure 5 is expected. Additionally, because OH radical concentration depended on ozone only and was not related to presence of plasma, few or no OH radicals are generated from dissociation of water by electron collision. Therefore it is expected that almost all OH radicals are produced from the path including the reactions of hydroxide ion in water with ozone produced by plasma, in case of spraying water droplets into the plasma space.

7. Conclusion

To investigate the effect of ozone and plasma to OH radical production, concentration of OH radical and ozone were measured in two cases of spraying into ozone space and into plasma space. Measurement result showed that OH radical concentration in case of spraying into ozone space is similar to that in case of spraying into plasma space if ozone concentration is similar. Therefore, when water droplets are sprayed into the discharge plasma, few or no OH radicals are generated from dissociation of water by electron collision, however almost all OH radicals are produced from the path including the reactions of hydroxide ion in water with ozone produced by plasma.

References

[1] B. R. Locke, M. Sato, P. Sunka, M. R. Hoffmann, and J. S. Chang, “Electrohydraulic discharge and nonthermal plasma for water treatment”, *Ind. Eng. Chem.*, **45**, 3, pp.882–905 (2006)

[2] H. Bader, J. Hoigné, “Determination of ozone in water by the indigo method”, *Water Research*, **15**, pp.449–456 (1981)

Formation of Hot Spots in the Divergent Gas-Puff Z Pinch and Its Application to the Observation of Living Tissue

Keiichi Takasugi, Shun Hakamatsuka, and Veronica Shlyaptseva*

Institute of Quantum Science, Nihon University

**University of Nevada, Reno*

ABSTRACT

The properties of hot spots were investigated in the divergent gas-puff z pinch. The resonance and intercombination lines of He-like Ar ions and the satellite lines were observed by spectroscopic measurements. From the measurement using soft x-ray CCD, the size of the hot spot was found to be about 100 μm. Observations of a ginkgo leaf, a sliced onion, a tiny moth and a mosquito were performed using soft x-ray emitted from hot spots.

Keywords

Divergent gas-puff z pinch, Hot spot, He-like Ar ion, CCD camera, Living tissue

1. Introduction

The gas-puff z pinch is known as a repetitive and efficient system of x-ray radiation[1]. And the plasma focus also allows plasma to converge to a single point reproducibly. The divergent gas-puff z-pinch has been devised for the realization of efficient radiation source which combines both advantages.

In the experiment of divergent gas-puff z pinch, high energy electrons have been observed [2]. Also, high energy ions have been observed, and ion acceleration independent of current direction has been confirmed[3]. It has been confirmed that the generation of high-energy electrons strongly depends on the direction of currents[4].

In this study, spectroscopic measurements and shape measurements of hot spots were performed in the discharge with reversed polarity where electron beams were hard to be generated near the center electrode in the divergent gas-puff z pinch. K-shell radiation of Ar ion emitted from hot spots was applied to the observation of living tissue.

2. Discharge System

The experiment was carried out on the SHOT-GUN III z-pinch device at Nihon University (Fig. 1). The energy storage section of the device consists of 40 kV 12 μF capacitor bank, and the maximum discharge current is 300 kA. The feature of this device is that it can be charged both positive and negative. In this experiment, in order to reduce the generation of electron beam near the center electrode, discharge was performed at the charging voltage of -20 $\sim$ -25 kV.

The gas-puff is made by a high-speed gas valve with a divergent annular Laval nozzle installed in the center electrode. The divergence angle of the nozzle is 10 degrees with respect to the central axis. The diameter of the nozzle is 30 mm, and the opposite electrode has a hole of 60 mm. The distance between the electrodes is 30 mm. Argon was used for the operating gas, and the plenum pressure of the

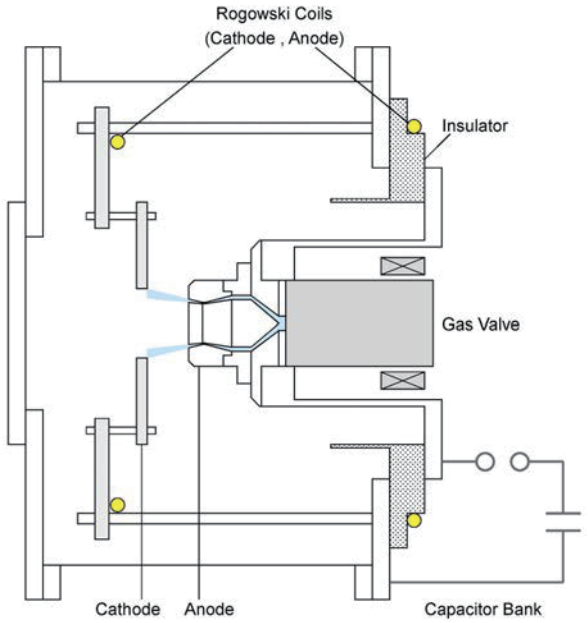

Fig. 1: Schematic diagram of the SHOTGUN III divergent gas-puff z-pinch device. The gas is puffed from the cylindrical Laval nozzle mounted on the center electrode.

valve was 5 atm.

Discharge currents were measured by Rogowski coils placed on the input and the load sides. A scintillation probe using 3 mm thick plastic scintillator was used to monitor x-ray. Figure 2 is the current waveform and the x-ray signal at the charging voltage of -23 kV. The current flows in the reversed direction, and the peak current was about -180 kA. A strong shrinkage of the plasma occur near the peak current, and a dent was formed in the current. The x-ray signal was hardly observed.

3. Soft X-ray Spectroscopy

X-ray spectroscopy was carried out using a Johansson-type curved crystal spectrometer with quartz crystal[5]. Kodak Biomax MS film was used for recording x-ray.

Figure 3 is the result of spectroscopic measurements. The resonant (Ar1) and the intercombination (Ar1′) lines of He-like argon ion were strongly radiated. Satellite lines associated with them have also been observed. Since lines of different ionization states were observed simultaneously, the existence of electron beam

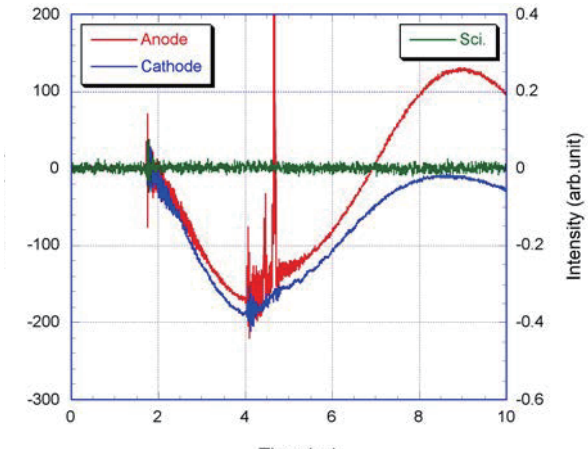

Fig. 2: Discharge currents and x-ray signal of divergent gas-puff z-pinch with negative polarity. X-ray signal was not observed.

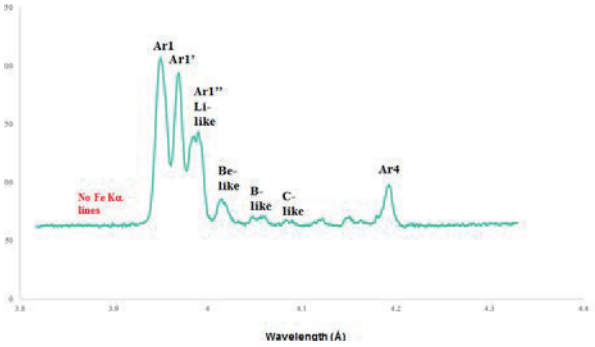

Fig. 3: Soft x-ray spectra of argon gas-puff z pinch. Resonant and intercombination lines of He-like ions as well as satellite lines were observed. Fe K_α lines were not observed.

was conceivable. The K_α lines of iron has been observed in the discharge with normal polarity[6, 7], but they were not observed in the reversed discharge.

4. CCD Measurement

Hot spots were observed using a pinhole camera equipped with a CCD. A CCD manufactured by Laser-Laboratorium Göttingen eV was used. The sensitive region is < 1 nm $\sim$ 1,100 nm, and the pixel size is 6.45 μm $(1,392 \times 1,040$ pixels).

Figure 4 represents the arrangement of pinhole cameras. The ratio of distances between the pinhole and the plasma and the CCD was 4:1. A pinhole with a diameter of 50 μm and a

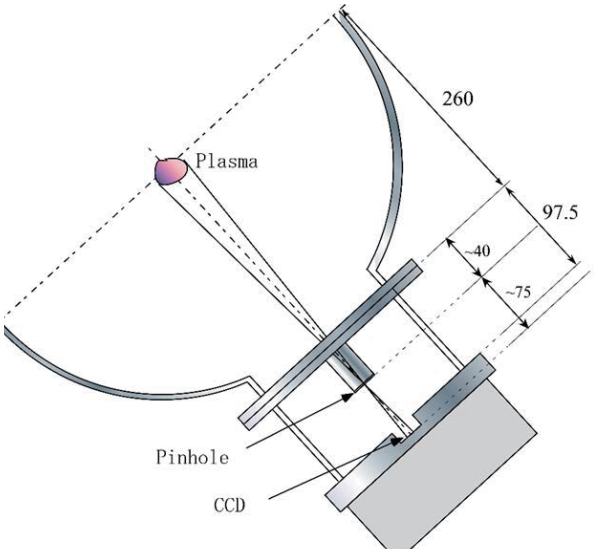

Fig. 4: Soft x-ray pinhole camera with Be window. The image was detected by a CCD camera.

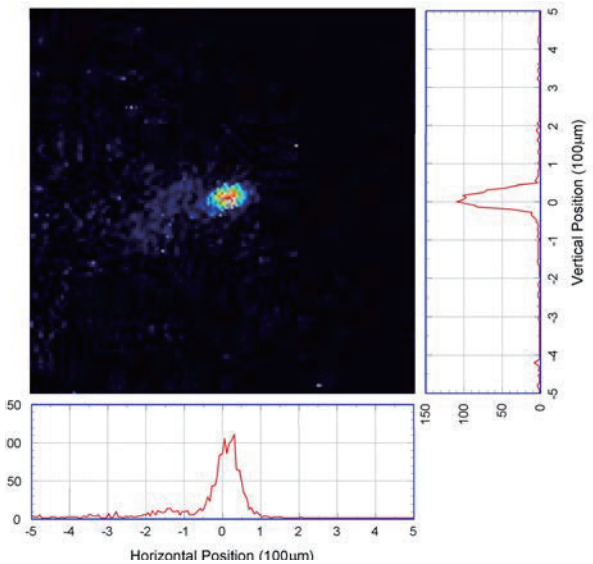

Fig. 5: Soft x-ray image of a hot spot on the CCD. The spot has an elliptic shape, and its vertical diameter is about 90 μm.

Be filter with a thickness of 15 μm were used. Soft x-ray below 1 keV is blocked by the filter.

Figure 5 is the image of a hot spot projected on the CCD. The image can be recorded every discharge, which was observed during the same discharge of Fig. 2. The image was observed while there was no x-ray signal, and it is thought to have captured K-shell radiation of He-like argon ions. The image had an elliptic shape extending in the horizontal (axial) direction, and the vertical diameter was about 90 μm on the CCD. The pinhole diameter is not sufficiently small and the size of the hot spot is not simply 4 times this size. As a result of analysis, it is estimated that the diameter of the hot spot in the vertical (radial) direction is about 100 μm.

5. Observation of Living Tissue

Small organisms were observed using K-shell radiation of argon ions around 3.95 Åemitted from hot spots. The organisms were placed in the vacuum chamber and exposed in close contact with the CCD.

Figure 6 is a radiogarph of a ginkgo leaf. The leaf veins were observed in a streaky fashion. There is a tissue with strong absorption of soft x-ray along the vein. It seems that not only the difference in the thickness of the tissue but also the difference in the organization is observed.

Figure 7 is a radiogarph of sliced onion. Although cell walls were clearly observed with visible light, they were not observed in soft x-ray at all. Instead, a fine structure is seen near the epidermis.

Figure 8 is a radiogarph of a tiny moth (Cephitinea colonella). Feathers are almost transparent. Antennas and leg contours are clearly captured. The structures of the head and abdomen were observed, which cannot be observed with visible light.

Figure 9 is a radiogarph of a mosquito (Aedes japonicus). Feathers can not be seen at all. The contours of the legs and mouth were clearly captured. The structures of the head and abdomen were observed.

6. Summary and Discussion

The divergent gas-puff z pinch discharge with reversed polarity was performed and soft x-ray radiated from hot spots was measured.

The resonant and intercombination lines of He-like argon ion were strongly radiated, and satellite lines have also been observed. Since ions of various ionization states were simultaneously observed, it is conceivable that electron

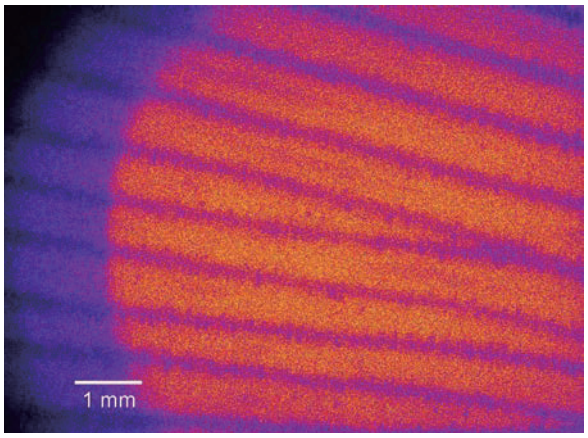

Fig. 6: Soft x-ray radiograph of a ginko leaf.

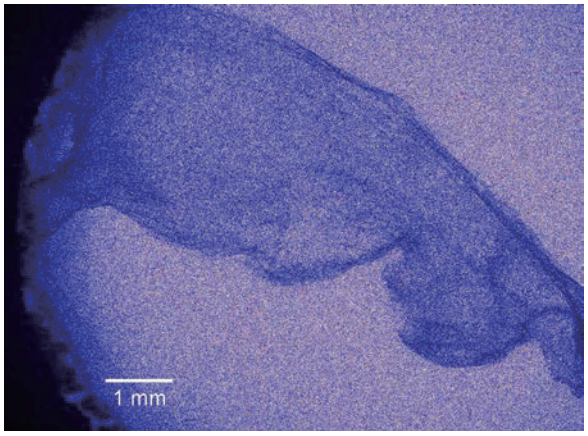

Fig. 7: Soft x-ray radiograph of a sliced onion.

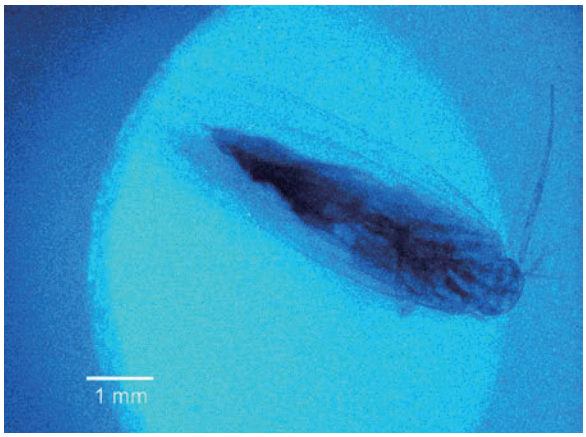

Fig. 8: Soft x-ray radiograph of a tiny moth.

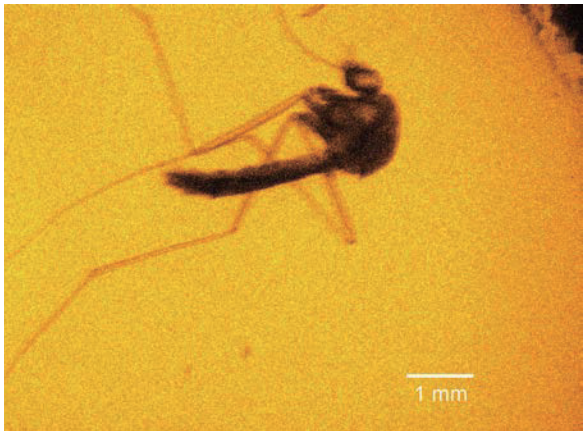

Fig. 9: Soft x-ray radiograph of a mosquito.

beam exists. The K_α lines of iron were not observed in the reversed discharge, which have been observed in the normal discharge.

The hot spot image of K-shell radiation was observed by the CCD camera. The image had an elliptical shape extending in the horizontal direction. The diameter was estimated about 100 μm.

Small organisms were observed using K-shell radiation of argon ions emitted from hot spots. The organisms were placed in the vacuum chamber and exposed in close contact with the CCD.

References

[1] J. Shiloh, A. Fisher and N. Rostoker: Phys. Rev. Lett. **40**, 515 (1978).

[2] K. Takasugi and E. Kiuchi: Plasma Fusion Res. **2**, 036 (2007).

[3] M. Nishio, H. Sakuma and K. Takasugi: Plasma Fusion Res. **6**, 1201009 (2011).

[4] M. Nishio and K. Takasugi: IEEE Tras. Plasma Sci. **43**, 2492 (2015).

[5] E.O. Baronova, M.M. Stepanenko, N. Pereira, A. Muravich, K. Takasugi and T. Miyamoto: NIFS-PROC **45**, 78 (2000).

[6] E.O. Baronova, K. Takasugi, V.V. Vikhrev and T. Miyamoto: Proc. 13th Int. Conf. Particle Beams, 784 (2001).

[7] K. Takasugi and H. Akiyama: Jpn. J. Appl. Phys **43**, 6376 (2004).

Efficiency Enhancement and Characteristic Evaluation of Virtual Cathode Oscillator

Yasunori Eguchi, Taichi Sugai, Weihua Jiang

Extreme Energy-Density Research Institute, Nagaoka University of Technology

ABSTRACT

Recent years, one of them a method of using single pulsed X-ray generated by an accelerator in order to smuggling of nuclear material prevented has expected. However, this X-ray have high intensity and wide range of energy in a short time, so that one difficult to measured using a simple item. As a solution, we proposed using a method combining numerical calculation and shielding experiment. We measured energy spectrum under two conditions of accelerating voltage 380kV and 400kV using proposed method. As result, X-ray intensity is larger at 380kV than 400kV on lower energy side and it is larger at 400kV than 380kV on high energy side. In the future, it will be necessary to compare this result with the simulation value.

Keywords

bremmstrahlung, pulsed X-ray, scintillator

1 Introduction

1.1 Microwave and application

Bremsstrahlung X-rays is that the X-ray generated by the interaction of charged particles and atomic nuclei. The principle of generating is shown in Fig.1.

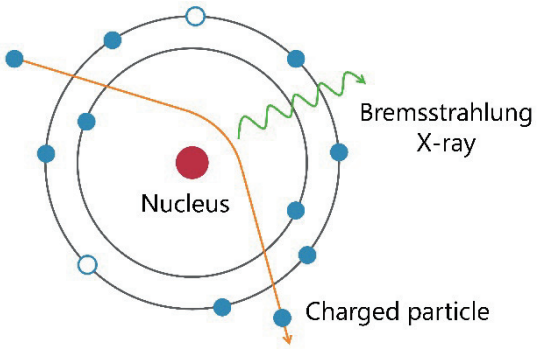

Fig.1 Generating of bremsstrahlung X-ray

The bremsstrahlung X-ray is generated by bending the trajectory or decelerating the velocity for the Coulomb interactions when the charged particles pass near the atomic nucleus. Bremsstrahlung X-rays are continuous spectra, so they have energy distribution over a wide range. Moreover, it does not exceed the maximum energy of incident electrons.

1.2 Pulsed bremsstrahlung X-ray generated from the accelerator

Since the accelerator can generate a high energy electron beam, it is able to generate high energy bremsstrahlung X-rays. This high energy X-ray is used in places such as CT imaging and non-destructive inspection of containers.

On the other hand, after the simultaneous multiple terrorism, there is an attempt to induce photonuclear reaction using this high energy X-ray and positively detect it[1][2]. To realize that attempt, we must know the nature of this X-ray. In this study, we aimed to find out energy spectrum, which is one of their properties. Since the bremsstrahlung X-ray generated from the accelerator has a high intensity in a short time (ns-us), it is difficult to measure using a simple equipment. As a solution, we proposed using a method combining numerical calculation and shielding experiment. In this method, energy

distribution can be determined easily by performing shielding experiment only. In this study, the energy spectrum of bremsstrahlung X - ray generated from the accelerator was measured using the proposed method.

2 Principle and Experimental Setup

2.1 Principle of X-ray spectrum calculation

The equation used for numerical processing of spectrum calculation is shown in Fig.2.

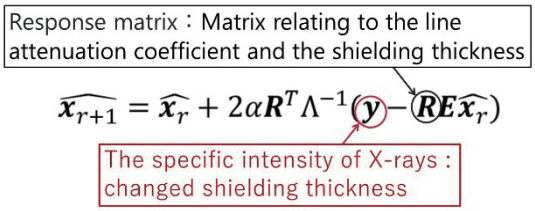

Fig. 2 Spectrum calculation formula

Now, the matrix y is a value obtain by X-ray shielding experiment. Also, the matrix R is a one relating to the line attenuation coefficient and the shielding thickness. The method of shielding experiment will be described later section. By repeatedly calculating this formula, it can diagnostic the X-ray spectrum.

2.2 Experimental Setup

We used the accelerator "ETIGO-IV" in our laboratory. This accelerator can accelerate electrons with a maximum voltage of 400 kV[3].

As an X-ray measuring device, we used that combining a photomultiplier tube (PMT) and a scintillator. The scintillator used LSO and there are advantage of high density and short life span. A schematic diagram of the experimental setup is shown in the Fig.3.

Shown in the schematic diagram Fig. 3, the electron beam generated by the accelerator strikes the copper of the target to generate bremsstrahlung X-rays, and the scintillator emits light when the X-rays are incident. X-rays are measured by making that light incident on the PMT.

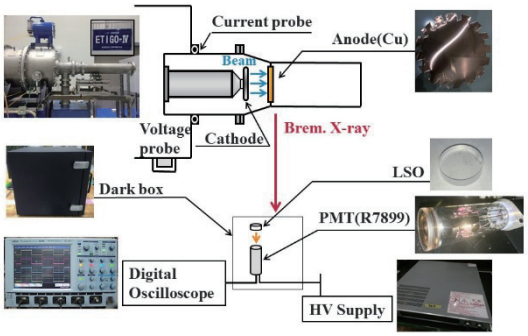

Fig. 3 Layout schematic of experimental equipment

2.2 Experimental Method

1) Shielding Experiment

A copper plate is placed between the accelerator and the measuring instrument to shield X-ray, and this one is measured. The thickness of the copper plate used for shielding change by each 2 mm from 0 to 16 mm. The specific intensity of X-ray (intensity upon shielding /intensity without shielding) is calculated for each thickness.

2) Diagnostic X-ray spectrum by numerical processing

In order to calculate the X-ray spectrum, numerical processing is performed using the equation shown in Fig. 2.

Experimental conditions in this paper are shown in Tab. 1.

Tab. 1 Experiment conditions

AK Gap	22mm
Measurement Distance	2.50m
PMT-LSO	5cm
PMT Voltage	500V
Cu Tickness	0-16mm

3 Result and Discussion

In this paper, we calculated two X-ray

energy spectrum of accelerating voltage 380 kV and 400 kV by the proposed method. In the beginning, measured PMT signal waveforms is shown in Fig. 4.

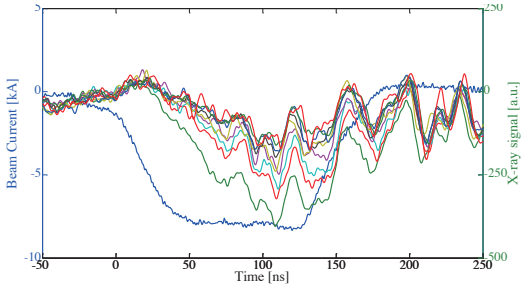

(a)Accelerating Voltage 380kV

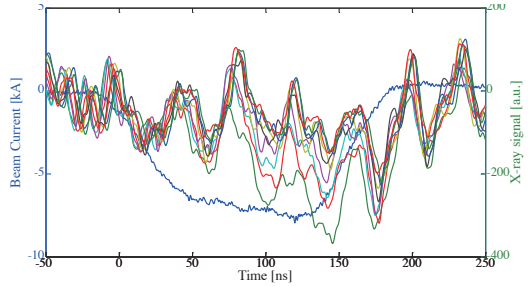

(b)Accelerating Voltage 400kV

Fig. 4 X-ray Signal Waveforms

The matrix y is obtained using the results shown in Fig. 4, and the X-ray energy spectrum calculated by numerical calculation is shown in Fig. 5.

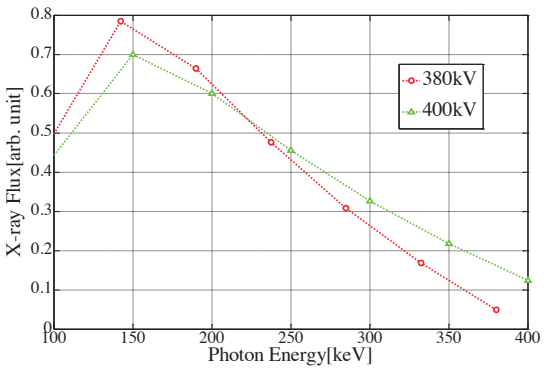

Fig. 5 X-ray energy spectrum

Analysis of the trend of the calculated energy spectrum shows that X-ray intensity is larger at 380kV than 400kV on lower energy side and it is larger at 400kV than 380kV on high energy side. The trend of this result of bremsstrahlung X-ray is expected to be a reasonable result. However, you will need to do a simulation comparison.

4 Conclusion

Bremsstrahlung X-ray was generated using the accelerator ”ETIGO-IV", and it was diagnosed by two instruments with a combination of a scintillator and PMT under accelerating voltages of 380 kV and 400 kV. The specific intensity was determined from the result, and each X-ray spectrum was calculated using it. As result, X-ray intensity is larger at 380kV than 400kV on lower energy side and it is larger at 400kV than 380kV on high energy side. In the future, it will be necessary to compare this result with the simulation value. We also plan to conduct experiments using equipment that can accelerate with much higher energy.

Reference

[1] T. J. Renk et al., "Use of pulsed bremsstrahlung excitation on hermes-iii for investigation of active detection of fissionable material," 2012 Abstracts IEEE International Conference on Plasma Science, Edinburgh, pp. 6D-1-6D-1, (2012)

[2] S. B. Swanekamp, J. P. Apruzese, R. J. Commisso, D. Mosher and J. W. Schumer, "An Analysis of Intense Pulsed Active Detection (IPAD) for the Detection of Special Nuclear Materials," in IEEE Transactions on Nuclear Science, vol. 58, no. 4, pp. 2047-2054, (2011).

[3] A. Tokuchi, N. Ninomiya, Weihua Jiang and K. Yatsui, "Repetitive pulsed-power generator "ETIGO-IV"," in IEEE Transactions on Plasma Science, vol. 30, no. 5, pp. 1637-1641, (2002).

Study on 2-Stage Acceleration of Pulsed Heavy Ion Beam using Bipolar Pulse Voltage

Tarou Honoki, Hiroaki Ito

Department of Electrical and Electronic Engineering,
University of Toyama, 3190 Gofuku, Toyama 930-8555, Japan

ABSTRACT

We have developed a new type of a pulsed ion beam accelerator named "bipolar pulse accelerator" in order to improve the purity of the intense pulsed ion beam. The BPA is operated with the bipolar pulse voltage and is a two-stage electrostatic accelerator. A coaxial gas puff plasma gun was used as an ion source, which was installed inside the grounded anode. When the bipolar pulse with voltage of about −160 kV and +120 kV and pulse duration of about 70 ns (FWHM) each was applied to the drift tube, the pulsed ion beam was observed by two BIC's (biased ion collector) placed downstream of the 2nd gap. By evaluating the ion energy of the ion beam from the time of flight delay time between two BIC signals, it was confirmed that the ion beam is again accelerated toward the grounded cathode in the 2nd gap by the positive pulse of the bipolar pulse and that the impurity of proton is removed.

Keywords

Intense Pulsed Heavy Ion Beam, Bipolar Pulse Accelerator; Magnetically Insulated Ion Diode, Plasma Gun

1. Introduction

Intensity pulsed heavy ion beam (PHIB) technology has been developed over the last two decades primarily for nuclear fusion and high energy density physics research [1,2]. Compared with the traditional ion implantation method, PHIB enables the accumulation of energy in very short time into the near surface region while it maintains a low substrate temperature. Recently, PHIB with an ion energy of several 100 keV, a high ion current density of several 100 A/cm^2, and a short pulse duration of < 1 μs has been widely used as a tool for material processes including the surface modification [3], thin film deposition [4] and ion implantation [5]. Especially, PHIB has received extensive attention as a new ion implantation technology named "pulsed ion beam implantation" for next generation semiconductor materials including silicon carbide (SiC) and diamond, since the ion implantation and the surface annealing can be completed in the same time.

A number of PHIB sources have been developed so far for the requirements of research and industrial application [6,7]. The producible ion species, however, is limited to the material of electrode (anode), since the anode plasma is produced by a high-voltage flashover and an electron bombardment to the anode surface. In addition, the purity of the PHIB is usually deteriorated by absorbed matter on the anode surface and residual gas molecules in the diode chamber [8]. Therefore, the conventional PHIB is not suitable for various applications to material processes.

It is very important for the application of PHIBs to the semiconductor implantation to develop the PHIB technology to generate high-purity ion beams with useful ion species for donor and acceptor in SiC such as nitrogen, phosphorous, boron and aluminum. We have been successful in generating the high-purity pulsed nitrogen and aluminum ion beam with purity of more than 90 % [9,10]. In order to improve the purity of the intense pulsed ion beam, we have developed a prototype of a new accelerator named "bipolar pulse accelerator (BPA)" [11, 12]. When the bipolar pulse

with the first (-114 kV, 70 ns) and the second pulse (85 kV, 62 ns) was applied to the drift tube, the pulsed ion beam with current density of 60 A/cm^2 and pulse duration of ≈50 ns was observed at 48 mm downstream from the anode surface and consisted of N^+ and N^{2+} components with energy of 120~130 keV/Z [13]. It was confirmed that the ions were successfully accelerated in the 1st gap toward the drift tube by the 1st (negative) pulse of the bipolar pulse. As the next stage of the BPA experiment, we have performed experiments on the acceleration of the pulsed ion beam in the 2nd gap. This paper reports the experimental results about characteristics of the pulsed ion beam accelerated by the bipolar pulse.

2. Principle of bipolar pulse accelerator

Figure 1 shows the conceptual diagram of the bipolar pulse accelerator. The BPA is operated with the bipolar pulse voltage and is a two-stage electrostatic accelerator. When a bipolar pulse with voltage $\pm V_{OUT}$ and pulse duration τ each is applied to the drift tube, at first, ions produced in the grounded ion source are accelerated in the 1st gap toward the drift tube by the negative voltage pulse with pulse duration τ. Subsequently, the polarity of the pulse is reversed and the positive voltage pulse of duration τ is applied to the drift tube. As a result, the ions are again accelerated in the 2nd gap toward the grounded cathode and the ion beam experiences total acceleration potential of $2V_{OUT}$ in the accelerator. The condition for the most effective acceleration is that the pulse duration τ is adjusted to the time of flight delay of the ion to pass

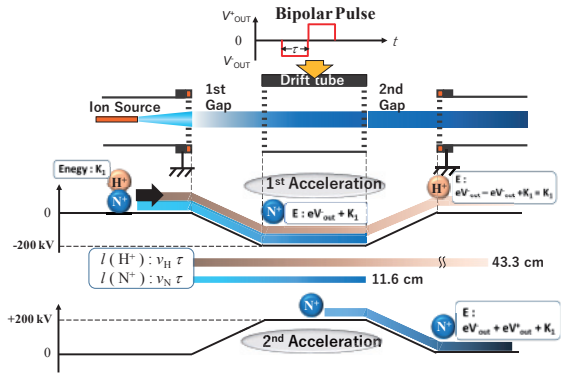

Fig. 1 Schematic of Bipolar Pulse Accelerator.

through the drift tube, i.e., $\tau = L/v_i$, where v_i is the ion velocity in the drift tube and L is the length of the drift tube. This condition can be satisfied by adjusting the parameter of the bipolar pulse and the length of the drift tube. In the above condition, when the top of the ion beam reaches the 2nd gap, the pulse is reversed and the ion beam is accelerated effectively in two gaps.

Let us explain the principle of the improvement of the purity of the ion beam. We assume that the ion beam produced in the ion source, which consists of N^+ ion and impurity of H^+ ion, is injected into the BPA. Each ion of N^+ and H^+ is accelerated in the 1st gap toward the drift tube by the negative voltage of the bipolar pulse and the length of H^+ beam is much longer than that of N^+ beam due to the difference of the velocity, where N^+ and H^+ ion beams are schematically described in Fig. 1. Assuming that the length (L) of the drift tube is designed to be same as the beam length of N^+ beam with a beam pulse duration τ at an acceleration voltage V_{OUT}, the condition for the most effective acceleration of N^+ beam is satisfied. It is, for example, calculated to be L=11.6 cm when V_{OUT} = 200 kV and τ = 70 ns. When N^+ beam with the length of 11.6 cm reaches the 2nd gap, the polarity of the pulse is reversed and the positive voltage is applied to the drift tube, which again accelerates the N^+ beam in the 2nd gap. On the other hand, since the length of H^+ beam at V_{OUT} = 200 kV and τ = 70 ns is L = 43.3 cm, 73 % of the H^+ beam is out of the drift tube and decelerated in the 2nd gap by the first pulse (negative voltage pulse). Hence 73 % of H^+ beam is removed in the BPA. As a result, the purity of the ion beam is improved.

3. Experimental Apparatus

Figure 2(a) shows the schematic configuration of the BPA in the present experiment. The system consists of a bipolar pulse generator and an accelerator. The bipolar pulse generator consists of a Marx generator and a pulse forming line (PFL). The designed output of the bipolar pulse generator is the negative and positive pulses of voltage ±200 kV with pulse duration of 70 ns each. In the system, the double coaxial type is employed as the PFL for the formation

of the bipolar pulse. The line consists of three coaxial cylinders with a rail gap switch on the end of the line, which is connected between the intermediate and outer conductors. The characteristic impedance of the line between the inner and intermediate conductors and one between the intermediate and outer conductors are 6.7 Ω and 7.6 Ω, respectively. The PFL is charged positively by the low inductance Marx generator with maximum output voltage of 300 kV through the intermediate conductor. The rail gap switch is filled with pure SF_6 gas and the pressure can be adjusted to control the optimum trigger timing.

Figure 2(b) shows in detail the acceleration gap design and experimental setup of the BPA, which consists of a grounded anode, a drift tube, a grounded cathode and two magnetically insulated acceleration gaps with gap length of d_{AK}=15 mm each. The anode and the cathode are the copper electrodes of diameter 78 mm, thickness 5 mm. The electrodes are uniformly drilled with apertures of diameter 4 mm, giving beam transmission efficiency of 58 %. In order to produce magnetic fields for suppression of the electron flow in both acceleration gaps, a magnetic field coil of grating structure is used and installed on the rectangular drift tube. The uniform magnetic field with strength of 0.3-0.4 T is produced in direction transverse to the acceleration gap by a capacitor bank with capacitance of 500 μF and charging voltage of 4 kV. To obtain higher transmission efficiency of the ion beam, right and left sides of the coil consist of 8 blades each and have a grating structure. Each of the blades (10 mm^W x 118 mm^L x 1 mm^T) is connected in series and works as an 8-turn coil. Since at peak of the magnetic field, the bipolar pulse voltage is applied to the drift tube, the pulsed current produced by the capacitor bank is applied to the magnetic coil through an inductively isolated current feeder.

A gas puff plasma gun, which consists of a gas puff valve and a coaxial plasma gun, was used as the ion source and installed inside the anode as shown in Fig. 2(b). The vessel of the gas puff is filled with N_2 gas. When the pulsed current is applied to the drive coil of the gas puff by discharging the capacitor bank with capacitance of 5 μF and charging voltage of 6 kV, the valve of the gas puff is opened and the filled N_2 gas is injected into the plasma gun. The ion source plasma is produced by discharging the capacitor bank with capacitance of 1.5 μF and charging voltage of 15 kV at the optimum timing.

The charging voltage of the PFL (V_{PFL}) and the output voltage (V_0) of the bipolar pulse were measured by the resistive voltage divider placed near the rail-gap switch, respectively. The ion current density of the pulsed ion beam was measured by a biased ion collector (BIC) placed inside the drift tube and the cathode.

4. Experimental Results and Discussion

First, the BIC was installed at 60 mm downstream from the anode surface inside the drift tube to measure the ion beam accelerated in the 1st gap by the first pulse of the bipolar pulse. Figure 3 shows the typical waveforms of the charging voltage of the PFL (V_{PFL}), the output voltage (V_0) of the bipolar pulse and the ion current density (J_i) of the pulsed ion beam accelerated in the 1st gap. The bipolar pulse generator was

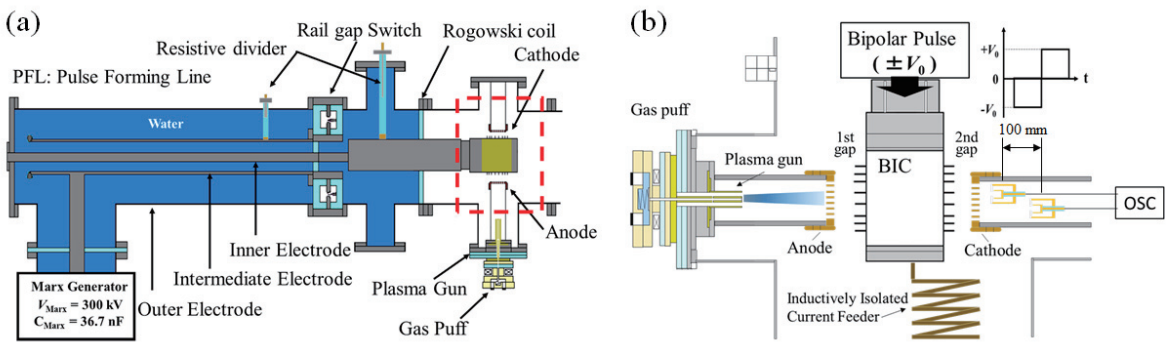

Fig. 2 (a) Schematic configuration and (b) acceleration gap design and experimental setup of BPA.

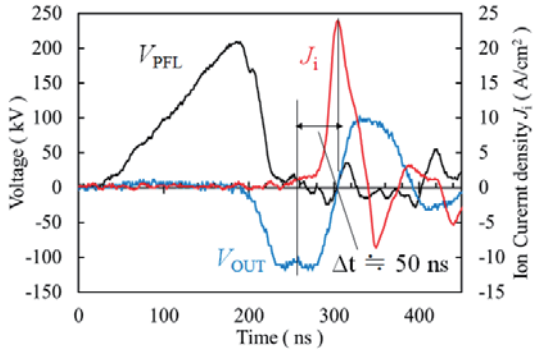

Fig. 3 Typical waveforms of PFL's charging voltage (V_{PFL}), bipolar pulse voltage (V_0) and ion current density (J_i).

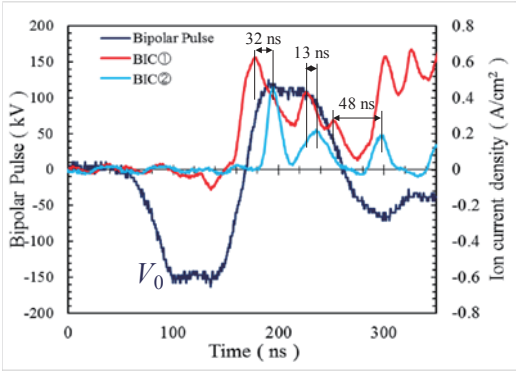

Fig. 4 Typical waveforms of bipolar pulse voltage (V_0) and ion current density (J_i) measured at 10 and 110 mm from grounded cathode.

operated at 70 % of the full charge condition of the Marx generator. When the bipolar pulse of -118kV, 75 ns (1st pulse) and +102 kV, 70 ns (2nd pulse) was applied to the drift tube, the ion beam with a current density of Ji = 24 A/cm^2 and a pulse duration of 30 ns (FWHM) was obtained. The energy of the pulsed ion beam can be estimated from a time of flight delay. Assuming that the time of flight delay is 50 ns, the velocity of the ion is calculated to be 1.2×10^6 m/s. It is reported in Ref. [14] that the accelerated ion beam consists of the singly and doubly ionized nitrogen ions and impurity of proton and N^+ is the dominant component. Thus, the velocity corresponds to the ion energy of 105 keV. In the view of fact that the pulsed ion beam has the broad energy spectrum with ion charge states of 1+ – 2+ as mentioned in Ref. [9], the ion energy estimated by the time of flight seems to be in reasonable good agreement with the acceleration voltage i.e., 1st pulse voltage V_0= −118 kV of the bipolar pulse.

Next, in order to confirm the acceleration of the pulsed ion beam in the 2nd gap, the energy of the pulsed ion beam was evaluated by a time of flight method (TOF). As shown in Fig. 2(b), two BICs were placed at 10 and 110 mm downstream from the grounded cathode, respectively. Figure 4 shows the typical waveforms of the output voltage (V_0) and the ion current density (J_i) measured by each BIC. When the Marx generator for the bipolar pulse was operated at 80 % of the full charge condition, the bipolar pulse with voltage of about −160 kV and +120 kV and pulse duration of about 70 ns (FWHM) each was applied to the drift tube. The ion current density has three peaks. As seen in Fig. 4, the TOF delay time of each peaks between two BIC signals are 32, 13 and 48 ns, which give the velocity of 3.2×10^6, 7.7×10^6 and 2.1×10^6 m/s, respectively. We estimate the ion energy for both N^+ and H^+ from each velocity, since the ion beam accelerated in the 1st gap contains the nitrogen ion and impurity of proton. Table 1 shows the estimated ion energy. In the present experimental condition, when the polarity of the bipolar pulse is reversed, singly ionized nitrogen ions do not yet reach the 2nd gap. Thus, it is evident that the 1st peak of the ion current density corresponds to the proton, which is accelerated in the 1st gap and subsequently decelerated in 2nd gap at a fall of the first (negative) pulse of the bipolar pulse. Taking in to account the result that the proton with the same energy as the acceleration voltage was observed in the ion beam accelerated in the 1st gap, it is considered that the impurity of proton is removed in the BPA. Comparing the estimated ion energy with the total acceleration voltage (280 kV) of the applied bipolar pulse, we find that the 2nd and 3rd peaks of J_i correspond to H^+ and N^+, respectively. The pulsed ion beam with H^+ and N^+ seems to be again accelerated in the 2nd gap by the second pulse of the bipolar pulse.

Table 1 Estimated Ion energy of N^+ and H^+

	1st peak	2nd peak	3rd peak
N^+	714 keV	4320 keV	317 keV
H^+	51 keV	309 keV	23 keV

5. Conclusions

We have developed a bipolar pulse generator and a prototype of the accelerator to perform proof of principle experiments on the BPA. We found that the ion beam was successfully accelerated in the 1st and 2nd gaps by applying the bipolar pulse to the drift tube. However, the only evaluation of the ion energy via time of flight is not enough to confirm the principle of the BPA. We are planning to evaluate the ion species and the energy spectrum of the ion beam in detail by using Thomson parabola spectrometer. In addition, We need to optimize the beam quality by modifying the gap structure to increase the beam current.

Acknowledgement

This work was partially supported by JSPS KAKENHI Grant Number JP 15H03961.

References

[1] J. A. Nation, “High Power Electron and Ion Beam Generation”, Particle Accelerators, Vol.10, pp.1-30 (1979).

[2] S. Humphries, Jr , "Intense pulsed ion beams for fusion applications", Nucl. Fusion, Vol.20, pp.1549-1612 (1980).

[3] Y. Nakagawa et al., "Modification of solid surface by intense pulsed light-ion and metal-ion beams", Nucl. Instrum. Method B, Vol.39, pp.603-606 (1989).

[4] G. P. Johnston et al., "Preparation of diamondlike carbon films by high-intensity pulsed-ion-beam deposition", J. Appl. Phys., Vol.76, No.10, pp.5949-5954 (1994)

[5] J. Khamsuwan et al., "High-energy heavy ion beam annealing effect on ion beam synthesis of silicon carbide", Surface & Coatings Technology, Vol.206, pp.770-774 (2011).

[6] Y. Hashimoto et al., "Generation and focusing of intense ion beam with an inverse pinch ion diode", Jpn. J. Appl. Phys., Vol.31, pp.1922-1927 (1992).

[7] X. P. Zhu et al., "Characterization of a high-intensity bipolar-mode pulsed ion source for surface modification of materials", Rev. Sci. Instrum., Vol.73, pp.1728-1733 (2002).

[8] K. Masugata et al., "Diagnosis of high-brightness ion beams produced in point pinch diodes", J. Appl. Phys., Vol.80, pp.4813-4818 (1996).

[9] H. Ito et al., "Diagnosis of high-intensity pulsed heavy ion beam generated by a novel magnetically insulated diode with gas puff plasma gun", Rev. Sci. Instrum., Vol.79, 103502 (2008).

[10] H. Ito et al., "Characteristic observation of intense pulsed aluminum ion beam in magnetically insulated ion diode with vacuum arc ion source", IEEE Trans. Plasma Sci., Vol.37, pp. 1879-1884 (2009).

[11] K. Masugata et al., "Development of bipolar-pulse accelerator for intense pulsed ion beam acceleration", Nucl. Instrum. & Methods in Phys. Res. A, Vol.535, pp.614-621 (2004).

[12] H. Ito et al., "Bipolar pulse generator for intense pulsed ion beam accelerator", Rev. Sci. Instrum., Vol.78, 013502 (2007).

[13] H. Ito et al., “Characteristics of Pulsed Heavy Ion Beam Generated in Bipolar Pulse Accelerator”, IEEJ Trans. on Fundamentals and Materials, Vol.135, pp.136–141 (2015).

Propagation of Intense Electron Beams through A Rectangular Waveguide

Dai Takagi, Momoko Katsuoka, Yukihiro Soga, Keiichi Kamada

Graduate School of Science and Technology, kanazawa Univercity, Kanazawa, Ishikawa, 920-1192, Japan

ABSTRACT

Cylindrical intense electron beams were injected into a thin rectangular waveguide. Beam cross-sectional profiles were observed along the beam axis. The center of the beam cross section was shifted when the beam was not injected just on the center of the height. The periodical deformation of the beam cross-sectional shape was also observed. When two beams were injected, centers of beams rotated each other and decreased their distance. Using a simple model with momentum equations of linear density elements of the beam, it was clear that E×B drift with the asymmetric self electric field and the magnetic field on the beam caused those phenomena.

Keywords

Intense electron beam, REB, free electron maser, rectangular waveguide, intense THz souce

1. Introduction

Free electron maser using an intense mildly relativistic electron beam (REB) is one of the candidates of a compact intense Tera-Herz source. As the radiated frequency increases, not only the wiggler structure but also the cross-section of the beam decreases. For the cylindrical structure the decrease of the beam radius results in the decrease of the output power. Though a sheet electron beam propagated along a rectangular waveguide with a large aspect ratio was proposed to provide a high total current, its propagation suffered considerable deformation of its cross-sectional shape from diocotron instability[1-4].

In this paper, the propagation of cylindrical electron beams instead of the sheet beam through a rectangular tube is investigated to use an energy source of a planar FEM. And a simple model was tested to explain the experimental phenomena.

2. Experimental Setup

Schematic of the experimental apparatus is shown in Fig. 1. A carbon cathode and a carbon annular anode with the same diameter were used in one beam experiment. A large circular cathode or a rod cathode with an anode with two holes was used in two beams experiments. Rectangular waveguides of 14.5 mm x 25 mm and 10.5 mm x 76 mm were utilized. The waveguide was set in a circular vacuum tube. Each long side was set horizontally as shown in Fig.1. The axial length of the waveguide was nearly 1 m. Axial magnetic field with strength of 0.6-1 T was

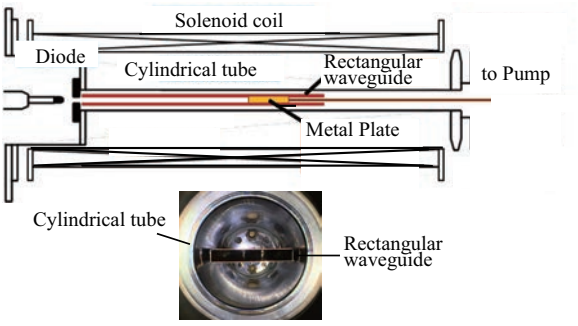

Fig. 1. Schematic of the experiment. A rectangular waveguide was set in a cylindrical vacuum tube.

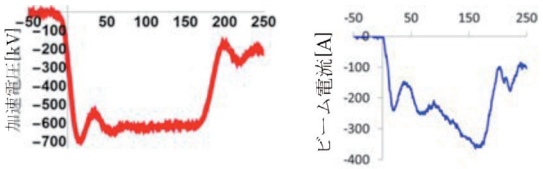

Fig. 2. Typical waveforms of the diode voltage (left) and the beam current (right).

applied by a solenoid coil.

Cylindrical REB(s) with energy of around 600 keV, current of 100-500 A, diameters of 3, 5, 8, 10 mm, duration of 150 ns was injected into a rectangular waveguide. Typical waveforms of the diode voltage and the beam current are shown in Fig. 2. When two beams were injected, the current density of two beams was nearly the same.

A metal plate grounded through 0.1 Ω register with low inductance was used to detect the beam current. The damage pattern on the metal plate was used to observe the integrated profile of the beam cross-section. The border of the damage pattern was estimated as shown in Fig. 3. The center of profiles was also estimated by the damage pattern.

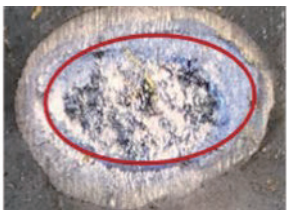

Fig. 3. A damage pattern and its estimated border (red line).

A simple model of the cylindrical beam propagation through a rectangular waveguide was employed to explain the phenomena observed in the experiment. The axial beam length was supposed to be infinite. The density profile of the beam cross-section is considered to be uniform. The beam cross-section is divided into 80 linear density elements. Momentum equations of linear density elements of the beam were calculated. In the equation of each element described below was employed where m, q are the mass and charge of line density for a unit axial length and γ is the relativistic factor.

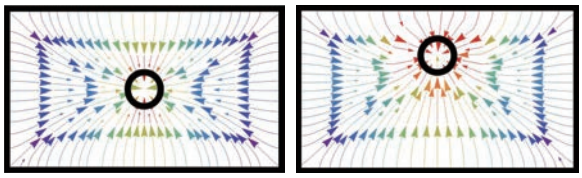

Fig.4 The electric lines of force of a circular beam in a rectangular waveguide. Left: the center of the beam is just on the vertical midpoint of the waveguide. Right: the beam located near the upper wall.

$$\frac{d}{dt}\ \gamma m\vec{v} = q\ (\vec{E} + \vec{v} \times \vec{B})$$

As the electric field E on each element, the electric field of the other linear charges and that of linear image charges by all elements are taken into account. For the magnetic field B, the axial guide magnetic field and the magnetic field of the other linear currents are calculated. The electric field on the cross-section of the waveguide calculated in the model is shown in Fig. 4. The electric field is different in strength and direction on the cross-section of the beam. The electric field is symmetric about horizontal centerline of the waveguide height when the center of the beam cross-section is on the vertical center of the waveguide. The electric field becomes asymmetric, when the beam center is not on the vertical center of the waveguide. In Fig. 4 right, the electric field near the wall was stronger than the opposite side.

3. Results and Discussion

3.1 Shift of the center of the profile

A beam was injected into a 25 x 14.5 mm rectangular waveguide. A longer 25 mm side was set horizontally. Damage patterns at the entrance (z=0 mm) and z=1000 mm downstream side of the waveguide were observed. The beam was injected into the rectangular waveguide at the center horizontally. When the center of the beam cross-section was just on the vertical center point of the waveguide at the entrance, the center of the beam

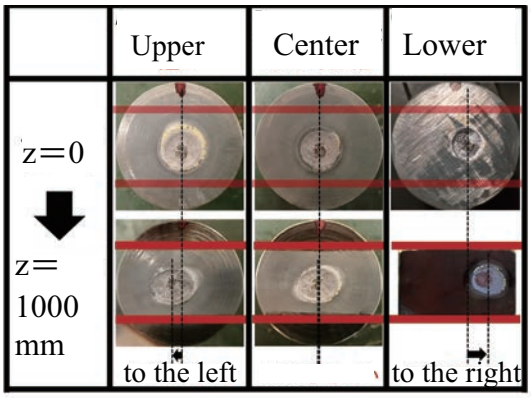

Fig. 5. Upper: when the center of the beam was injected near the upper wall, the beam shifted to the left at downstream side. Center: the center is on the vertical center point, no shift. Right: near the lower wall, the beam shifted to the right. Beam diameter was 8 mm. 14.5 x 25 mm waveguide was used.

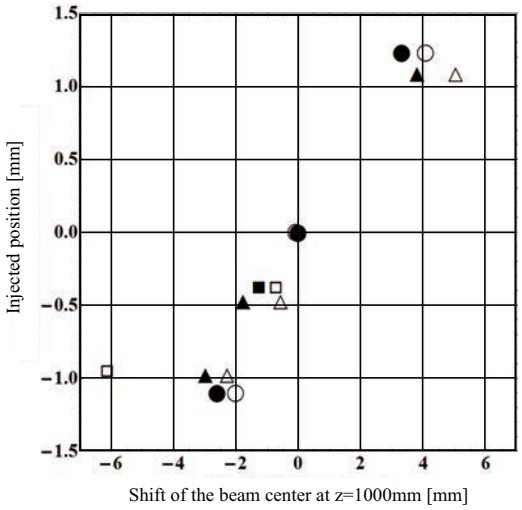

Fig. 6. The horizontal shift of the beam center at 1000 mm downstream side for various injection positions. 0 mm is the center of the vertical size of the waveguide. Circle : beam diameter=5mm, triangle : 8mm, rectangle:10 mm. Open and filled symbols are experimental and calculated results, respectively. 14.6 x 25 mm waveguide was used.

showed no horizontal shift at the downstream side. If the center of the beam was not injected at vertical

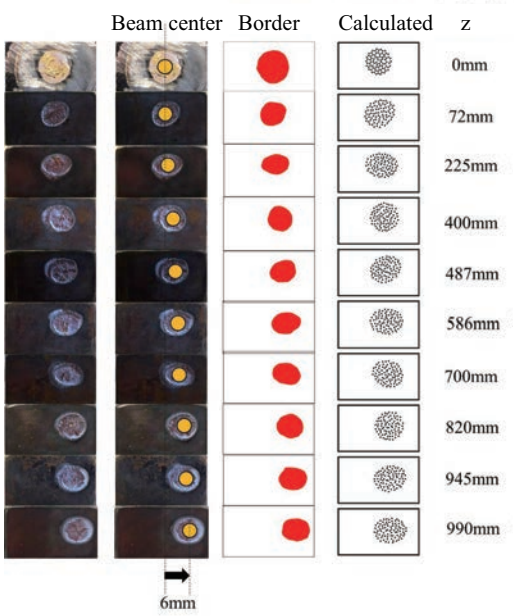

Fig. 7 . Damage patterns along z-axis. In addition to the horizontal shift of the beam center, the cross-sectional shape of the beam was deformed. The calculated results showed good agreements with the experimental ones.

center point of the waveguide, it was shifted to the right or left horizontally at the downstream side, as shown in Fig. 5. The shift at 1000 mm downstream side is plotted in Fig. 6 against the injection position of the cross-sectional center of the beam where 0 mm is the center of the waveguide height for various beam diameters. The calculated results showed good agreements with the experimental data. The distance between two centers increased, the shift increased. The direction of the shift was opposite across the vertical center of the waveguide. The direction of the shift was the equal to that of E x B force using vertical E of the stronger side. The center of the beam shifted because of the asymmetric E x B force.

3.2 Deformation of the beam cross section

The cross-sectional shape of the beam was deformed periodically along the axial distance as shown in Fig, 7 where 25 x 14.5 mm waveguide was used. In addition to the shift of the center of the beam, the circular shape of the beam cross-section

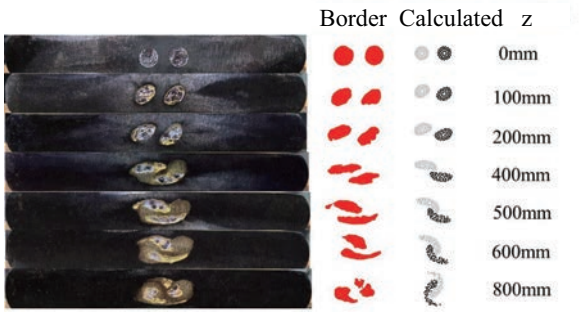

Fig. 8. Two beams were rotated each other. The distance between beam centers were 7.5 mm at z-0 mm. Beam diameter was 5 mm. 10.5 x 76 mm waveguide was used.

turned to elliptical and back to circular repeatedly. The beam cross-sectional shapes were observed nearly circular at the injected point (z=0mm), z=400 mm and 820 mm. The calculated shape of the beam cross-section at each position corresponds well with the experimental one. Similar experimental and calculated results were obtained by using the 10.5 x 76 mm waveguide.

When the guide magnetic field was increased, the periodical length of deformation was increased. It could be reasonable because the drift velocity E/B was decreased as the B increased.

The deformation of the beam cross-sectional shape came from E x B drift with the different electric field in strength and direction on the beam cross-section as shown in Fig. 4.

3.3 The rotation of two beams

Two beams 7.5 mm apart were injected into the 10.5 x 76 mm waveguide. The beams were rotated each other and their shapes of cross-section were deformed as shown in Fig. 8. The distance between two beams was also decreased along the axial length. When the distance of two beams was 38 mm, no mutual rotation was observed and their shapes of cross-section deformed independently. In Fig. 8, the calculated shapes of the cross-section were also depicted and they show good correspondence with the experimental results. When the distance of two beams was narrow, two beams interacted each other as expected.

When the experimental parameters are given, the simple model could estimate the distance of two beams that propagate without rotation.

4. Conclusions

When an electron beam propagates through a rectangular waveguide, a shift of the beam center and periodical deformation of the cross-sectional shape of the beam were observed. When two beams were injected with narrow space, they rotated each other, the distance between two beams was decreased and their cross-sectional shapes were deformed.

A simple model with momentum equations of linear beam elements showed good agreements with experimental results. The shift of the beam center, the periodical deformation of the cross-sectional shape of the beam and the rotation of the beams are originated from the E x B drift motion of each elements. The simple model could be useful to estimate the parameters of a rectangular tube and beams for long range multi-beam propagation.

References

[1] R. H. Levy, Phys. Fluids, vol. 8. 1288 (1965)

[2] E. R. Stanford et.al., Nucl.Instr.and Meth. A296, 521 (1990).

[3] H. S. Uhm et.al. , Phys. Plasmas, vol. 1, 3686, (1994).

[4] H. Yin et.al., Chin Phys. B, vol. 20, 104101, (2011).

Output Evaluation of Microwave Pulse Emitted from Axially-Extracted Vircator with Resonance Cavity

Tsukasa Nakamura, Motohiro Teramae, Fumiya Niwa, Hiroaki Ito

Graduate school of science and engineering for education , University of Toyama, Toyama 930-8555, Japan

ABSTRACT

The high power microwave generated in an axially extracted virtual cathode oscillator (vircator) has been studied experimentally. The vircator is driven by a Marx generator and pulse forming line. To improve the efficiency, we installed a cavity in the vircator, since the narrowing of the output microwave frequency leads to the improvement of the efficiency. The electron beam diode was an axially extracted vircator with the solid type aluminum cathode of 60 mm in diameter and the stainless steel mesh anode. The disc resonator with an extraction window was placed at the distance away from an anode with anode-cathode gap of 8 mm. The electronic field of output microwave was measured by varying the cavity length and the aperture of cavity to analyze the cavity effect. The maximum output power of the microwave from the vircator has been measured to be about 80 MW in this experiment when the diode voltage and diode current are 280 kV and 12 kA, respectively. In addition, we evaluate the characteristics of output microwave with the resonator by analysis of the time-dependent frequency analysis.

Keywords

High-power microwave, virtual cathode oscillator, vircator, resonance cavity

1. Introduction

Radiation sources of the high-power microwave are being developed for applications in plasma heating, particle acceleration, high-power radar, and many other industrial and military fields [1,2]. A number of high-power microwave sources have been developed, such as Virtual Cathode Oscillator (vircator), Magnetron, Klystron, Gyrotron and so on. The vircator has remarkably attracted attention over other kinds of high-power microwave sources. The vircator has the attribute of high-power capability, wide frequency tuning ability, and conceptual simplicity [3]. It is possible to generate high-power microwaves ranging from a few tens of megawatts up to a few gigawatts at frequency from a few hundreds of MHz to a few tens of GHz. However, the vircator has difficult problems in low efficiency of beam-to-microwave power conversion and wide frequency bandwidth [3]. The many researchers have been making research efforts and experimental studies to improve the microwave conversion efficiency and oscillation frequency control [4-8]. Despite these efforts, the best conversion efficiency is still not higher than 10% and an order of magnitude less than that of other high-power generators.

It has been found that the conversion efficiency depends on the electromagnetic field strengths in the interaction region around the virtual cathode. This field plays important roles on both modulating the electron beam and extracting energy from the electron beam. In order to improve the conversion efficiency and narrow the output frequency, the vircator with a resonance cavity has been proposed and proven successful by several research groups [9, 10]. When the resonant mode has an electric field component along the direction of the virtual cathode oscillation, the beam-field interaction can be enhanced by feeding back the microwave field to the virtual cathode and the field can extract higher energy from the virtual cathode oscillation at the resonant frequency. Thus, the choice

of the mode is an important consideration in the design of the drift space. The experiments were performed using an axially extracted vircator with the resonance cavity, which was installed by inserting a movable disc plate with an extraction window in the drift space. This results in an axial electron beam and a virtual cathode oscillating along the vircator axis. The axial position of this plate was varied during the experimental series. In this paper, we investigated the influence of the resonant cavity structure, i.e. length and aperture size, on the electric field and frequency of the microwave emitted from the vircator and evaluated the output microwave power. In addition, the obtained output microwave was evaluated by the time-dependent frequency analysis (TFA) [11].

2. Principle of Vircator

The intense electron beam is used for the generation of microwave by the vircator. The electron beam diode consists of a cathode and an anode. When a high pulsed negative voltage is applied to the cathode, electrons are emitted from the surface of the cathode. The electron beam passes through the anode, which is usually a thin foil or a mesh, and is injected into drift space on the other side of the anode. When the injected electron beam current exceeds the space charge limited current in the region behind the anode, a virtual cathode, which is an unstable region of negative potential, is formed at the same distance as AK gap. Most of the electrons in the beam lose their kinetic energy and are then reflected back toward the anode. The mechanism for microwave generation in the vircator can generally be explained by two dynamical mechanisms [2, 12]. The first is electron reflection in the potential well formed between the real and virtual cathodes. The radiation frequency due to electron reflexing depends on the AK gap and the beam energy. The frequency is approximately given by

$$f_e = \frac{v_e}{4d_{AK}} \approx \frac{c\sqrt{\gamma^2 - 1}}{4d_{AK}\gamma}$$

where v_e is the velocity of the electron, d_{AK} is the distance between the anode and the cathode, and c is the velocity of light. The relativistic factor γ is given by

$$\gamma = \frac{1}{\sqrt{1-(v_e/c)^2}} = 1 + \frac{eV_0}{m_e c^2}$$

The second is an oscillation of the virtual cathode in time and space. The oscillation frequency is given by

$$f_{vc} = \frac{5}{4\pi}\omega_p = \frac{5}{4\pi}\sqrt{\frac{e^2 n_b}{\varepsilon_0 m_e \gamma}}^{1/2}$$

$$= \frac{5}{4\pi}\sqrt{\frac{e^2}{\gamma\varepsilon_0 m_e}}\sqrt{\frac{1}{e\beta c}}\left(\frac{4\varepsilon_0}{9}\left(\frac{2e}{m_e}\right)^{1/2}\frac{V_0^{3/2}}{d_{AK}^2}\right)^{1/2}$$

where ω_p is the electron plasma frequency, n_b is electron beam density derived by the space charge limited current, e and me are the electron charge and mass, respectively, ε_0 is the vacuum permittivity, V_0 is the applied voltage across the AK gap, and β=v/c. These two oscillation frequencies are fundamentally determined by the geometric structure, the applied voltage and the electron beam parameter.

3. Experimental Setup

Figure 1 shows a schematic configuration of the pulse power system for the axially-extracted vircator

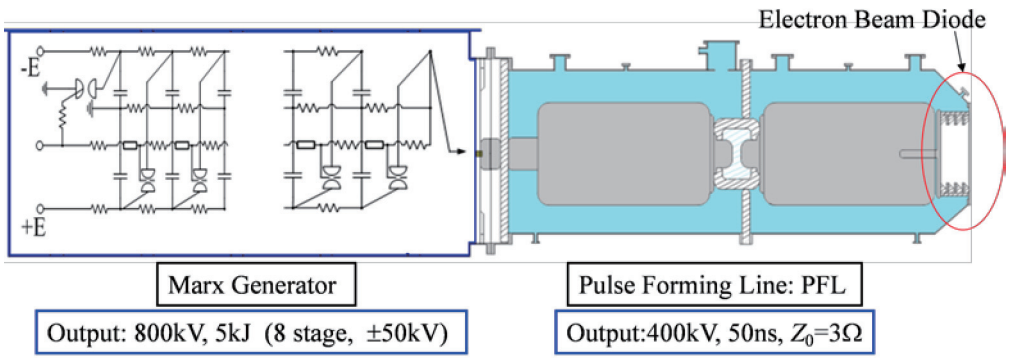

Fig.1 Schematic diagram of Pulsed Power system

used in this study. The pulse power system for generation of the high-power microwave consists of a high-voltage generator, a single pulse forming line (PFL), a gas SF_6 spark gap and a pulse transmission line. The high-voltage generator is an eight-stage bipolar Marx generator with the maximum output of 800 kV and the stored energy of 5 kJ. The PFL is filled with the deionized water as a dielectric. The designed parameters of the PFL are characteristic impedance of 3 Ω, and electrical length of 50 ns. In this experiment, the pulsed power system was operated in negative-output mode and the charging voltage of Marx generator was set to 24 kV and to operate in a single-shot mode.

Figure 2 shows the schematic structure of the axial vircator and the microwave measurement setup. The high-voltage pulse generated from the pulsed power system is applied to the cathode of the electron beam diode. A vacuum explosive electron emission diode was used to generate an intense relativistic electron beam. The diode consists of an aluminum planar disk cathode of 60 mm in diameter and a stainless-steel meshed anode with a transparency of ~65%. As shown in Fig. 2, both anode and cathode electrodes are plane surfaces that are at right angles to the vircator symmetry axis. To improve the microwave efficiency and control the output frequency, the resonance cavity was installed by placing a movable disc plate with a center hole at the distance (L) away from an anode. In this resonator configuration, it is expected that the dominant mode might be the transverse magnetic (TM) mode, which have an axial electric field that strongly couples to the oscillating virtual cathode's electric field. The output microwave was measured

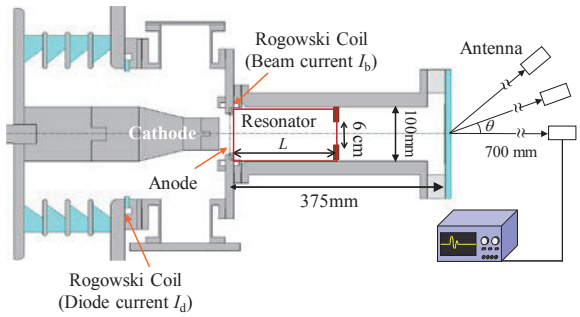

Fig. 2 Schematic structure of axially extracted vircator and microwave measurement setup.

varying both the distance (L) and the diameter (a) of extraction window to analyze the resonator effect. From previous experimental results, the AK gap d_{AK} was set to be 8 mm regarding small shot-to-shot variations and good durability of the meshed anode.

The output microwave from the vircator traveled along a circular waveguide of 100 mm in diameter and 375 mm in length and is emitted into free space through an acrylic window. The output power of the emitted microwave was evaluated by measuring the spatial distribution of the microwave from the vircator. The open ended rectangle waveguide (WR187: 4.75 × 2.22 cm^2) is utilized as the receiving antenna, which is placed in the step of 10° in the azimuthal direction at a distance of 0.7 m away from the window. The temporal waveform of the output microwave was obtained by using a crystal diode and recorded by a digital oscilloscope with a bandwidth of 200 MHz and a sampling rate of 2 GS/s, together with the beam parameters (voltage and current). In order to carry out Fourier transforms and TFA, the signal from the antenna was also recorded by a high-speed digital oscilloscope with a sampling rate of 40 GS/s through a coaxial RF cable.

A resistive $CuSO_4$ voltage divider was used to measure the output voltage (V_{PFL}) of the pulsed power system and placed at the edge of PFL. The diode voltage (V_d) applied to the cathode is calculated by the inductive correction, since the inductance of the transmission line from the resistive divider to the cathode is ~100 nH. The diode current (I_d) and the beam current (I_b) passed through the anode were monitored by Rogowski coil at the upstream and downstream of the anode.

4. Experimental Results

Figure 3(a) shows the typical waveforms of the diode voltage V_d, the diode current I_d and the electric field of the microwave with no resonance cavity. The diode voltage increases up to 200 kV within 100 ns and the diode current rises with the diode voltage and has a peak of 14 kA. It can be seen from the waveform of the microwave field that the microwave is emitted at the rise time of V_d. Figure 3(b) shows the Fast Fourier

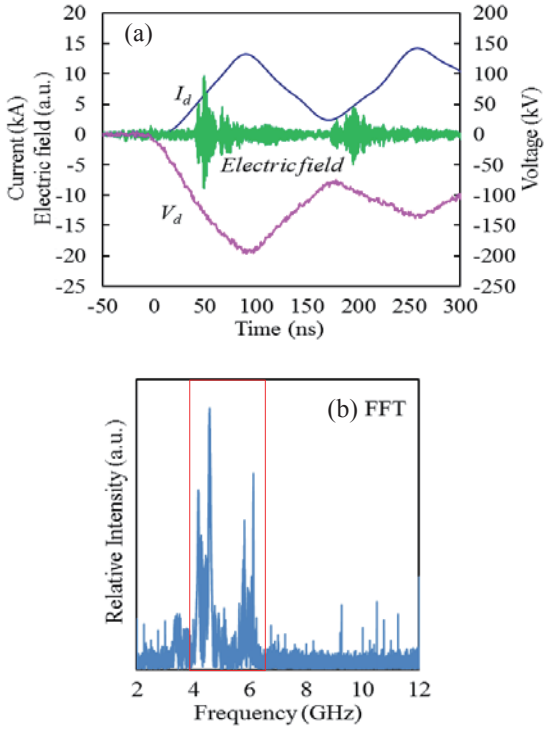

Fig. 3 (a) Typical waveforms of diode voltage V_d, diode current I_d and electric field of microwave with no cavity and (b) FFT of microwave signal shown in Fig.3(a).

transform (FFT) of the microwave waveform. As seen in Fig. 3(b), the bandwidth of the microwave frequency is broad and the main frequency components can be identified as ~4.4 and ~5.9 GHz. This result indicates that two mechanisms of microwave radiation exist together, namely, the electron reflex between the real and virtual cathodes as well as the virtual cathode oscillation. From above-mentioned equations, the low frequency is related to the virtual cathode oscillation, while the high frequency corresponds to the electron reflex process.

Figure 4 shows the microwave output signal recorded by the high-speed digital oscilloscope for two aperture diameters (a=4, 6 cm) of the cavity extract window at various cavity lengths. The waveforms of the diode voltage applied to the cathode and the microwave field without the cavity are shown as the reference. It can be clearly seen from Fig. 4 that the amplitude of the microwave field with the cavity is higher than that without the cavity. The experimental results show that the emission time of microwave is more stable at the extract window diameter a=6 cm

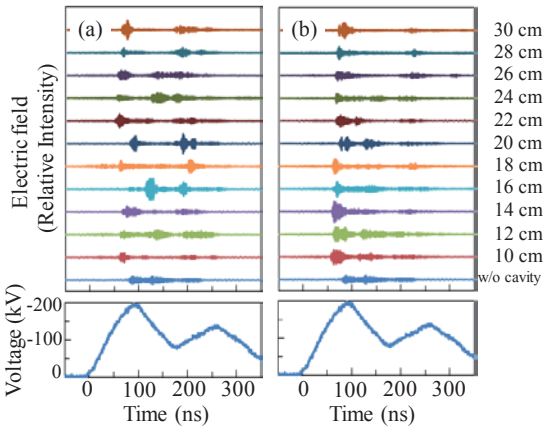

Fig. 4 Waveform of microwave electric field as a function of cavity length at extract window diameters (a) a=4 cm, and (b) a=6 cm.

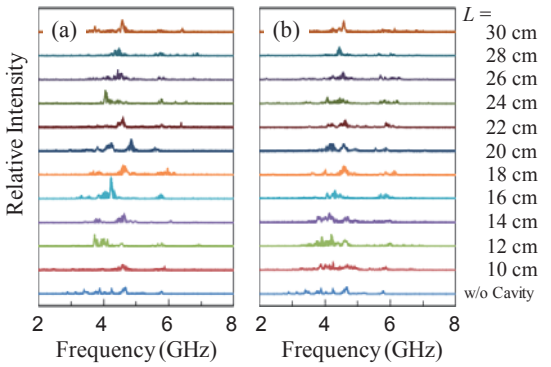

Fig. 5 FFT of the microwave E-field of Fig.5 as a function of cavity length at extract window diameters (a) a=4 cm and (b) a=6 cm.

than at other diameters. The effect of the cavity structure on the output microwave frequency is investigated by FFT. Figure 5 shows the FFT of each microwave E-field shown in Fig. 4. It turned out from Fig. 5 that the frequency spectrum has narrow bandwidth and sharp peak by installing the resonance cavity. The microwave mode depends on the cavity structure, i.e. the ratio of the diameter D and the length L. The microwave mode can be evaluated by varying the cavity length, since the cavity diameter is fixed to D=10 cm. Considering that the microwave frequency is in range of 4-5 GHz and that $(D/L)^2$ is set from 0.1 to 1 in the present experimental setup, we find from Fig. 5 that the frequency corresponding to TM_{01p} or TM_{11p} modes is tuned to resonate with the broadband

virtual cathode oscillation, while the nonresonant frequencies are suppressed. Thus, the frequency bandwidth of the emitted microwave becomes narrower.

Figure 6 shows the spatial distribution of the received microwave power as a function of the cavity length. It turns out that the spatial distribution of the received power is almost 0 at the axis and has a peak around 30°. It is expected that the dominant mode might be the TM mode, since the current oscillation is longitudinal direction. It is observed experimentally that the most dominant frequency of the microwaves generated from the vircator is about 5 GHz which is also comfortably above the cutoff frequency of the TM mode. Therefore, it is believed that the dominant emission mode of the microwave from the vircator is mainly TM mode in this experiment.

Assuming that the electric field of the emitted microwave is the axial symmetry, the total radiated power P of the microwave is given by

$$P = \frac{2\pi z^2}{A_{eff}} \int P_R(\theta) \sin\theta \, d\theta \ ,$$

where z is distance between the transmitting and receiving antenna, $P_R(\theta)$ is a received power at the angle θ from the central axial in the azimuthal direction, A_{eff} is the effective area of the receiving antenna and is given by

$$A_{eff} = \frac{G\lambda^2}{4\pi} = \frac{2ab}{\pi^2} \cdot \frac{\left(1+\sqrt{1-f_c^2/f^2}\right)^2}{\sqrt{1-f_c^2/f^2}}$$

where G is an antenna gain, f_c is the cutoff frequency of the antenna, and a and b are the short and long sizes of the rectangular waveguide, respectively. Table 1 shows the total radiated power of the microwave calculated from the spatial distribution shown in Fig. 6 by using above-mentioned equations. The microwave power depends on the cavity length and the maximum power of 79 MW is observed at the cavity length of L=14 cm. The output microwave power increased by 15% compared to that without the cavity.

Table 1 Microwave Power radiated from vircator as a function of cavity length (L)

w/o	L=10cm	L=12cm	L=14cm
70 MW	43 MW	64 MW	79 MW

The oscillation frequency in the vircator depends on electron-beam parameters such as voltage, current density, and the geometric structure of the diode. As a result, the virtual cathode oscillations vary with time during the output pulse because of the diode gap closure due to cathode plasma expansion. According to previous experimental results, at the AK gap distance of d_{AK}=4 mm, the microwave frequency

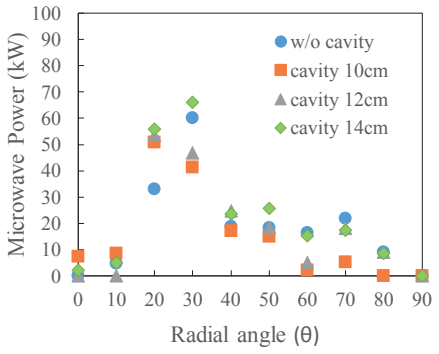

Fig. 6 Spatial distribution of received microwave power as a function of cavity length.

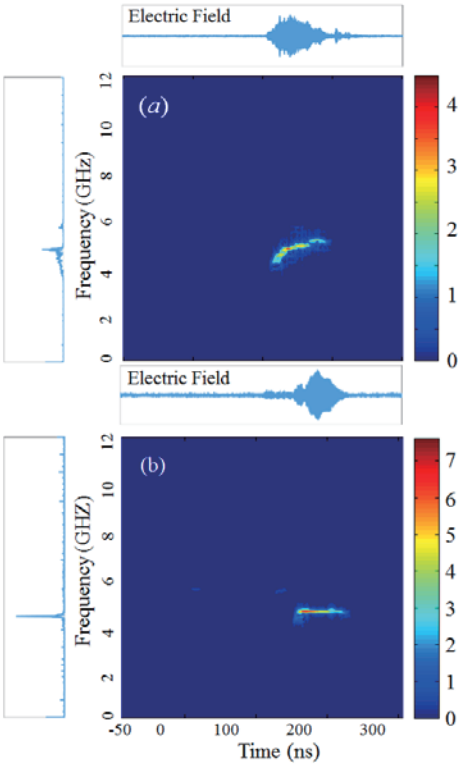

Fig. 7 Time evolution of microwave frequency spectrum (a) without cavity and (b) with cavity.

increases from 6 to 12 GHz during the period of 0-50 ns and the emission is broadband. The time frequency analysis was carried out for evaluation of the frequency stabilization of the virtual cathode oscillation. Figure 7 shows the time evolution of the microwave frequency spectrum with no cavity and with the cavity, where the AK gap is d_{AK}=12 mm and the cavity is set to the length of L=10 cm and the extract window of a=6cm. In Fig. 7, a time-window width of 12.8 ns (512 data points) was shifted by the step of 0.25 ns and the horizontal and vertical axes represent the center of the time window and the spectrum intensity obtained within each window by the blackness variation, respectively. It can be seen from Fig. 7 that in the case of no cavity, the output frequency increases from 4.1 to 4.9 GHz with time and the bandwidth of the emission is broad, while in the case of the vircator with the cavity, the constant frequency of ~4.3 GHz was observed over the microwave emission and the spectrum became sharp. This result shows that the frequency stabilization of the virtual cathode oscillator is achieved by installing the resonant cavity.

4. Conclusions

We have investigated experimentally and numerically the influence of the cavity structure on the output characteristics of microwave emitted from axially extracted virtual cathode oscillator. By installing the cavity in the virtual cathode oscillator, the microwave with the resonant frequency is enhanced, whereas nonresonant frequencies are suppressed and the bandwidth of the emitted microwave becomes sharp. In addition, the output microwave power increased by 15% to 80 MW. The dominant emission mode from the virtual cathode oscillator is found to be mainly TM mode by the resonance condition of cavity and simulation results. We plan to find a practical way of improving its frequency characteristics and microwave efficiency.

References

[1] R. J. Barker and E. Schamiloglu, Eds., "High-Power Microwave Sources and Technologies", New York: Wiley-IEEE Press (2001).

[2] J. Benford, J. Swegle, and E. Schamiloglu, "High Power Microwaves" 2nd ed., New York: Taylor & Francis (2007.

[3] D. J. Sullivan, J. E. Walsh, and E. A. Coutsias, "Virtual cathode oscillator (vircator) theory", in High Power Microwave Sources, V. Granastein and I. Alexeff, Eds. Norwood, MA: Artech House, p. 441 (1987).

[4] B. V. Alyokhin, et al., "Theoretical and experimental studies of virtual cathode microwave devices", IEEE Trans. Plasma Sci., vol.22, pp.945–959 (1994).

[5] E. H. Choi, et al., "High-power microwave generation from an axially extracted virtual cathode oscillator", IEEE Trans. Plasma Sci., vol.28, pp.2128–2134 (2000).

[6] W. Jeon, et al., "Output characteristics of the high-power microwave generated from a coaxial vircator with a bar reflector in a drift region", IEEE Trans. Plasma Sci., vol.34, pp.937-944 (2006).

[7] D. Biswas and R. Kumar, "Efficiency Enhancement of the Axial VIRCATOR", IEEE Trans. Plasma Sci., vol.35, pp.369-378 (2007).

[8] R. Menon, et al., "High power microwave generation from coaxial virtual cathode oscillator using graphite and velvet cathodes", J. Appl. Phys. vol.107, p.093301 (2010).

[9] J. Benford, et al., "Interaction of a vircator microwave generator with an enclosing resonant cavity," J. Appl. Phys., vol. 61, pp. 2098–2100 (1987).

[10] W. Jiang, et al., "Experimental and simulation studies of new configuration of virtual cathode oscillator," IEEE Trans. Plasma Sci., vol. 32, pp. 54–59 (2004).

[11] W. Jiang, "Time–Frequency Analysis of Virtual-Cathode Oscillator", IEEE Trans. Plasma Sci., vol.38, pp.1325-1328 (2010).

[13] H. Sze, et al., "Dynamics of a virtual cathode oscillator driven by a pinched diode", Phys. Fluids, vol.29, pp.3873-3880 (1986).

Behavior of Electron Beam in Virtual Cathode Oscillator

Tomoya Ito, Tatsuro Ohka, Taichi Sugai, Weihua Jiang

Nagaoka University of Technology

ABSTRACT

Research for the generation of high power microwave, Virtual cathode oscillator (Vircator) operated by "ETIGO-Ⅳ" has been studied. The purpose of this study was to elucidate the microwave generation mechanism in the Vircator. A shunt for measuring the downstream electron beam in the Vircator was fabricated. Behavior of the electron beam when oscillating was confirmed by measuring the electron beam current in the beam traveling direction. The microwave was generated 30 ns after the rise of the upstream current. At that time, it was confirmed experimentally that the electrons in the downstream electron beam were reflected and decreased by the virtual cathode.

Keywords

Virtual Cathode Oscillator, Vircator, High Power Microwave, Electron Beam, Pulse Power

1 Introduction

High Power Microwave (HPM) is an electromagnetic wave having a frequency of 1 to 30 GHz and exceeds 100 MW. It is expected to be applied to accelerators and wireless power transmission. The Virtual Cathode Oscillator (Vircator) has the advantage that external magnetic field is unnecessary, the structure is simple, and frequency can be adjusted. However, the conversion efficiency is low, and the oscillation mechanism is unclear. [1] In this study, to elucidate the oscillation mechanism of the Vircator quantitatively, we fabricated a measuring instrument that measured the electron beam current and investigated the relation between the electron beam and the microwave.

2 Experimental Setup

2.1 Electron beam shunt

Fig.1 and Fig.2 show the appearance and equivalent circuit of a shunt for measuring electron beam current. The shunt had an electron beam collector with a diameter of 24 cm at the tip. The collector was fixed with four screw pipes. Shunt resistances (metallic film resistance, 2 Ω) were arranged in parallel in the concentric circle at the base. It was insulated by placing acrylic board (2 mm) between the screw pipe fixing part and the flange which was the ground potential. It was possible to measure the electron beam current by measuring the potential generated when the electron beam passed through the shunt resistor.

The electron beam current is given by

$$I_b = \frac{V_{out}}{50} + \frac{V_{out}}{R_{//}}. \qquad (1)$$

Here, the terminating resistance of the oscilloscope is 50 Ω, the measurement voltage is V_{out}, and the combined resistance of the shunt resistance is $R_{//}$.

2.2 Pulsed power generator "ETIGO-Ⅳ"

In this study, the virtual cathodic oscillator was driven by the repetitive pulsed-power generator "ETIGO - IV". (Fig. 3) Rated voltage 400 kV, rated current 13 kA, pulse width 120 ns, repetition rate 1 Hz. [2] The cathode was bonded with a 10 cm diameter velvet with epoxy adhesive on a 12 cm diameter stainless steel disk. For the anode, a stainless-steel mesh (transmittance of about 65.8%) cut into a circle and fixed by a ring-shaped fixture was used. The anode-cathode gap

was 21 mm. The voltage between the electrodes and the upstream electron beam of the anode were measured by the capacitive voltage divider and Rogowski coil of the "ETIGO - IV" main body. The current which was measured by shunt was the downstream electron beam. Each signal was observed on an oscilloscope (Lecroy WavePro 760 Zi) through a coaxial cable. When observing microwaves, change the shunt to a circular waveguide (21 cm in diameter, 1 m in length) with an acrylic window at the tip. The generated microwave was received by a horn antenna (band 1.72 - 2.61 GHz) located 2.5 m away from the output window and observed with an oscilloscope via a high frequency cable (TOTOKU, TCF 500) and a detector (Anritsu 75 N 50 B). The horn antenna was installed at a position of 20 ° when the front face of the waveguide was set to 0 °.

3 Experimental Results

3.1 Measurement of current distribution in beam progression direction

Fig.4 shows the waveform of the shunt when the anode-collector gap was discretely varied from 10 mm to 100 mm. Fig.5 shows the maximum current value (average of absolute values in "ETIGO - IV" 3 shots) in each anode - collector gap. When the anode-collector gap was 70 mm in Fig. 4, the current rapidly decreases, it was considered that the virtual cathode is formed, which suggests that electrons are reflected. [3] In Fig.5, the current didn't change between 10 mm and 40 mm. This was because when the anode mesh and the collector were regarded as a parallel flat plate of the same potential, the virtual cathode wasn't formed at the position which was theoretically shorter than twice the distance between the electrodes. Current reduction was seen at 50 mm and 60 mm. This was because part of the beam didn't strike the collector due to divergence of the electron beam due to the self-electric field.

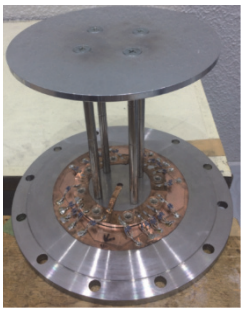

Fig.1 Electron beam shunt

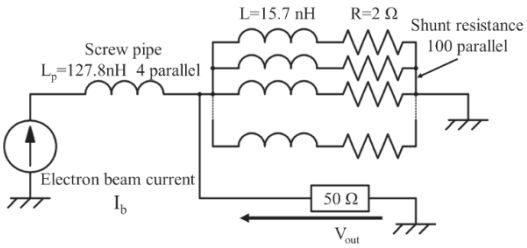

Fig.2 Equivalent circuit of electron beam shunt.

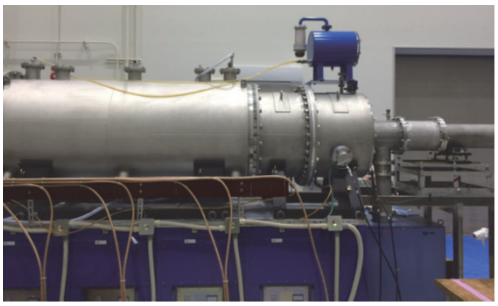

Fig.3 Repetitive pulsed-power generator "ETIGO-IV".

3.2 Relationship between electron beam and microwave

Fig.6 shows a combination of upstream and downstream current waveforms when a planar collector is placed at an anode-collector gap of 70 mm and microwave power waveform. From the graph, the microwave rose about 30 ns after the rising of the current. That is, a virtual cathode was formed. The electron beam current on the downstream side decreased with the generation of the microwave because electrons were reflected

due to the formation of the virtual cathode. The current downstream of the subsequent electron beam was limited by the virtual cathode.

4 Conclusion

In this study, we fabricated a shunt to measure the electron beam current for elucidating the oscillation mechanism of the virtual cathode oscillator. In the current distribution with respect to the beam traveling direction, when the collector position was set at 70 mm or more, the formation of the virtual cathode was confirmed. From the temporal relationship between the electron beam and the microwave, the microwave rose about 30 ns after the rising of the current. Since electrons were reflected by the formation of the virtual cathode, the downstream electron beam decreased and was then limited.

In the future, we will investigate details on the conversion of energy from electron beam energy to microwave.

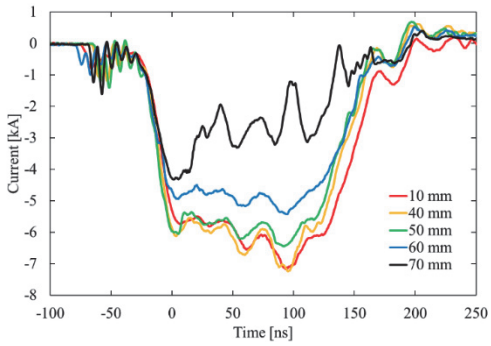

Fig.4 Waveform of downstream to beam progression direction.

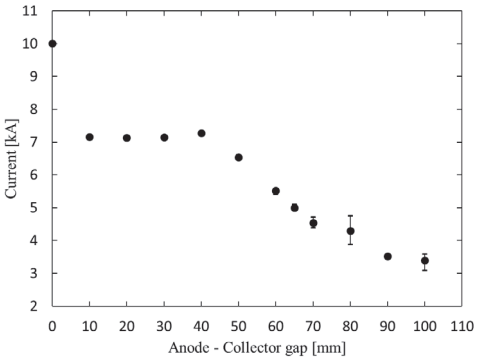

Fig.5 The current distribution to beam progression direction.

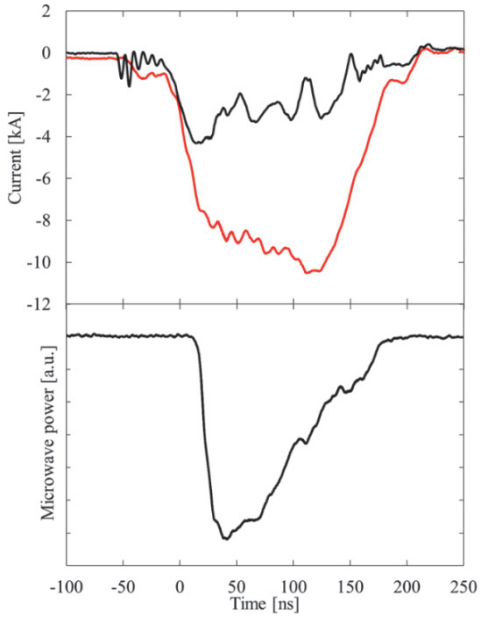

Fig.6 Time relationship between electron beam and microwave. (Top: Upstream and downstream current. Bottom: Microwave.)

Reference

[1] W.Jiang, "Time-Frequency Analysis of Virtual-Cathode Oscillator", IEEE Trans. Plasma Science, Vol.38, N0.6 1325-1328(2010)

[2] A.Tokuchi , N.Ninomiya , W.Jiang , K.Yatsui , "Repetitive Pulsed-Power Generator "ETIGO-Ⅳ"" , IEEE Trans. Plasma Science, Vol 30 , No.5 , 1637-1641(2002)

[3] M.Onoi , M.Yamabuchi , M.Yatsuzuka , "金属メッシュ陽極による仮想陰極発振器の出力改善と多ショット化" , IEEJ Trans. FM, Vol. 123, No.1(2003)

Effect of Resonant Cavity in Virtual Cathodic Oscillator

Tatsuro Ohka, Tomoya Ito, Muhammad Shafiq Bin Zakaria,
Taichi Sugai, and Weihua Jiang

Extreme Energy-Density Research Institute, Nagaoka University of Technology

ABSTRACT

The virtual-cathode oscillator is one of the promising devices being developed as high-power microwave sources. It has the advantages of simplicity and high power capability. However, it has serious problems like low efficiency and frequency stability. In this paper, we have tried to solve those problems by installing a resonator and strengthening microwave interactions. Therefore, microwave measurements of a virtual cathode oscillator with a resonator has been carried out. The measurement result shows that the output of the virtual cathode oscillator can be improved by installing the resonator designed to match the resonant frequency and the oscillation frequency.

Keywords

Virtual Cathode Oscillator, Vircator, High Power Microwave, Pulse Power

1 Introduction

A high power microwave (HPM) is an electromagnetic wave whose wave length 1 – 30 cm (frequency is 30 – 1 GHz) and HPM exceeds 100 MW in peak power. In recent years, HPM had various applications in charged particle accelerators, plasma heating, medical field, space development field, and many other fields. Virtual cathode oscillator (Vircator) is one of the sources of HPM. [1][2] A vircator is capable of generating pulsed microwaves with the peak power ranging from a few tens of MW up to several GW. It design is simple and Generated frequency range is on the order of GHz. However, vircator has serious problems like low efficiency and frequency stability. [3] The purpose of this study is to improve the microwave efficiency of the vircator by installing a resonator. In this paper deals the result of comparing and examining the radiation power and frequency characteristics of the case where the resonator is installed and the conventional vircator.

2 Principle and Experimental Setup

2.1 Principle of Virtual Cathode Oscillator

Figure 1 shows the schematic structure of the vircator used in this paper. The cathode is a planar stainless steel disk covered with a piece of velvet of 12 cm in diameter, and the anode is a stainless-steel mesh with a transparency of ~ 65%(Wire diameter:0.6mm). The anode–cathode gap is 21 mm. When a pulsed high voltage is applied on the diode, an electron beam is generated from the cathode surface and accelerated toward the anode. Part of the electron beam passes through the anode and forms a virtual cathode that oscillates and radiates electromagnetic waves in the microwave range. The radiation is extracted through a cylindrical waveguide of 21 cm in diameter and 100 cm in length and is emitted into the air through an acrylic window.

2.2 Repetitive pulsed-power generator ETIGO-IV

Figure 2 shows the repetitive pulsed power generator “ETIGO-IV” has been used to drive the

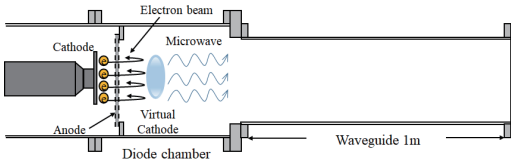

Fig. 1 Schematic structure of a virtual cathode oscillator.

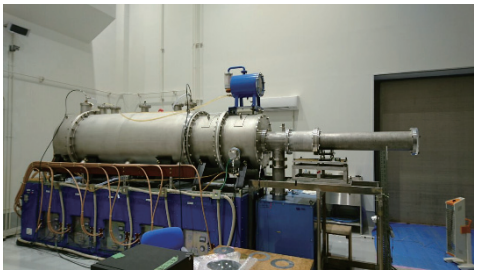

Fig. 2 Repetitive pulsed-power generator "ETIGO-IV".

vircator, which has rated outputs of 400 kV in voltage, 13 kA in current, 150 ns in pulse width, and 1 Hz in repetition rate. [4]

Figure 3 shows the typical experimental result of a vircator using ETIGO-IV. For observation of microwaves, a horn antenna (R-band: 1.72 - 2.61 GHz) was used and measured with a digital oscilloscope (LeCroy Wave Pro 760 Zi, with a sampling rate of 40 GS / s) through a coaxial RF cable (TOTOKU TCF 500). At the same time, the microwave peak power was calculated by mV-dBm conversion by measuring the microwave by a microwave detector (Anritsu 75N 50 B).

The peak voltage shown in Fig. 3 reaches ~300 kV with a peak current of ~10 kA. Although the microwave radiation has been observed, its peak power is ~60 MW, giving a microwave efficiency is ~1.9%. Figure 4 shows the Fourier transform of the horn antenna signals shown in Fig. 3. From Fig. 4, the main microwave frequency of the vircator using ETIGO-IV is ~2.5GHz.

2.3 Installation of resonator

Installation of a resonator has been proposed to improve the oscillation efficiency of the virtual cathode oscillator. [5][6] In this study, a resonator is

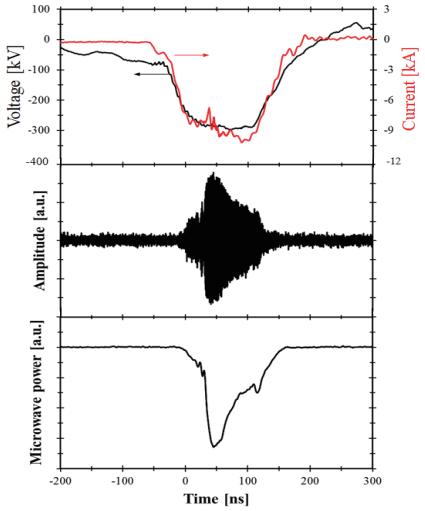

Fig. 3 Waveform of diode voltage and current, R-band horn antenna signal, and waveform of obtained by microwave detector.

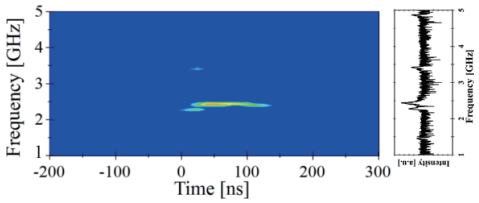

Fig. 4 Time-Frequency analysis (TFA) and Fourier transform of the horn antenna signal shown in Figure 3.

constructed by attaching an electromagnetic wave reflection plate to one end of a metal cylinder. Figure 5 shows the principle diagram when a resonator is installed in the vircator. It is expected that the microwave efficiency will be improved by the interaction between the oscillated microwave and the microwave reflected by the resonator. In this paper, several resonators with resonance frequency around 2.5 GHz were prepared and experiments were carried out. Figure 6 shows the resonator using this paper.

3 Experimental results

3.1 Change the length of resonator *L*

Figure 7 shows the microwave peak power when changing the length of the resonator to 60 to 95 mm. The horizontal axis is the length of the resonator

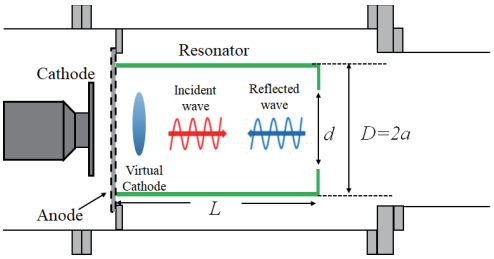

Fig. 5 Schematic structure of a virtual-cathode oscillator with resonant cavity.

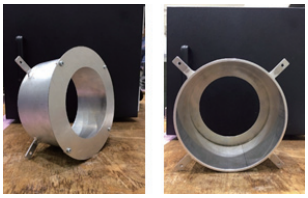

Fig. 6 Resonator (L=80mm, D=144mm, d=110mm).

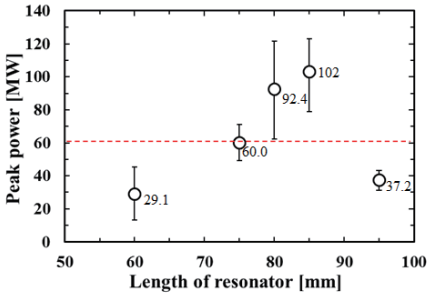

Fig. 7 Length of resonator vs peak power characteristic (D=144, d=110mm).

L [mm], and the vertical axis is the radiation power [MW]. The plot is the average value of the microwave peak power when the measurement was carried out 5 times under each condition, and the error bar shows the maximum value and the minimum value. The red line on the graph shows the microwave power without the resonator. From Fig. 7, at the resonator length of 80 and 85 mm, the peak power is larger than when without the resonator. This results shows the properly designed resonator can improve the microwave efficiency of the vircator. Fig.8 shows the R-band horn antenna signal and TFA result under condition of resonator length is 80mm. Compared to Fig. 3 and Fig.4, when the efficiency improves as shown in Fig. 8, it

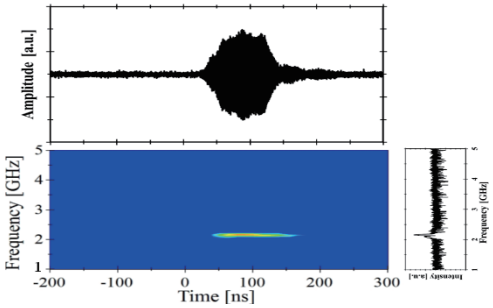

Fig. 8 Microwave and TFA results obtained by using resonator. (L=80mm, D=144mm, d=110mm)

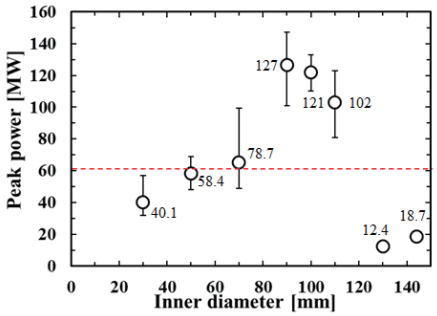

Fig. 9 Inner diameter of resonator vs peak power characteristic (L=60mm, D=144mm).

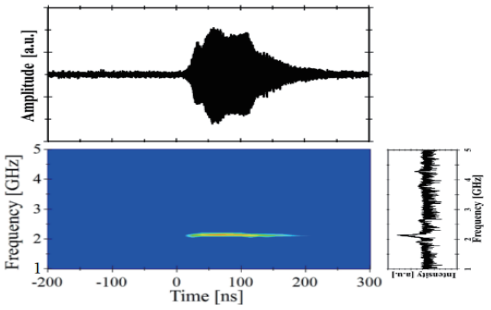

Fig. 10 Microwave and TFA results obtained by using resonator. (L=85mm, D=144mm, d=90mm)

oscillates at a single frequency and the amplitude of the microwave also tends to be constant.

3.2 Change the inner diameter of resonator *d*

From the results in Fig. 7, larger peak power can be expected with the resonator length L = 85 mm. Therefore, in Fig. 7, the inner diameter of resonator d was fixed at 110 mm, but we investigated whether further improvement in microwave power

can be made by changing the inner diameter of resonator. Figure 9 shows the microwave peak power when changing the inner diameter of resonator to 30 to 144 mm. The horizontal axis is the inner diameter of resonator *d* [mm], and the vertical axis is the radiation power [MW]. It can be seen that the peak power greatly changes depending on the difference in inner diameter of resonator. Especially when the inner diameter of the resonator is 90 mm, approximately twice the peak power was obtained than in the case without the resonator. Figure 10 shows the R-band horn antenna signal and TFA result under condition of resonator length is 85mm, inner diameter is 90mm. From Fig.10, the measured microwave tendency also coincided with Fig.8.

4 Conclusion

Improvement of peak power and microwave efficiency of the virtual cathode oscillator is possible by installing a resonator and strengthening microwave interaction. In this study, we have improved the peak power and microwave efficiency of the virtual cathode oscillator by about 2 times by using a resonator with a length of 85 mm and an inner diameter of 90 mm. In the future we will optimize the resonator structure and aim to further improve the efficiency of the virtual cathode oscillator.

Reference

[1] D.J.Sullivan, J.E.Walsh, and E.A.Coutsias: "Virtual cathode oscillator (vircator) theory," *High Power Microwave Sources*, V.Granatstein and I.Alexeff,Eds. Norwood, MA:Artech House, pp.441-505 (1987).

[2] L.E.Thode,"Virtual-cathode microwave device research: Experiment and simuation," High Power Sources, V.Granatstein and I.Alexeff,Eds. Norwood, MA:Artech House, pp.507-562(1987).

[3] W. Jiang, "Time-frequency analysis of virtual cathode oscillator," *IEEE Trans. Plasma Sci.*, vol. 38, No.6, pp.1325-1328, Jun.2010.

[4] A. Tokuchi, N. Ninomiya, W. Jiang, and K. Yatsui, "Repetitive pulsed-power generator 'ETIGO-IV'," *IEEE Trans. Plasma Sci.*, vol. 30, No. 5, pp. 1637–1641, Oct. 2002.

[5] J. Benford, D. Prise, H, Sze, and D. Bromley, "Interaction of a vircator microwave generator with an enclosing resonant cavity," *Journal of Applied Physics.*, vol.61, 2098(1987).

[6] V. Baryshevsky, A. Gurinovich, E. Gurnevich, and P. Molchanov, "Experimental study of an axial vircator with resonant cavity," *IEEE Trans. Plasma Sci.*, vol. 43, No.10, pp3507-3511, Oct.2015.

Kinetic Energy Partitioning Between Longitudinal and Transverse Directions of Beam using Compact Electron Beam Simulator for Final Pulse Compression in Heavy–Ion Inertial Fusion

Takashi Kikuchi, Takuya Komori, Ryuma Matsuda, Youngsoo Park*, Yasuo Sakai**, Yukihiro Soga*, Kazuhiko Horioka**, Kazumasa Takahashi, Toru Sasaki, Nob. Harada

Nagaoka University of Technology
**Kanazawa University*
***Tokyo Institute of Technology*

ABSTRACT

Kinetic energy partitioning between longitudinal and transverse directions of beam bunch was studied for longitudinal pulse compression during final stage of energy driver in heavy–ion inertial fusion. Beam parameters were corresponded with experimental parameters of compact electron beam simulator. The kinetic energy equipartition was estimated by the multi–particle simulation results. It was expected that the equipartition in a theoretical approach is underestimated in comparison to the numerical simulation result.

Keywords

Heavy–Ion Inertial Fusion, Space–Charge–Dominated Beam, Space Charge Effect, Pulse Compression, Equipartitioning, Compact Beam Simulator

1 Introduction

In an energy driver of heavy ion inertial fusion, beam dynamics in a longitudinal pulse compression is an important issue for an effective implosion process of a fuel pellet [1]. A large scale of a particle accelerator complex is required to generate intense heavy–ion beams. However it is not suitable for the researches of the beam dynamics from the viewpoint of the cost. For this reason, theoretical and numerical approaches were carried out [2–8], moreover an experimental device by using electron beam was proposed for a scaled simulator [9–12]. It is easy to achieve the space–charge–dominated state in a small experimental device.

The equipartitioning of the longitudinal and the transverse temperatures of the beam is expected in the space–charge–dominated condition [13], and is important topic for the beam dynamics and transport [14, 15]. In this study, the kinetic energy partitioning between the longitudinal and the transverse directions of the beam is discussed with the evolution of the kinetic energies in the compact beam simulator.

2 Calculation Conditions

The numerical simulation is carried out using multi–particle tracking with space charge effect. The calculation box for the numerical simulation and the detail of the calculation conditions are described in Refs. [16–18]. The transverse confinement of the beam is carried out with the pulse solenoidal magnet. The magnetic flux density B_z for longitudinal direction z is given with 11 mT corresponding to the experimental condition. The velocity modulation pulse duration applied by the induction unit

is 100 ns. The injected kinetic energy of electrons is 2.8 keV, and the initial pulse duration is 100 ns. After the initial setting, the beam bunch is injected into the modulation gap. The applied voltage $V_{\rm dec}$ is geven by

$$V_{\rm dec} = \frac{m_{\rm e}}{2e} \frac{1}{\left(\sqrt{\frac{m_{\rm e}}{2eV_0}} + \frac{\tau_{\rm p} - t}{L} \right)^2} - V_0, \quad (1)$$

where $m_{\rm e}$ is the mass of electron, e is the charge of electron, V_0 =2.8 kV, $\tau_{\rm p}$ =100 ns is the pulse duration, t is the time, and L=1.93 m is the drift length for transport. To apply the modulation voltage into the gap, the longitudinal velocity distribution of injected electrons has the head-to-tail velocity tilt. For this reason, the pulse duration of electron bunch is compressed in order to the velocity tilt during the drift transport after the gap.

In the experimental condition, the electron gun emits the electrons, and the electrons accelerate longitudinally to 2.8 keV in quasi-DC mode after the electron emission from the thermal cathode surface. In this study, the initial transverse and longitudinal temperatures are assumed by $T_\perp = T_{||} = 1000$ K, and the temperatures give the velocity spread to the initial particle distribution. For this reason, the longitudinal velocity of particle has the average velocity for injection kinetic energy of 2.8 keV with the thermal velocity spread of 1000 K. The condition is an ideal case starting with the equal temperatures. The initial beam current is -265 μA.

3 Simulation Result

It was found that the longitudinal kinetic energy of the beam particle was converted into the transverse kinetic energy due to the space charge effect [18]. The effective transverse and longitudinal temperatures are evaluated by

$$T_\perp = \frac{m_{\rm e}\langle v_\perp^2 \rangle}{2} = m_{\rm e} \frac{\langle (v_{\rm x} - \langle v_{\rm x} \rangle)^2 \rangle + \langle (v_{\rm y} - \langle v_{\rm y} \rangle)^2 \rangle}{4}, \quad (2)$$

and

$$T_{||} = \frac{m_{\rm e}\langle v_{||}^2 \rangle}{2} = m_{\rm e} \frac{\langle (v_{\rm z} - \langle v_{\rm z} \rangle)^2 \rangle}{2}. \quad (3)$$

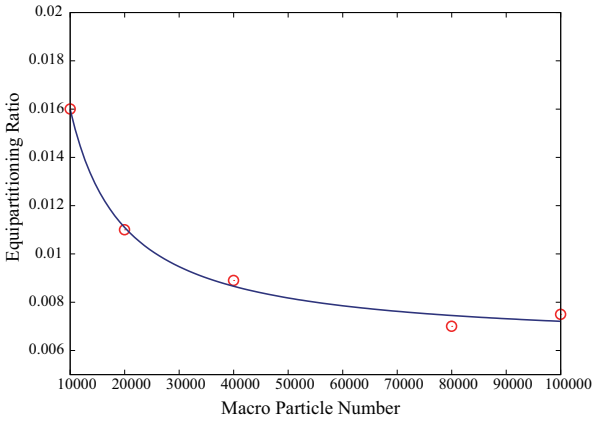

Figure 1: Equipartitioning ratio $T_\perp/T_{||}$ as a function of macro (super) particle number $N_{\rm sp}$. The red circle indicates the numerical simulation result, and the solid line indicates the fitting curve of $f(N_{\rm sp}) = 103.78\, N_{\rm sp}^{-1.00695} + 0.00625084$.

Here, $m_{\rm e}$ is the mass of electron, $v_\perp$ and $v_{||}$ are the transverse and longitudinal velocities of particle on the beam frame, and $v_{\rm x}$, $v_{\rm y}$, and $v_{\rm z}$ are the particle velocities in x, y, and z directions on the laboratory frame, respectively. The value $\langle X \rangle$ indicated with brackets means the average value of X. The equipartitioning ratio $T_\perp/T_{||}$ is obtained by the ratio of Eq.(2) to Eq.(3).

Figure 1 show the equipatitioning ratio at t = 160 nsec (i.e., the maximum compression time) as a function of the number of macro (super) particles used for the numerical simulation. By using the least–square approach, the numerical simulation results are fitted by

$$f(N_{\rm sp}) = 103.78\, N_{\rm sp}^{-1.00695} + 0.00625084, \quad (4)$$

where $N_{\rm sp}$ is the macro (super) particle number. From Eq. (4), it is expected that the equipartitioning ratio converges on 0.00625084 for $N_{\rm sp} = \infty$.

On the other hand, the theoretical estimation for the equipartitioning ratio indicated as 0.00285 [18]. It is implied that the theoretical result underestimates the kinetic energy equipartition between the longitudinal and the transverse directions.

4 Conclusion

The kinetic energy partitioning between the longitudinal and the transverse directions of the beam was investigated numerically for the longitudinal

pulse compression during the final stage of the energy driver in heavy–ion inertial fusion. The beam parameters were corresponded with the experimental parameters of the compact electron beam simulator. The equipartitioning ratio $T_{\perp}/T_{||}$ was estimated as 0.00625084 in the multi–particle simulation results. It was expected that the equipartitioning in the theoretical approach was underestimated in comparisons to one of the numerical simulation.

References

[1] S. ATZENI and J. MEYER-TER-VEHN, *The Physics of Inertial Fusion: Beam Plasma Interaction, Hydrodynamics, Hot Dense Matter* (Oxford Univ., N.Y., 2004).

[2] D. D.-M. HO and S. T. BRANDON, *Nucl. Instrum. Methods Phys. Res.*, **A278**, pp.182-185 (1989).

[3] O. BOINE-FRANKENHEIM, I. HOFMANN and G. RUMOLO, *Phys. Rev. Lett.*, **82**, 3256 (1999)

[4] M.J.L. DE HOON, E.P. LEE, J.J. BARNARD and A. FRIEDMAN, *Phys. Plasmas*, **10**, pp.855-861 (2003).

[5] R.C. DAVIDSON and E.A. STARTSEV, *Phys. Rev. ST Accel. Beams*, **7**, 024401 (2004)

[6] T. KIKUCHI, M. NAKAJIMA, K. HORIOKA and T. KATAYAMA, *Phys. Rev. ST Accel. Beams*, **7**, 034201 (2004)

[7] T. KIKUCHI and K. HORIOKA, *Nuclear Instruments and Methods in Physics Research*, **A 606**, pp.31-36 (2009)

[8] P.S. BABU, A. GOSWAMI and V.S. PANDIT, *Phys. Lett.*, **A 378**, pp.212-218 (2014).

[9] P.G. O'SHEA, M. REISER, R.A. KISHEK, S. BERNAL, H. LI, M. PRUESSNER, V. YUN, Y. CUI, W. ZHANG, Y. ZOU, T. GODLOVE, D. KEHNE, P. HALDEMANN and I. HABER, *Nucl. Instrum. Methods Phys. Res.*, **A464**, pp.646-652 (2001).

[10] A. NAKAYAMA, Y. SAKAI, Y. MIYAZAKI, T. KIKUCHI, M. NAKAJIMA and K. HORIOKA, *EPJ Web Conf.*, **59**, 09005 (2013).

[11] Y. SAKAI, M. NAKAJIMA, J. HASEGAWA, T. KIKUCHI and K. HORIOKA, *Nucl. Instrum. Methods Phys. Res.*, **A733**, pp.70-74 (2014).

[12] Y. PARK, Y. SOGA, Y. MIHARA, M. TAKEDA and K. KAMADA, *NIFS-PROC*, **93**, pp.84-87 (2013).

[13] R.A. JAMESON, *IEEE Trans. Nucl. Sci.*, **NS-28**, 2408 (1981).

[14] T.P. WANGLER, *RF Linear Accelerators, 2nd Edition*, (Wiley-VCH : Verlag GmbH & Co. KGaA, 2008).

[15] M. REISER, *Theory and Design of Charged Particle Beams* (Wiley, New York, 1994).

[16] T. KIKUCHI, K. HORIOKA, K. TAKAHASHI, T. SASAKI, T. ASO and Nob. HARADA, *Progress in Nuclear Energy*, **82**, pp.126-129 (2015).

[17] T. KIKUCHI, Y. SAKAI, T. KOMORI, T. SATO, J. HASEGAWA, K. HORIOKA, K. TAKAHASHI, T. SASAKI and Nob. HARADA, *Journal of Physics: Conference Series*, **717**, 012101 (2016).

[18] T. KIKUCHI, Y. SAKAI, J. HASEGAWA, K. HORIOKA, K. TAKAHASHI, T. SASAKI and Nob. HARADA, *IEEE Transactions on Plasma Science*, **44**, pp.216-220 (2016).

Energy Transport of Axially Compressed Electron Plasma Simulating Space-charge Dominated Beam

Youngsoo Park, Yukihiro Soga, and Takashi Kikuchi*

Graduate School of Natural Science and Technology, Kanazawa University, Kakuma-machi, Kanazawa, Ishikawa, 920-1192, Japan

**Nagaoka University of Technology, Nagaoka, 940-2188, Japan*

ABSTRACT

The axial energy distribution and the radial mean energy of a pure electron plasma confined in a Malmberg-Penning trap have been measured during and after the longitudinal compression. The mean energy in the both directions increases during the compression due to the increase of the space charge effects. After the compression, the axial energy is converted into the radial energy, while the total energy is almost kept constant. Such precise measurements of the fast energy relaxation of compressed electron plasmas could contribute to the technical development of generating the space-charge-dominated heavy ion beam with low emittance required for a heavy ion inertial fusion.

Keywords

Electron plasma, Space-charge-dominated beams, Heavy ion inertial fusion

1. Introduction

In a heavy ion inertial fusion device, heavy ion beams (HIB) with extremely high current should be prepared for the efficient implosion of a target. In order to realize a large amount of the current, an abrupt longitudinal compression of the HIB is required in the final stage of the device[1]. The sudden increase of the current density generates a high space charge effect which causes an increase of the beam emittance. In a result, the efficient fusion reaction would be prevented. A method for controlling the increase of beam emittance after the dramatic compression has to be studied. However, the study on the HIB in a large accelerator complex will cost a great expense.

Instead of HIB, an electron plasma in a Malmberg-Penning trap is a suitable material for the study on charged particle beam. The equivalence has been confirmed of the pure electron plasma and the charged particle beam in the center-of-mass frame under a proper scale transformation[2]. The compression in the longitudinal direction of HIB could be simulated by the compression in the longitudinal direction of the pure electron plasma. The observed energy distribution in of the pure electron plasma could be related to the beam emittance of the HIB.

According to the preliminary experiment using a Malmberg-Penning trap, an increase of the electron temperature in the axial direction was observed during the axial compression of a pure electron plasma[3]. However, the time evolution of the radial energy has not been measured during the compression. In this study, in addition to the axial energy, the radial energy of the pure electron plasma was observed during and after the axial compression in order to clear the fast relaxation process from non-equilibrium state due to the compression.

2. Experimental Setup

The schematic configuration of the compression experiment device is shown in Fig.1. The device is composed of an electron source, ring electrodes with 60 mm in a diameter, and a phosphor screen in a

cylindrical vessel. The basic scheme of an electron confinement consists of the homogeneous magnetic field along the z-axis and the saddle shaped axisymmetric potential with negative barriers at both ends[4]. We use an electron plasma of cylinder in shape with an equilibrium state as an initial profile for the compression experiment. The cylindrical electron plasma is produced by mixing and relaxation of about 500 strings of electrons which accumulate in the trap through multiple injection-hold-mixing cycles.

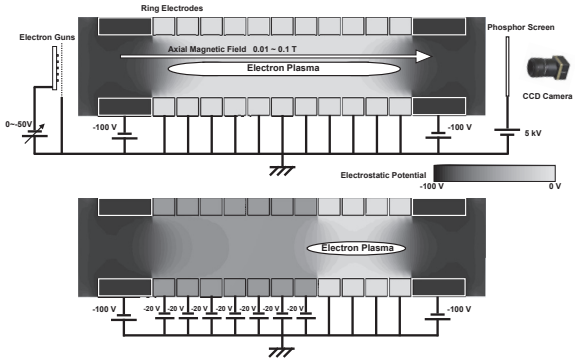

Fig. 1 Schematic configuration of the electron trap. Electrons are compressed in the longitudinal direction by changing the external electric potential.

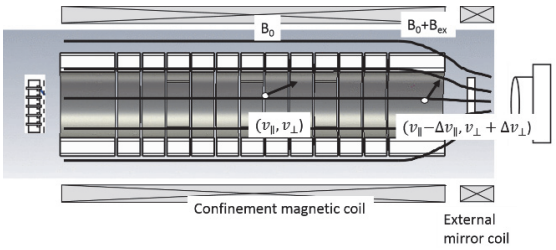

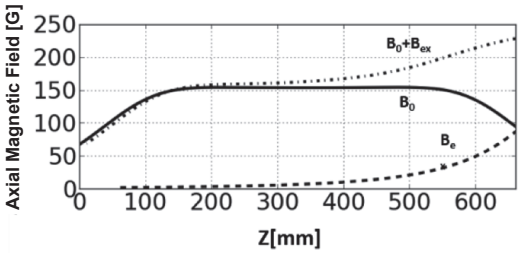

Fig. 2 2D magnetic field distribution for the energy analysis in the radial direction (upper figure). An auxiliary magnetic field is added where the analyzing potential is applied for selection of energetic electrons. The energy selection is carried out at z = 500 mm (lower figure).

The axial compression is achieved by applying negative voltage to seven ring electrodes where the electrons originally exists. In this experiment, an electron column is compressed from 0.120 m to 0.030 m in the axial length for 1.5 msec.

A longitudinal kinetic energy distribution of plasmas is measured by the energy selection method using variable potential at the end electrode[5]. A radial kinetic energy can be measured by magnetic mirror field added at the energy selection region shown in Fig.2. The axial kinetic energy is converted to the radial one due to the mirror field, so the average radial kinetic energy could be determined [6].

3. Experimental Results

Figure 3 represents radial distribution of electron densities and longitudinal temperatures of the electron plasma with the 1/e radius of 11 mm under the magnetic field B = 0.1 T(a) and 0.02 T(c) before and after the compression. The electron plasmas are compressed from the axial length L = 0.12 m to 0.03 m by shortening the ground region for 1.5 msec. The radial density distribution almost remains unchanged by the compression. On the other hand, the longitudinal electron temperature increases over the whole region in both cases. The mean increase rates of the axial temperature before and after the compression are 0.38 with B = 0.1 T and 0.21 with B = 0.02 T respectively.

The time evolution of the electron temperature in the axial and radial directions defined by the mean energy is plotted in Fig. 4. During the axial compression for 1.5 msec, the temperature in the both directions increases rapidly. Because the time scale of Coulomb collisions in this parameter range is few msec, the increase of the radial energy could be driven by a space charge effect. After the compression, the axial energy is slowly converted into the radial energy probably due to the Coulomb collision, while the total energy is almost kept constant.

4. Discussion

In beam dynamics, a tune depression is used as an index to the space charge effect of charged particle

beam. For non-neutral plasmas with low density in comparison to the Brillouin density limit, the tune depression can be determined as follows [7].

$$\sigma/\sigma_0 = \sqrt{1 - \frac{n_0/n\,(0)}{(1+\Delta)}}$$

$$\Delta \equiv \frac{2(\omega_r\omega_c - {\omega_r}^2)}{{\omega_p}^2} \approx \frac{2\tilde{n}}{n_0} - 1$$

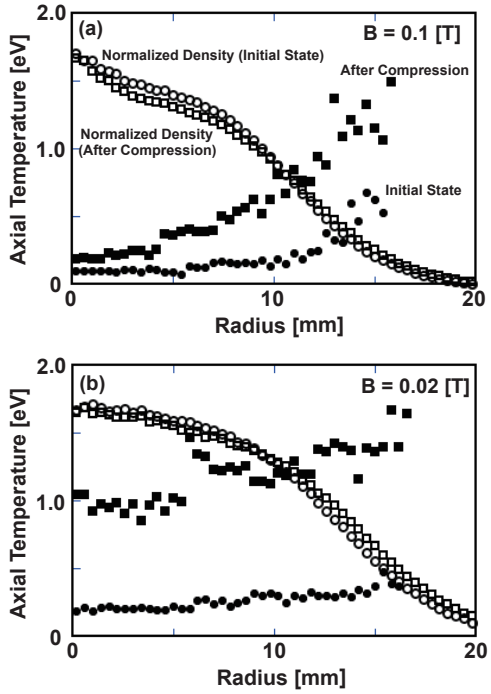

Fig. 3 Radial density distribution of electron plasmas before and after the longitudinal compression for magnetic field B = 0.1 T (a) and 0.02 T (b) along with the longitudinal kinetic energy distribution.

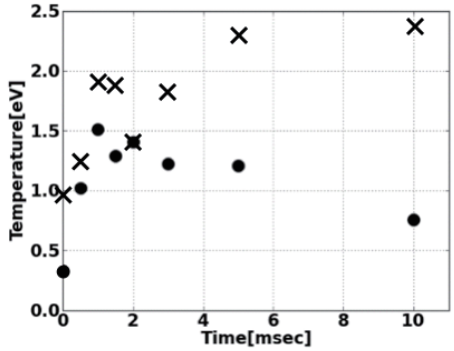

Fig. 4 The time evolution of electron temperature in the axial direction (closed circles) and radial direction (crosses). The electron plasma was compressed from t = 0 to 1.5 msec.

Here n_0 is a constant density determined by the total electron number and RMS radius, ω_r is a plasma rotation frequency in the cross section, and $\tilde{n}$ is a average density bounded by the RMS radius. According to the radial density distribution, the tune depression could be estimated at 0.76 with B = 0.1 T, 0.67 with B = 0.02 T respectively. On the other hand, the average rise rate of the axial temperature before and after the compression can be calculated at 3.2 with 0.1 T and 4.6 with 0.02 T. This results suggest that beam emittance increases due to the larger space charge with the weaker magnetic field. However, the tune depression 0.67 is still large in terms of beam physics. In order to investigate the high current ion beam, electron plasmas with flat density distribution or with the Brillouin density under the weak magnetic field are required.

5. Conclusion

An energy increase and relaxation due to a space charge effect were observed in an axially compressed pure electron plasma. The electron temperature in the radial and axial direction increased by compressing the electron plasma into one forth in the axial length. The average rise rate of the axial temperature before and after the compression was higher in a weaker magnetic field. After the compression, the axial energy is slowly converted into the radial energy, while the total energy is almost kept constant.

References

[1] T. Kikuchi et al., Nucl. Instr. Meth. Phys. Res. A577, 103 (2007)

[2] H. Okamoto, H. Tanaka, Nucl. Instr. Meth. Phys. Res. A **437**, pp.178-187(1999).

[3] Youngsoo Park, Yukihiro Soga, and Takashi Kikuchi, "Experimental study on the axial compression of a pure electron plasma simulating space-charge-dominated beam", to be published in NIFS-PROC Series.

[4] Y. Soga, T. Mimura, Y. Kato and Y. Park, Plasma Fusion Res. **8**, 2401034 (2013).

[5] D. L. Eggleston, C. F. Driscoll et al., Phys. Fluids B **4** 3432 (1992).

[6] A. W. Hyatt, C. F. Driscoll, and J. H. Malmberg, Phys. Rev. Lett. 59, 2975 (1987).

[7] Steven M. Lund, T. Kikuchi, and Ronald C. Davidon, Phys. Rev. Accel. Beams **12**, 114801 (2009).

Measurement of current evolution of intense electron beams during longitudinal compression

Tomonobu Itagaki[a,b)], Yasuo Sakai[a)], Jun Hasegawa [a,b)], Kazuhiko Horioka [a,b)]

a) Department of Energy Sciences, Tokyo Institute of Technology
b) School of Engineering, Tokyo Institute of Technology,
Midori-Ku, Yokohama 226-8502, Japan

ABSTRACT

We developed a significantly cost-effective scale-downed device to investigate the beam dynamics during longitudinal compression. The device demonstrated the effects of space charge on the compressed electron beams. We adopted specially designed Rogowski coils to monitor the process of beam compression at two different positions along the beam line.

Keywords

Intense charged particle beams, beam compression, induction accelerators, laser ablation plasma, Rogowski coil

1. Introduction

High power Heavy Ion Beam (HIB) is expected as a promising driver of Inertial Confinement Fusion (ICF) [1,2]. The ICF driver needs to supply a beam power of ~100 TW (roughly 1 MJ in 10 ns). To achieve such an extraordinarily high beam power, the ion beams are longitudinally compressed at the final acceleration process. However, in this process, space-charge effects are predicted to increase the beam emittance, which degrades the beam focusability [3]. While the detailed mechanism of beam degradation in the compression process still remains unclarified, experimental researches using a driver-level HIB like the system design at Lawrence Berkeley [4] are hard to perform from its cost.

Instead of such a huge and costly HIB device, we developed a device for scale-downed experiments which uses electrons instead of ions. High specific charge of electrons compared with heavy ions enables us to simulate the behavior of intense HIBs with a laboratory scale device.

2. Beam compression experiment

The schematic of the developed beam compression device is shown in Fig. 1. It consists of a laser ablation plasma electron source, an induction adder composed of five modules [5], a solenoidal transport line, and a Faraday cup placed at the longitudinal focal point of the electron beam.

The source plasma is produced by a Q-switched Nd:YAG laser with a wavelength of 1064 nm, a pulse width of 20 ns, and a maximum energy of 150 mJ. A titanium disk is irradiated by the laser with a spot diameter of ~1 mm. The plasma drifts to the extraction gap placed at the entrance of the solenoidal line.

Figure 2 shows ion (a) and electron (b) beam fluxes extracted through the gap with 3 kV and -3 kV bias voltages, respectively. The diameter of the extraction hole was 10 mm. As shown in Fig. 2(b), we obtained

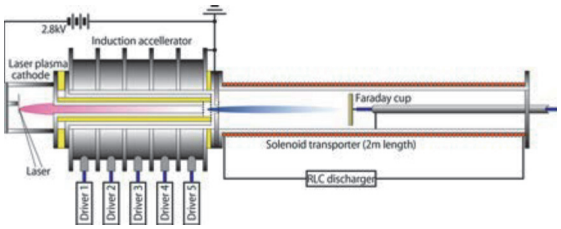

Fig. 1. Schematic of electron beam compression experiment.

an electron beam current of several tens of mA from the source plasma, which is much more intense than that from thermal electron guns used in our previous study [6]. In addition to the intensity, this beam source has several advantages for our experiment. First, owing to the drift motion of the plasma source, the extraction gap can be placed just before the beam modulation gap. Second, we can make parameter survey by changing the timing of modulation voltage application to the plasma, since the decay time of the plasma flux (~10 μs) is enough large compared with the modulation pulse length (~100 ns). As shown in Fig. 2, the electron beam current is tens of times larger than the ion beam current. We consider that the enhancement can be attributed to the drift motion of the source plasma which affects the sheath potential at the extraction boundary [7, 8].

The 5-unit induction adder regulated the modulation voltage for longitudinal bunching. The typical modulation pulse waveforms are shown in Fig. 3. The unit numbers in Fig. 3 correspond to each driver unit shown in Fig. 1, and a synthesisized pulse was applied to the modulation gap placed just after the beam extraction gap. The "ideal" line shows the modulation voltage waveform with which all electrons in the beam bunch are longitudinally focused to the same position in the beam line when the space-charge effect is ignored. As shown in the figure, the synthesisized pulse

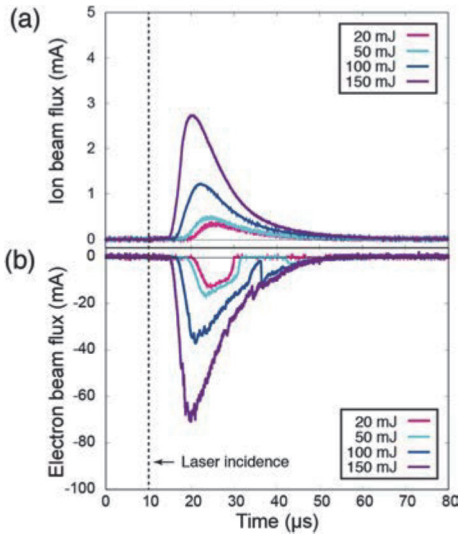

Fig. 2. Beam current waveforms extracted from laser-produced plasmas.

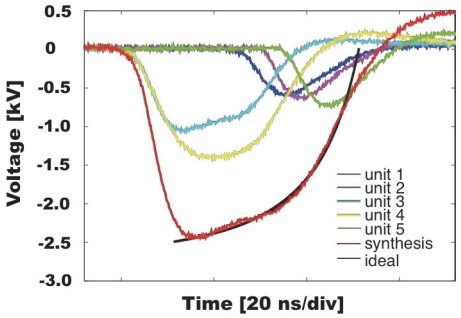

Fig. 3. Typical modulation pulse waveform applied to induction accelerator (focus length L_f=1.6 m)

("synthesis" in the figure) mostly matches the "ideal" line, that is, the beam modulation in our experiments are expected to be performed precisely. The modulation voltage was adjusted to a focus length L_f of 160 cm in the case of Fig. 3.

Thanks to precise modulation by the induction adder, the compressed beam has a sharp peak as shown in Fig. 4. When the initial beam current was 30 mA, the peak current of the compressed beam was ~170 mA.

Figure 5 summarizes the results of the bunch compression experiments. The result shows initial current dependence of the compression ratio, which is defined to be the ratio of the peak current to the initial current. When the initial current is larger than 10 mA, the compression ratio decreases with increasing initial current. This is the first experimental demonstration of the space charge effect on the longitudinally compressed charged particle beam.

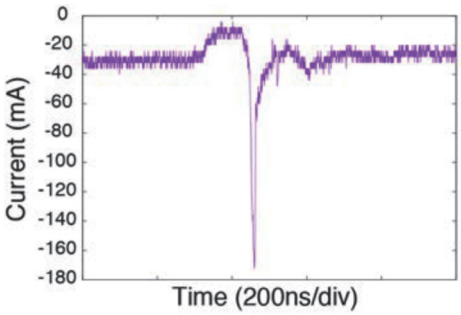

Fig. 4. Typical waveform of a compressed electron beam measured at focus point (focus length L=1.6 m).

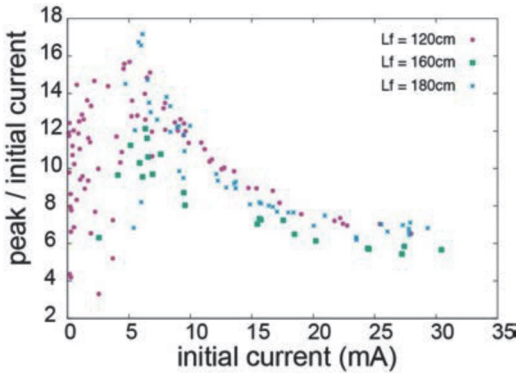

Fig. 5. Initial current dependence of beam compression ratio.

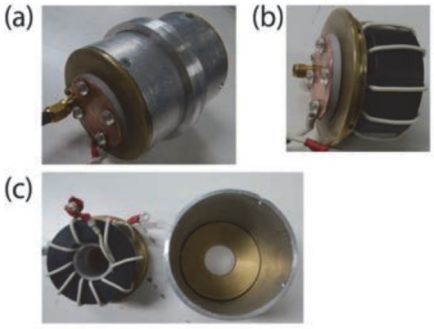

Fig. 6. A Rogowski coil and a metal case designed to be installed inside the solenoidal line.

3. Consideration for multipoint measurement with Rogowski coils

In the beam compression experiment described in Section 2, the initial current dependence of compression ratio is clearly observed in the regime where the initial current is more than 10 mA. However, in the lower current regime, the reproducibility of the beam current is not so good and the compression ratio varied shot to shot. To identify the cause of this variation, we tried to observe the time evolution of beam during compression with multipoint monitoring. Therefore, we installed non-destructive beam monitors in addition to the Faraday cup. Rogowski coils are often used as non-destructive beam monitor [9,10]. Since the commercially available ones are not suitable for our device from a geometrical restriction, we tried to manufacture suitable Rogowski coils.

3.1 Rogowski coil inside the transporting solenoid

The Rogowski coil that we made was designed to be installed in the solenoidal transport line. The Rogowki coil must have sufficient sensitivity with more than 1 V/A to measure 1-mA electron beams and a wide bandwidth enough to monitor the timescale ranging from 10 μs to 10 ns at compression peak. Also the magnetic core must accommodate the geometry of the transport line. Figure 6 shows photographs of the Rogowski coil. We used a FINEMET (Hitachi Materials) core because it has high permeability with good high frequency characteristics. The number of turns of the coil was determined to be 10, by which we obtained a sensitivity of 5 V/A and a cutoff frequency of 3 kHz. An aluminum case for the coil and a Faraday cup attached to the case are also shown in the figure. We examined the characteristics of the coil by monitoring a beam simultaneously with the Faraday cup.

The typical result is shown in Fig. 7. The beam current measured is smaller than that in Section 2 because the diameter of beam extraction port is reduced to 2 mm to prevent the beam from hitting the coil. Without modulation and compression (Fig. 7(a)), the waveform from the Rogowski coil well coincide with that from the Faraday cup. With modulation (Fig. 7(b)), the coil could not observe the beam correctly. This is probably because the beam orbit was disturbed by the discontinuity of the guiding magnetic field caused by incerting the ferromagnetic core [11].

From the output waveforms of the Rogowski coil and the Faraday cup, we estimated relative sensitivity of the coil. Figure 8 shows the relative sensitivity of the coil. As shown in the figure, the relative sensitivity increased in the high frequency range. This might be caused by the parasitic capacitance between the coil winding, i.e., the frequency characteristics of the Rogowski coil was not flat.

We examined the effect of the magnetic core on the magnetic field of the beam transport line. Figure 9 shows the magnetic field measured by a Gauss meter along the center axis of the beam line.

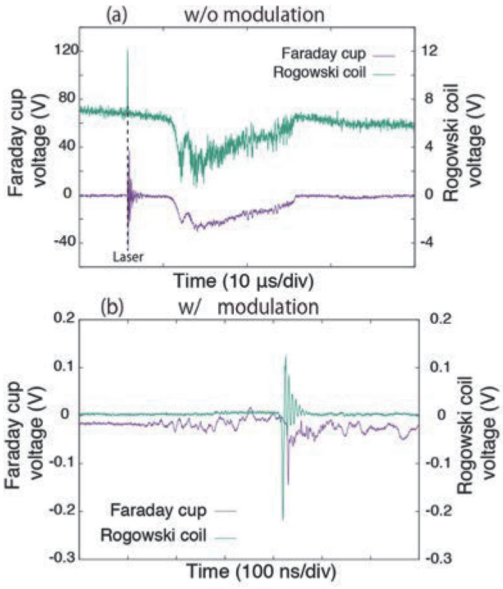

Fig. 7 Beam waveforms of Rogowski coil inside the solenoid and comparative Faraday cup signals.

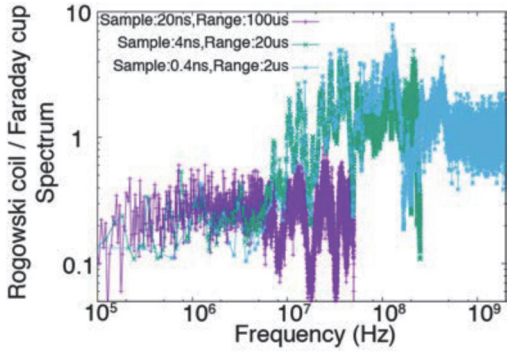

Fig. 8. Frequency characteristic of relative sensitivity of the prototypical Rogowski coil.

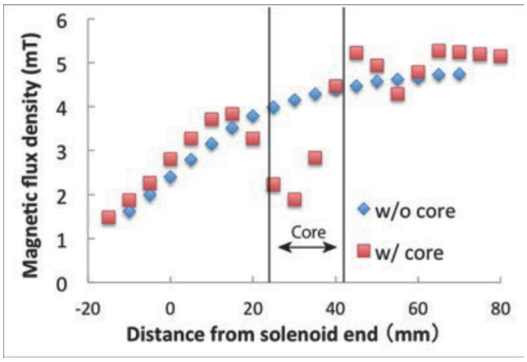

Fig. 9. Effect of the Rogowski core on the magnetic field of solenoidal beam transport line.

The result supports that the beam transport is disturbed by the modulation of the solenoidal field. After all, we concluded that this coil is unsuitable for the non-destructive beam measurement.

3.2 Beam monitoring from outside

Since the prototypical Rogowski coil that we made is not suitable to be installed inside the solenoidal line, we tried another way to monitor the beams with Rogowski coils which were installed outside the solenoidal line. The new coils monitor the electron beam through the insulator flanges as shown in Fig. 10.

The result of beam monitoring with this configuration is shown in Fig. 11. When it is without beam modulation (Fig. 11(a)), the measured waveform by the Rogowski coils were similar to those by the Faraday cup. The coil signals decay faster than the Faraday cup signal, which is due to the insufficient permeability of the magnetic cores. On the other hand, as shown in Fig. 11(b), a large noise, which was completely different from the beam signal, was observed by the coils when the beam was modulated. This noise may be due to the beam modulation pulse. Probably, the noize came through the wall of the beam transport line because it was not observed with the prototype coils installed inside the solenoid. This is supported also by the fact that the timing of the noise and modulation pulse coincide with each other.

From the above resutls, we conclude that for non-destructive beam measurement, we have to increase the S/N ratio of Rogowski coils.

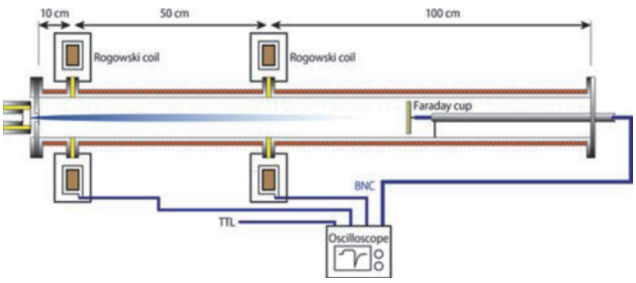

Fig. 10. The configuration of Rogowski coils outside the beam line and a Faraday cup.

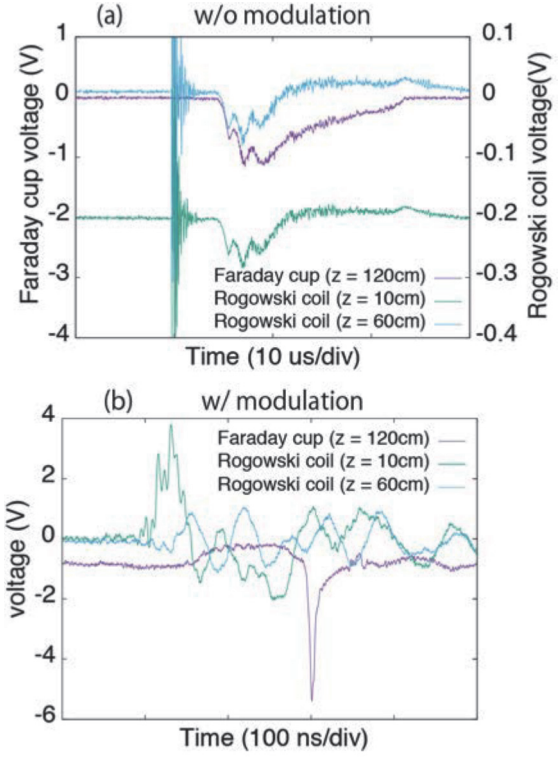

Fig. 11 Measured beam waveforms of Rogowski coils outside the solenoid and Faraday cup.

4. Conclusion

To contribute the HIB driven ICF, we developed a revolutionary compact and cost-effective scale-downed electron beam device for longitudinal compression of intense charged particle beams. Using this device, we showed the first successful experimental results for longitudinal beam compression in space charge dominated regime. The results showed that the beam compression ratio decreases with increasing beam intensity. The results demonstrated that the scale down devices is useful for the beam dynamics study in the space charge dominated regime.

We tried to monitor the detailed time evolution of the beams during the compression with Rogowski coils. In order to accommodate the geometry of the beam transport line, we manufactured several types of Rogowski coils. However, those Rogowki coil could not measure electron beam current waveforms with a 10-ns timescale at the focusing region.

References

[1] Fusion policy advisory committee, final report, DOS/S-0081, September 1990.

[2] K. Horioka, Journal of Plasma and Fusion Research, **89**, 87-88, (2013).

[3] T. Kikuchi, K. Horioka, Nuclear Instruments and Methods in Physics Research **A 606** pp.31-36 (2009).

[4] R.Bangerter, A. Faltens, and P. Seidl. Reviews of Accelerator Science and Technology, **6**, 85-116, (2013).

[5] K. Takayama, Journal of Plasma and Fusion Research, **Vol.89**, pp.102-109, (2013)

[6] Yasuo Sakai, Mitsuo Nakajima, and Kazuhiko Horioka. Review of scientific instruments, **Vol.87**, 083306 (2016).

[7] Y. Sakai, T. Itagaki, K. Horioka, Physics of Plasmas, American Institute of Physics, **Vol.23**, pp. 123112-1-7, (2016).

[8] Y. Sakai, T. Itagaki, K. Horioka. Plasma and Fusion Research, The Japan Society of Plasma Science and Nuclear Fusion Research, **Vol. 11**, pp. 1206107-1-2, (2016).

[9] M. Tobiyama, OHO texts, KEK, (2008).

[10] M. Wada, Y. Ishida, T. Nakamura, A. Takamine, A. Yoshida, and Y. Yamazaki. RIKEN Accel. Prog. Rep. 38 (2005).

[11] D. G. Pellinen, M. S. D. Capua, S. E. Sampayan, H. Gerbracht, and M. Wang, Physics International Company. San Leandro. California 94577, (1980).